Modulation Scheme Investigation for High-Power Medium-Voltage Current Source Converter Based Drives

by

Martti Muzyka

Submitted in partial fulfillment of the requirements
for the degree of Master of Science in
Electrical and Computer Engineering

Lakehead University

Thunder Bay, Ontario

April 2023

Abstract

Pulse width modulated (PWM) current source converter (CSC) based drives are commonly used in high-power (1-10 MW), medium-voltage (MV) (2.3-6.6 kV) applications. These drives feature a simple converter structure, inherent four-quadrant operation capabilities, motor-friendly waveforms, and reliable fuseless short-circuit protection. PWM CSC-based drives are generally constructed using symmetrical gate-commutated thyristors (SGCTs) with reverse voltage blocking capabilities. In order to avoid exceeding the thermal limits of these SGCT devices, and to minimize switching losses, the device switching frequency used by PWM CSC-based drives is typically kept below 500 Hz. There are three main modulation schemes used in MW-level MV PWM CSC-based drives: space vector modulation (SVM), trapezoidal pulse width modulation (TPWM), and selective harmonic elimination (SHE). Of these three modulation schemes, SHE possesses the best harmonic performance as it features the ability to eliminate a number of low-order harmonics, all while retaining a low switching frequency. However, due to its off-line implementation, SHE suffers from poor dynamic performance, and in certain cases, requires a large, memory-exhaustive look-up table. To address these issues, this research investigates ways of improving the dynamic performance of conventional SHE through on-line (i.e., real-time) implementation. Two new modulation schemes are proposed: on-line SHE for modulation of the grid-side PWM current source rectifier (CSR) and SHE-TPWM for modulation of the motor-side PWM current source inverter (CSI). The proposed on-line SHE scheme models the independent switching angles used in conventional SHE as polynomial functions by applying curve-fitting techniques. This method of implementation improves the dynamic performance of conventional SHE, as it enables real-time computation of switching angles, and eliminates the need for look-up tables. Conversely, the proposed SHE-TPWM scheme combines the principles, while retaining the respective advantages, of both conventional SHE and TPWM. This integrative approach enables SHE-TPWM to possess SHE-level harmonic performance, along with improved dynamic performance rivaling that of TPWM.

Acknowledgments

I would like to first and foremost thank my thesis supervisor, Dr. Qiang Wei, for his guidance and support throughout my graduate studies. Dr. Wei has been an invaluable mentor to me, providing me with insightful feedback, challenging me to think critically, and encouraging me to pursue my research interests. His in-depth knowledge and expertise in the field of power electronics has been instrumental in shaping the scope and direction of my research. I have learned so much from him and feel privileged to have had him as my supervisor.

I would like to extend another thank you to my colleague, Mr. Zijian Wang, for his tireless efforts in assisting me with the preparation and execution of laboratory experiments. It is without a doubt that, without his help, these experiments could not have been completed as quickly and seamlessly as they were.

Additionally, I would like to take this opportunity to extend my gratitude to all those who attended my seminar presentation. I am incredibly grateful for the thoughtful questions, feedback, and advice that I received from the audience. I want to give special thanks to Drs. Ameli, Dekka, and Zhou for raising some excellent points that have helped me improve the overall quality of my research. Their insights and suggestions have been invaluable, and I am deeply appreciative of their time and effort.

Lastly, I would like to express my gratitude to my group members for their support and collaboration throughout my graduate studies. Their insights, suggestions, and assistance have been invaluable in helping me overcome the various challenges and obstacles that I encountered along the way, and I feel incredibly fortunate to have been a part of such a talented group of researchers.

Table of Contents

List of Figures

List of Tables

List of Symbols

Symbol	Description
f_{sw}	Device Switching Frequency
C_f	Three-Phase Filter Capacitance
L_s	Line Inductance
ω_{res}	LC Resonant Frequency
L_d	DC Choke Inductance
I_d	DC-Link Current
S_{1-6}	CSI/R Switches
i_w	PWM Current
i_{wA-wC}	PWM Current per Phase
v_m	Modulating Signal
v_{cr}	Carrier Signal
m_a	Amplitude Modulation Index
$\hat{V}_{cr}$	Peak Value of the Carrier Signal
$\hat{V}_m$	Peak Value of the Modulating Signal
I_{wn}	Magnitude of the nth PWM Current Harmonic
$I_{w1,max}$	Maximum Magnitude of the Fundamental PWM Current Harmonic
f_1	Fundamental Frequency
N_p	Number of Pulses per Half-Cycle of the PWM Current
$\vec{I}_0$	Zero Space Vector
$\vec{I}_{1-6}$	Active Space Vectors

$\vec{I}_{ref}$	Reference Current Vector
θ	Phase Angle of the Reference Current Vector
ω	Angular Velocity of the Reference Current Vector
f_s	Sampling Frequency
T_s	Sampling Period
T_{0-2}	Space Vector Dwell Times
θ_{1-k}	SHE Switching Angles
F_{1-k}	Transcendental SHE Equations
t_{ov}	Overlap Time
$\lvert\Delta\theta\rvert$	Absolute Switching Angle Error
$\theta_{\text{approximate}}$	Approximated Switching Angles
θ_{actual}	Actual Switching Angles
R_s	Load Resistance
v_{g1-g6}	Gating Signals
α_i	Lagrange Polynomial Coefficients
i_s	Filtered Output Current
i_{sA-sC}	Filtered Output Current per Phase
i_c	Capacitor Current

List of Abbreviations

Abbreviation	Description
PWM	Pulse Width Modulation
CSC	Current Source Converter
MV	Medium-Voltage
CSR	Current Source Rectifier
CSI	Current Source Inverter
SGCT	Symmetrical Gate-Commutated Thyristor
CMV	Common-Mode Voltage
TPWM	Trapezoidal Pulse Width Modulation
SVM	Space Vector Modulation
SHE	Selective Harmonic Elimination
THD	Total Harmonic Distortion
VSC	Voltage Source Converter
SHC	Selective Harmonic Compensation
VI-SHC	Virtual Impedance-Based Selective Harmonic Compensation
MPSPC	Model Predictive Switching Pattern Control
MPC	Model Predictive Control
IGBT	Insulated Gate Bipolar Transistor
FFT	Fast Fourier Transform

1 Chapter 1 - Introduction

1.1 PWM CSC-Based Drives

Pulse width modulated (PWM) current source converter (CSC) based drives are commonly used in high-power (1-10 MW), medium-voltage (MV) (2.3-6.6 kV) applications [1–6]. These drives offer a number of advantages including a simple converter structure, inherent four-quadrant operating capabilities, motor-friendly waveforms, high input power factor, and reliable fuseless short-circuit protection [5, 6]. In regards to their drawbacks, PWM CSC-based drives are limited in terms of dynamic performance and are susceptible to potential LC resonance [5, 6]. Fortunately, high dynamic performance is not the main priority for the majority of applications in which MV drives are utilized, and LC resonance can be suppressed through selective harmonic elimination (SHE) and/or active damping control [5, 7, 8].

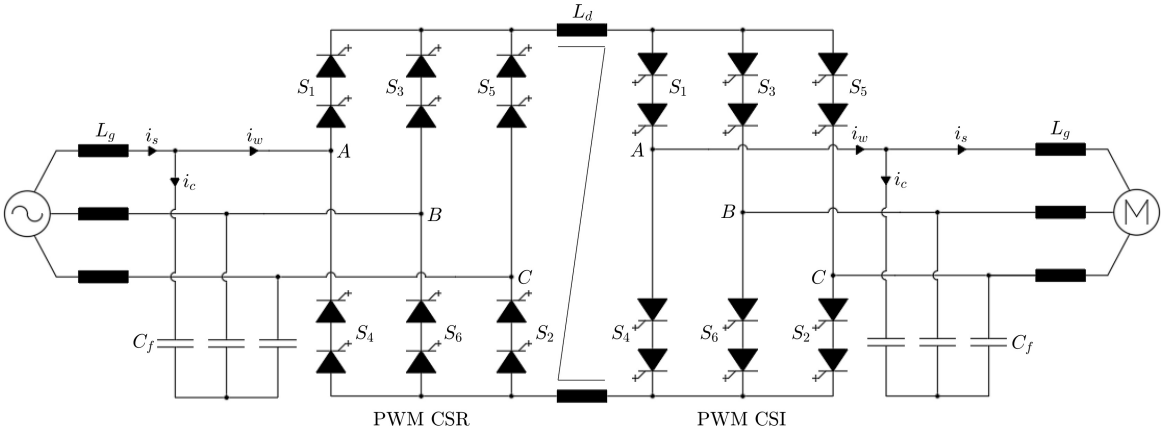

Figure 1: Connection diagram of a three-phase PWM CSC-based drive.

As shown in Fig. 1, a typical three-phase PWM CSC-based drive consists of a front-end single-bridge PWM current source rectifier (CSR), feeding a motor-side PWM current source inverter (CSI). In order to ensure uni-directional current flow and to enable operation at high utility voltages, these drives are commonly configured using sets of series-connected symmetrical gate-commutated thyristor (SGCT) switches, with reverse voltage blocking capabilities [5, 9–12]. The number of series-connected switches in each branch of the drive will vary depending on the rated utility voltage and the ratings of each

switch. For instance, a total of four 6000V SGCTs are necessary in each branch, if the line-to-line utility voltage is rated at 4160V [5]. Due to the inherent high thermal resistance of the SGCTs used in PWM CSC-based drives, they lack the ability to efficiently transfer heat away to their respective heat-sinks, and thus can overheat when switched at high frequencies [5,13]. As a result, PWM CSC-based drives typically feature device switching frequencies (f_{sw}) limited below 500 Hz, which is also done in order to minimize switching losses [5, 12, 13].

PWM CSC-based drives require both grid-side and motor-side three-phase filter capacitors (C_f) to assist in the commutation of the switching devices, and to filter out unwanted line/motor current harmonics [5, 14, 15]. The size of these three-phase filter capacitors is dependent on a number of different factors including the chosen switching frequency and modulation scheme, grid-code requirements, input power factor, and LC resonance [5]. The issue of LC resonance results from the LC resonant network formed by the grid-side total line inductance (L_s or L_g) and the grid-side filter capacitors [5,7,14,15]. Given that the grid-side three-phase filter capacitors and total line inductance are typically in the range of 0.3-0.6 per-unit (pu) and 0.1-0.15 pu respectively, this corresponds to an LC resonant frequency (ω_{res}) between 3.3 and 5.8 pu [5]. Often because the device switching frequency featured in PWM CSC-based drives is kept so low, the 5th and 7th PWM current harmonics generated by the front-end PWM CSR are capable of exciting this LC resonant mode [5, 7, 13]. For this reason, it is imperative that the LC resonant frequency be kept below the lowest possible harmonic produced by the PWM CSR, and if this is not a possibility, that active damping control be implemented [5, 7, 14, 15].

Another important component of PWM CSC-based drives is the DC choke (L_d), which is required in order to smooth the DC-link current (I_d) supplied to the motor-side PWM CSI [5, 12]. In practice, the DC choke is customarily implemented as a magnetic core with two coils, each connected to the positive and negative terminals of the DC bus [5,16,17]. This configuration reduces the motor common-mode voltage (CMV) [5,16]. The size of the DC choke inductor typically ranges from 0.5-0.8 pu, in order to limit the DC-link current ripple below 15% [5].

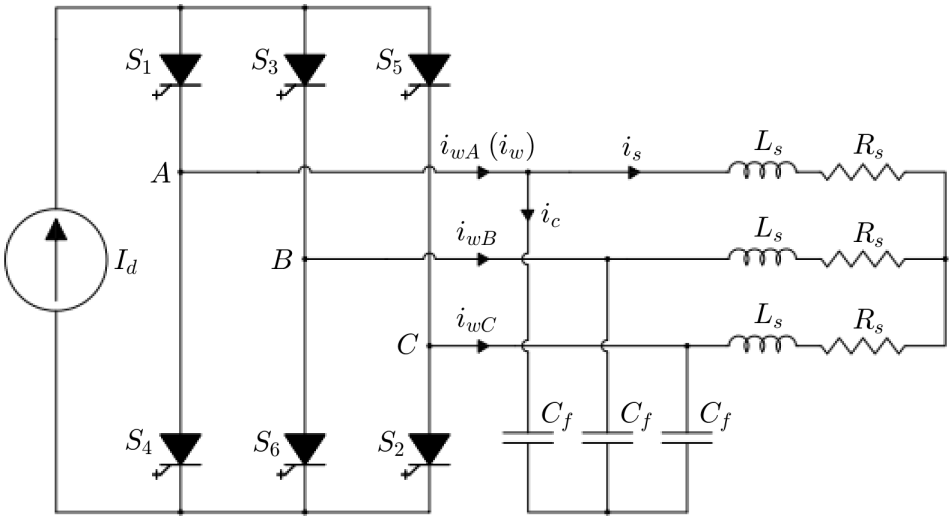

Figure 2: Connection diagram of a three-phase PWM CSI.

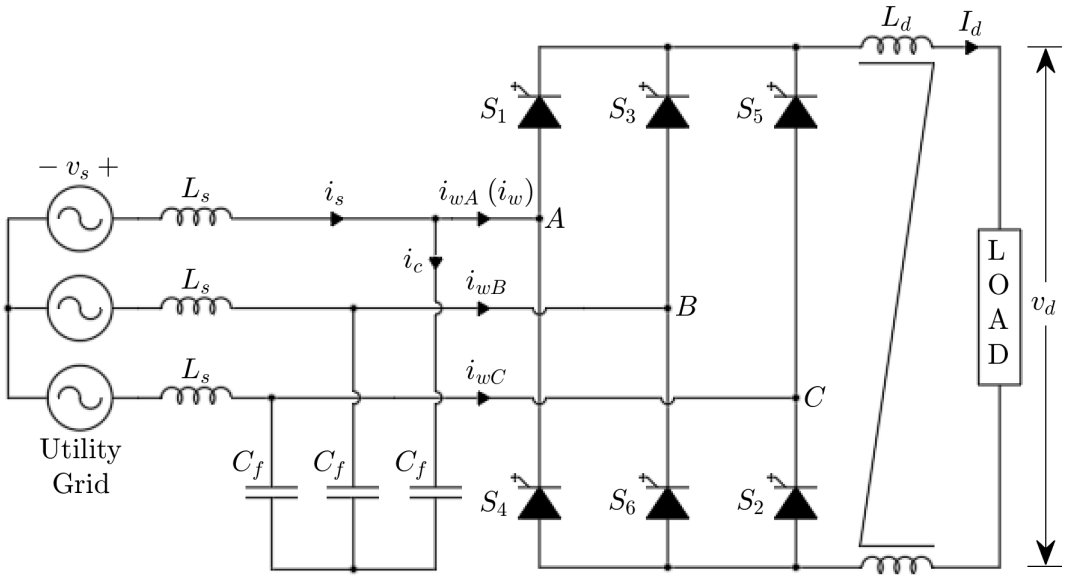

Figure 3: Connection diagram of a three-phase PWM CSR.

1.2 CSC Modulation Schemes

There are three main modulation schemes used in MW-level, MV CSC-based drives: trapezoidal pulse width modulation (TPWM), space vector modulation (SVM), and selective harmonic elimination (SHE) [5, 6, 13]. In order to be used effectively in PWM CSC-based drives, each of these three modulation schemes must ensure that the following two conditions are satisfied: (1) that the DC-link current is kept continuous, and (2) that the PWM current (i_w) remains defined [5, 6, 18]. In essence, these conditions mean that only one upper and one lower switch can conduct at once, aside from during commuta-

tion intervals, in both the grid-side PWM CSR and motor-side PWM CSI [5,6,18]. If less than two switches conduct simultaneously, then the DC-link current will suddenly drop, resulting in a high induced voltage across the DC choke, which can damage the switching devices [5].

Three-phase PWM CSIs and CSRs feature a total of nine switching states compliant with the constraints outlined previously [5, 6, 8, 18]. These switching states are listed in Table 1, where they are also classified as either zero or active switching states. Zero states refer to cases where the top and bottom switches in the same converter leg both conduct, such as S_1 and S_4 in leg A for the [14] switching state. Operation under these zero state conditions is referred to as bypass operation, as under these conditions, the DC current is bypassed from the load, resulting in: $i_{wA} = i_{wB} = i_{wC} = 0$ [5]. The active states included in Table 1 refer to cases where the top and bottom switches in different legs of the converter both conduct, such as S_1 in leg A and S_2 in leg C for the [12] switching state. This active and zero state classification is an important aspect of space vector modulation, which is introduced in Section 1.2.2.

Table 1: CSI/R switching states and space vectors.

Type	Switching State	On-State Switches	PWM Current			Space Vector
			i_{wA}	i_{wB}	i_{wC}	
Zero States	[14]	S_1, S_4	0	0	0	I_0
	[36]	S_3, S_6				
	[52]	S_5, S_2				
Active States	[61]	S_6, S_1	I_d	$-I_d$	0	I_1
	[12]	S_1, S_2	I_d	0	$-I_d$	I_2
	[23]	S_2, S_3	0	I_d	$-I_d$	I_3
	[34]	S_3, S_4	$-I_d$	I_d	0	I_4
	[45]	S_4, S_5	$-I_d$	0	I_d	I_5
	[56]	S_5, S_6	0	$-I_d$	I_d	I_6

1.2.1 TPWM

TPWM is a carrier-based modulation scheme that generates a PWM waveform through comparison of a trapezoidal modulating signal (v_m) to a triangular carrier signal (v_{cr}), as illustrated by Fig. 4 [5,6,13]. For TPWM, the amplitude modulation index (m_a) is defined as

$$m_a = \frac{\hat{V}_m}{\hat{V}_{cr}} \tag{1}$$

where $\hat{V}_m$ and $\hat{V}_{cr}$ refer to the peak values reached by the trapezoidal modulating signal and the triangular carrier signal, respectively [5]. In order for TPWM to satisfy the CSC switching constraints outlined in Section 1.2, the PWM current is not modulated within the center $\pi/3$ intervals of each half cycle (i.e., no bypass operation) [5, 6, 13]. As a result, the magnitude of the PWM currents fundamental harmonic (I_{w1}) can only be adjusted within a limited range of its maximum value (i.e., $I_{w1,max}$) [5]. For instance, the fundamental harmonic of the PWM current produced by the TPWM switching scheme illustrated in Fig. 4, can only be adjusted within the following range:

$$0.863 I_{w1,max} \leq I_{w1} \leq I_{w1,max}. \tag{2}$$

Due to this limitation, TPWM-based amplitude modulation index control is not typically used to control the magnitude of the PWM currents fundamental harmonic [5]. In practice, this is instead accomplished by varying the DC-link current through control of the front-end PWM CSR [5].

Fig. 5 (a) shows the harmonic spectrum of the PWM current achieved using the TPWM switching scheme illustrated in Fig. 4, with a fixed amplitude modulation index of 0.85. Based on this figure, it is clear that the generated PWM current does not possess any even-order harmonics, which results from the fact that it exhibits half-wave symmetry [5]. Furthermore, there are also two observable pairs of dominant harmonics located at $n = 17/19$ and $n = 13/23$. These dominant harmonic pairs are intrinsic to all TPWM switching schemes, and are positioned based on

$$n = 3(N_p - 1) \pm 1 \tag{3}$$

and

$$n = 3(N_p - 1) \pm 5 \tag{4}$$

where N_p refers to the number of pulses per half-cycle of the PWM current [5]. Fig. 5 (b) and (c) show the PWM currents harmonic content across the full range of the amplitude modulation index. These illustrations further highlight the fact that the magnitude of the PWM currents fundamental harmonic can only be adjusted within a limited range of its maximum value, when relying solely on TPWM. Furthermore, it is also apparent that this TPWM scheme achieves its best harmonic performance while operating at an amplitude modulation index of 0.85. This occurrence happens to hold true for all other TPWM switching schemes [5]. Therefore, in order to minimize the PWM currents total harmonic distortion (THD) when using TPWM, it is wise to operate at an amplitude modulation index of 0.85.

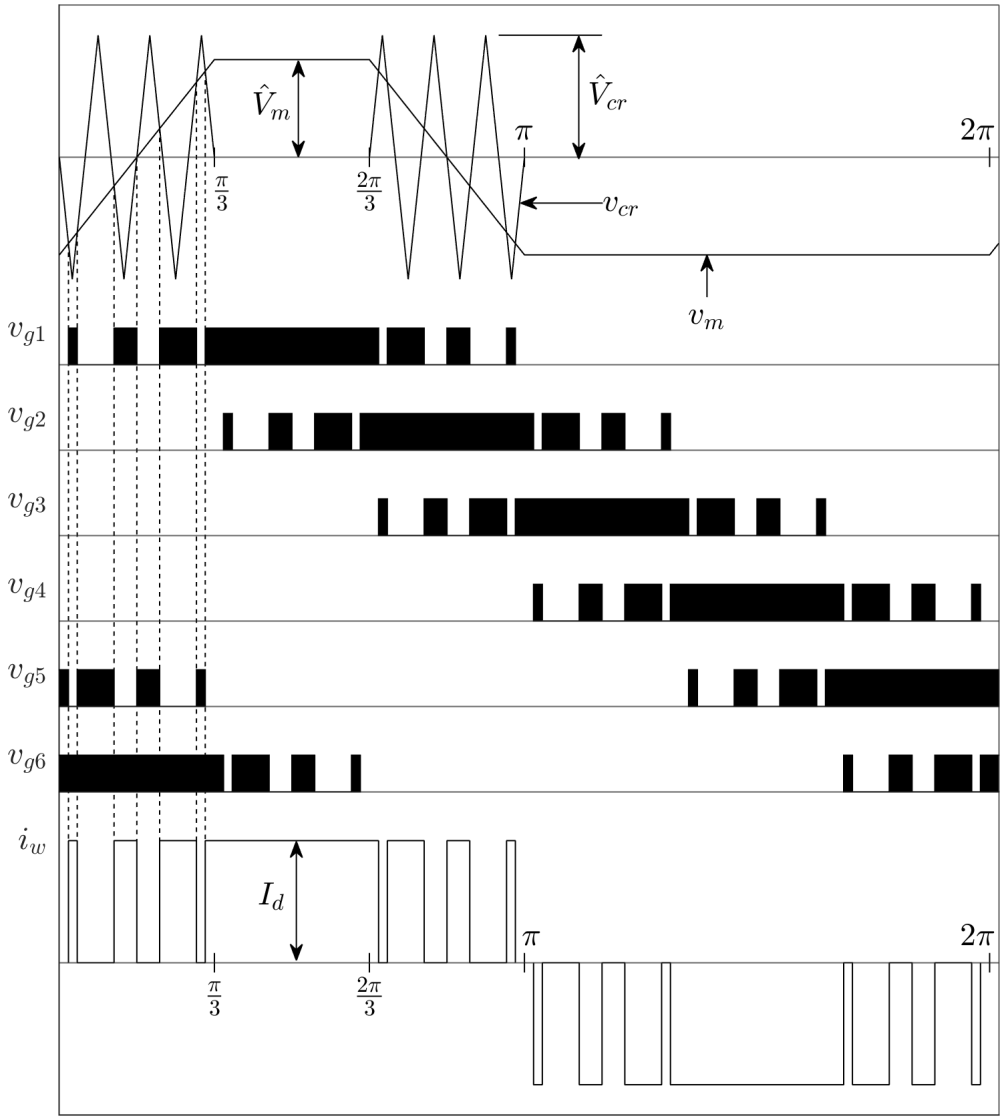

Figure 4: Principle of TPWM ($N_p = 7$, $m_a = 0.8$).

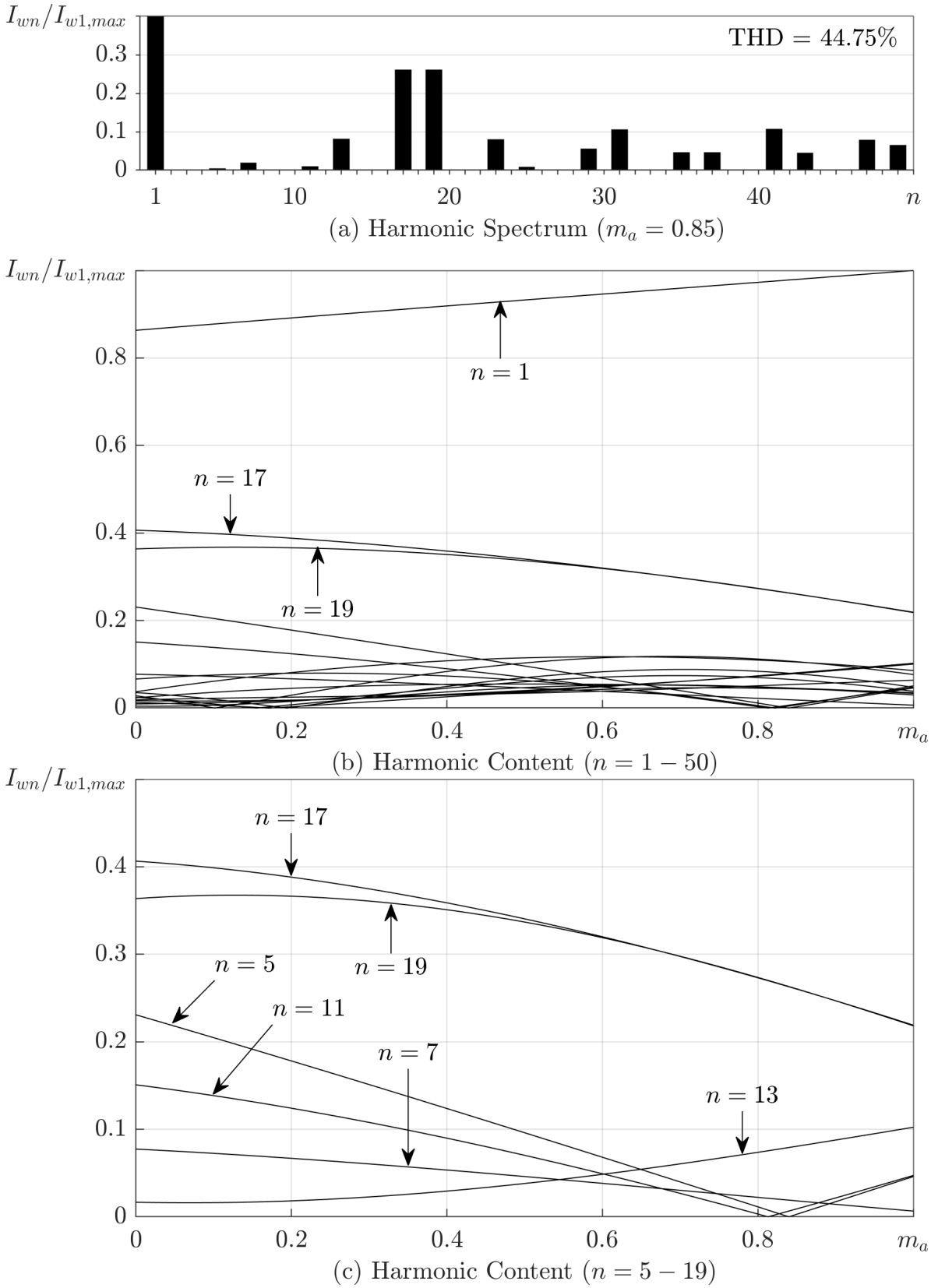

Figure 5: PWM current (i_w) harmonic content produced by TPWM operating at a fixed amplitude modulation index (m_a) of 0.85 (a), and across the full range of the amplitude modulation index (b)-(c) ($N_p = 7$).

The device switching frequency associated with a particular TPWM switching scheme can be determined using

$$f_{sw} = f_1 \times N_p \tag{5}$$

where f_1 refers to the fundamental frequency of the generated PWM current [5]. By assuming a fundamental frequency of 60 Hz and applying (5) to the model $N_p = 7$ TPWM scheme shown in Fig. 4, this yields a device switching frequency of 420 Hz. It should be noted that (5) can also be applied to determine the device switching frequency inherent to SHE and SVM schemes as well [5].

1.2.2 SVM

SVM is an on-line modulation scheme that offers the best dynamic performance of all three modulation schemes used in MW-level, MV PWM CSC-based drives [5, 6, 13]. However, SVM also features the worst harmonic performance, which prevents it from seeing much success in commercial applications, unlike SHE and TPWM [5,6,13]. As will be shown later on this section, implementation of SVM typically results in a PWM current harmonic profile that possesses high magnitude, low-order harmonics, such as the 5th and 7th, that lie close to the resonant frequency of the grid-side LC filter [5, 13]. These high magnitude, low-order current harmonics pose a problem, as they can introduce resonance if the system is inadequately damped [5,13]. Fortunately, new SVM modulation techniques like multi-sampling SVM and natural sampling SVM have been proposed, which address these issues, and offer improved low-order harmonic performance [13, 19, 20].

When applying SVM to a three-phase PWM CSI, the active and zero switching states listed in Table 1 are represented as active and zero space vectors [5, 6, 13]. As shown in Fig. 6, the six active space vectors form a two-dimensional hexagon with six equal sectors, with the zero vector located at its center [5,6,13]. The magnitude and phase of the output PWM current is then represented by a reference vector ($\vec{I}_{ref}$) rotating in two-dimensional space within this hexagon [5,6,13]. The angular velocity (ω) at which this reference vector rotates in space, is proportional to the fundamental frequency of the PWM current, as shown by

$$\omega = 2\pi f_1. \tag{6}$$

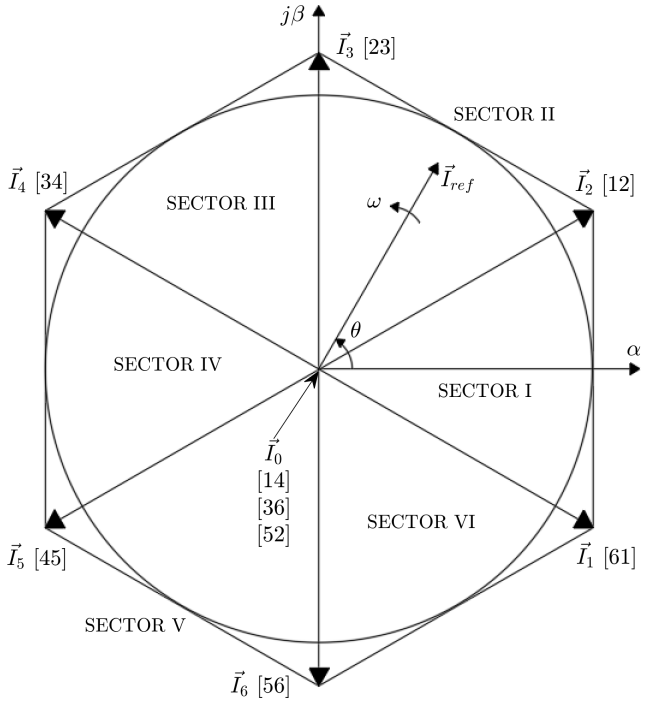

Figure 6: PWM CSI space vector diagram.

Given that SVM is well optimized for discrete operation, it features a finite sampling frequency (f_s), which refers to the rate at which the reference current vector is sampled [5]. Predictably, the sampling period (T_s) is related to the sampling frequency by

$$T_s = \frac{1}{f_s}. \tag{7}$$

Assuming that the sampling period is sufficiently small, the reference current vector can be regarded as constant throughout each sampling interval [5]. Based on this assumption, the reference current vector can be synthesized using two nearby active vectors and one zero vector [5, 6, 13]. This allows for translation of the characteristics of the reference current vector, such as its magnitude and phase, to tangible switching states, as each of the stationary active and zero vectors correspond to unique switching states of the PWM CSI, as shown previously in Table 1. In order to determine the length of time for which each switching state is active during a particular sampling period, the dwell times of the stationary space vectors used in the synthesis of the reference current vector must be

determined [5, 13]. Considering the case illustrated in Fig. 7, where the reference current vector is located in Sector I. The reference current vector can be synthesized using the nearest stationary space vectors: $\vec{I}_1$, $\vec{I}_2$, and $\vec{I}_0$. Expressions representing the dwell times of each of the three closest space vectors can be derived by applying the ampere-second balancing principle [5]. The resultant expressions are shown below.

$$\begin{cases} T_1 = m_a \sin(\pi/6 - \theta) T_s \\ T_2 = m_a \sin(\pi/6 + \theta) T_s \text{ for } -\pi/6 \leq \theta < \pi/6 \\ T_0 = T_s - T_1 - T_2 \end{cases} \tag{8}$$

In (8), θ refers to the phase angle of the reference current vector, while the amplitude modulation index for SVM is defined by

$$m_a = \frac{I_{ref}}{I_d} = \frac{\hat{I}_{w1}}{I_d}, \tag{9}$$

where I_{ref} refers to the magnitude of the reference current vector [5].

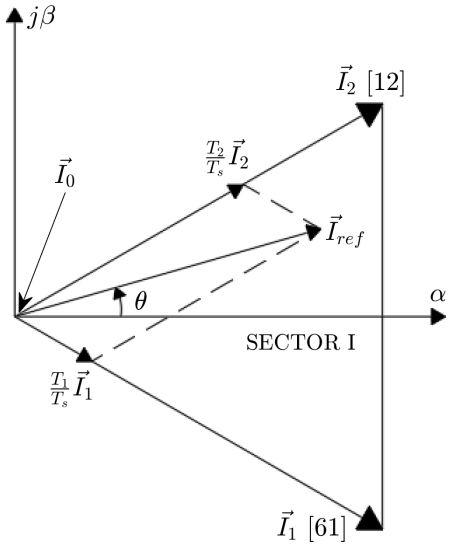

Figure 7: Synthesis of the reference current vector ($\vec{I}_{ref}$) in Sector I, using the following stationary space vectors: $\vec{I}_0$, $\vec{I}_1$, and $\vec{I}_2$.

Another important aspect of SVM, is the selection of an appropriate switching sequence. In order for a space vector switching sequence to be used in a PWM CSI, it must not only comply with the switching constraints outlined in Section 1.2, but must also ensure that the resultant device switching frequency is minimized and that the PWM

currents in each phase are balanced [5, 13, 18, 21]. To ensure that the device switching frequency inherent to a particular switching sequence is minimized, the following conditions must be met: (1) the transitions between switching states must only involve two switches, and (2) the number of switches involved in the transitions between sectors must be minimal [5, 13, 21]. The three-segment switching sequence (i.e., SQ1) shown in Fig. 8, satisfies these conditions.

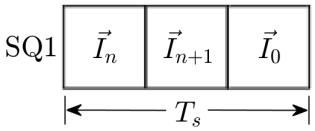

Figure 8: Three-segment SVM switching sequence (SQ1).

Fig. 9 provides an illustration of a SVM switching scheme in which the SQ1 sequence is used. Given a fundamental frequency of 60 Hz, this SVM scheme features a device switching frequency of 360 Hz, and a sampling frequency of 720 Hz. The PWM current produced by the SVM scheme detailed in Fig. 9 possesses a number of high magnitude, low-order harmonics, as shown in Fig. 10. Most notable are the 5th and 7th order PWM current harmonics, as these can lie close to the resonant frequency of the input/output LC filter, and can be amplified [5, 6, 13]. This is often the case with SVM, hence why it is typically not viable for practical usage [5, 6, 13].

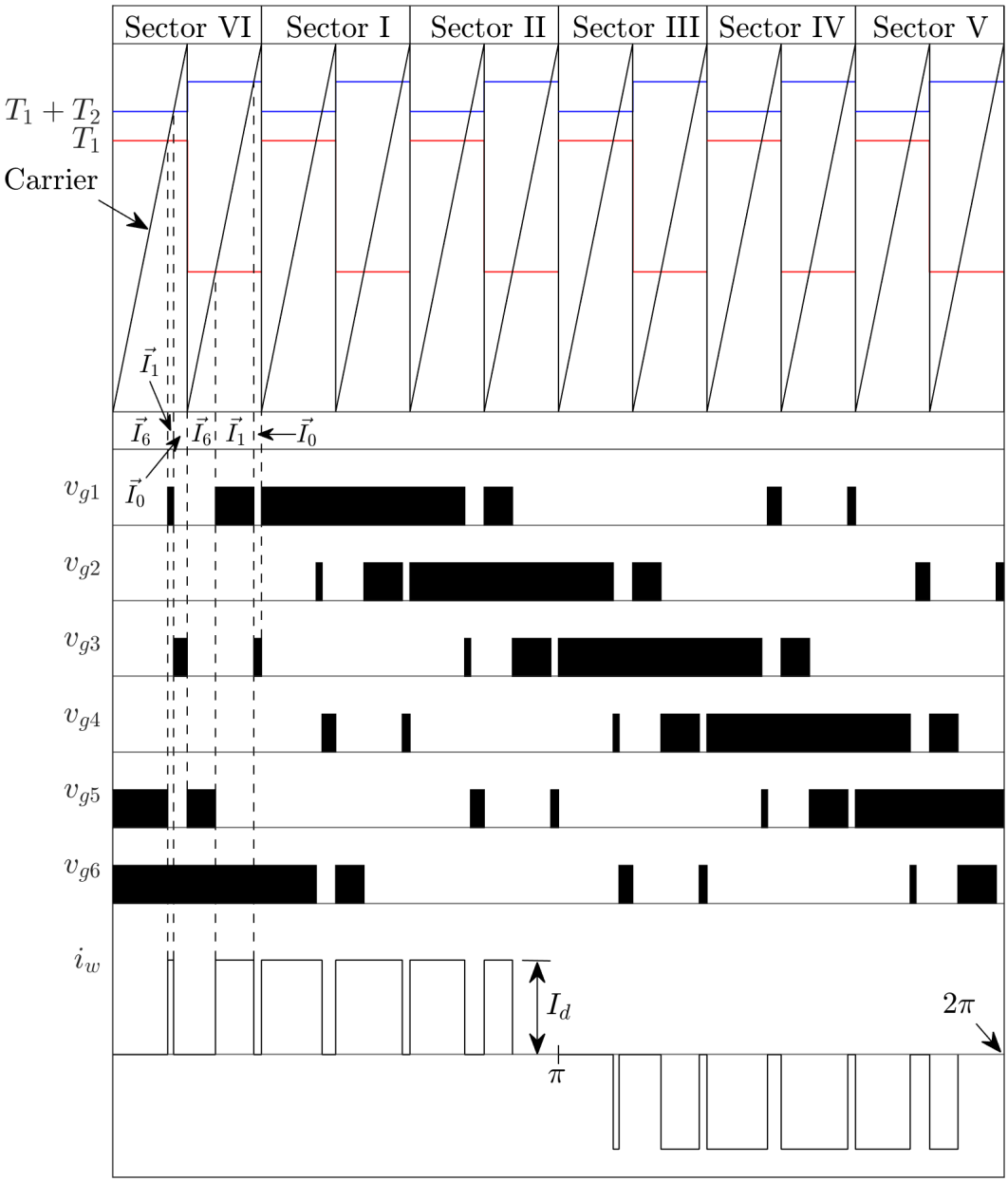

Figure 9: SVM switching scheme that uses SQ1 ($N_p = 6$, $f_s = 720$ Hz, $m_a = 0.9$).

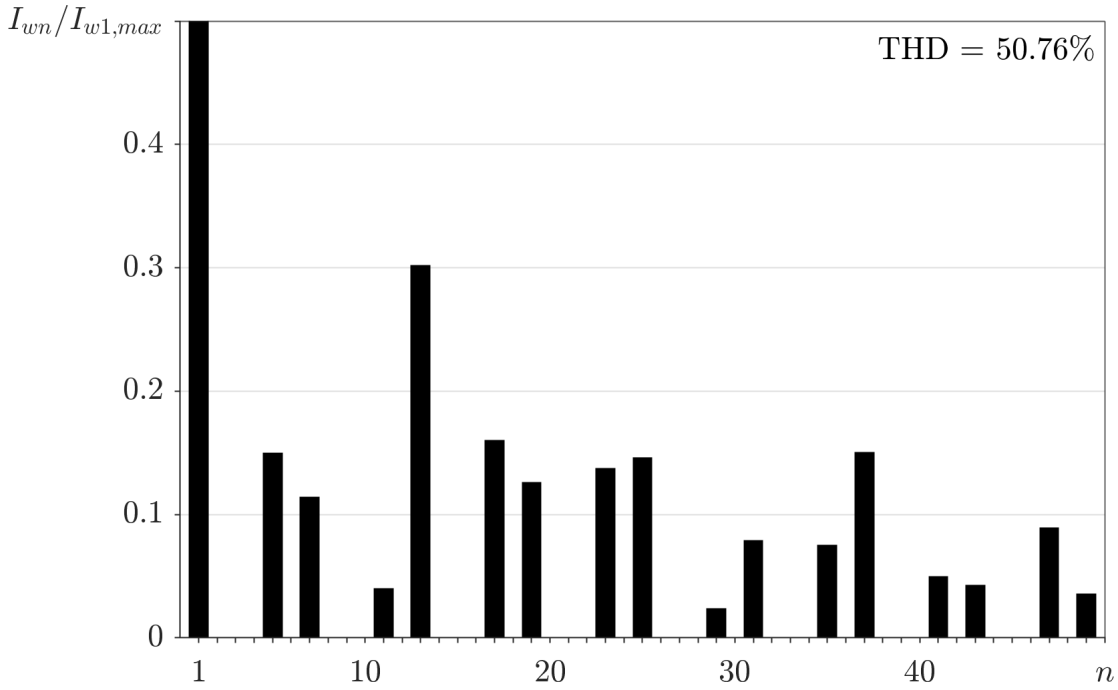

Figure 10: The PWM current (i_w) harmonic spectrum produced by the $N_p = 6$ SVM scheme that uses SQ1 ($N_p = 6$, $f_s = 720$ Hz, $m_a = 0.9$).

1.2.3 SHE

SHE is an off-line modulation scheme capable of eliminating a number of unwanted low-order harmonics present in the PWM current of PWM CSC-based drives, all while retaining a low device switching frequency [5, 6, 13]. In comparison to TPWM and SVM, SHE offers the best harmonic performance, and as a result, it is widely used throughout industry [5, 6, 13]. Depending on the intended application, SHE can either be configured with or without amplitude modulation index control [5, 6]. In general, amplitude modulation index control is not needed for modulating the motor-side PWM CSI, as it is preferable to maintain the amplitude modulation index at its maximum value (e.g., $m_a = 1$) [5]. However, when it comes to modulating the front-end PWM CSR, amplitude modulation index control is typically necessary to regulate the DC-link current [5].

In order to selectively eliminate specific low-order PWM current harmonics, SHE incorporates the use of switching angles to define the position of PWM current pulses. While the initiation and termination points of each PWM current pulse correspond to distinct switching angles, SHE utilizes a limited number of independent switching angles, upon which all others are related [5, 22]. Depending on the number of harmonics targeted

for elimination, the number of independent switching angles will vary proportionally [5,22, 23]. For instance, to eliminate k harmonics, k independent switching angles are required (e.g., θ_1, θ_2, ..., θ_k). Consequently, the number of PWM current pulses per half-cycle will also vary based on

$$N_p = 2k + 1. \tag{10}$$

Equation (10) can be combined with (5) in order to obtain an expression describing the relationship between the number of harmonics targeted for elimination by a particular SHE scheme, and its respective device switching frequency [5].

$$f_{sw} = f_1(2k + 1) \tag{11}$$

In order to satisfy the switching constraints imposed by PWM CSC-based drives, and to avoid the manifestation of even-order PWM current harmonics, the PWM current waveforms achieved through SHE exhibit both quarter-wave and half-wave symmetry [22,23]. Therefore, when using Fourier series to model the magnitudes of the PWM current harmonics targeted for elimination, the a_0 and a_n Fourier coefficients are consequently eliminated. As a result, the PWM current can be expressed as

$$i_w(\omega t) = \sum_{n=1}^{\infty} I_{wn} \sin(n\omega t) \tag{12}$$

where

$$I_{wn} = b_n = \frac{4}{\pi} \int_0^{\frac{\pi}{2}} i_w(\omega t) \sin(n\omega t)\, d(\omega t). \tag{13}$$

Equation (13) is of vital importance when solving for the switching angles of a particular SHE scheme, as it characterizes the magnitudes of the individual harmonics present in the PWM current. Using (13), a set of k nonlinear expressions, modeling the magnitudes of each of the PWM current harmonics targeted for elimination, can be derived (e.g., F_1, F_2, ..., F_k). Given that the goal is to eliminate these harmonics (i.e., reduce their magnitudes to zero), these nonlinear equations can each be initialized to zero and then

simultaneously solved, in order to determine the independent switching angles needed to achieve their elimination. However, due to the inherent non-linearity of the system of equations derived from (13), a numerical method such as the Newton-Raphson iterative algorithm must be applied to solve for the required switching angles [5,13]. A flowchart describing the general steps and decision-making processes followed by the Newton-Raphson algorithm when solving for the switching angles is shown in Fig. 11. In Fig. 11, θ^0 refers to the initial guesses of the switching angles supplied to the algorithm and $\partial F/\partial\theta$ denotes the Jacobian matrix defined by

$$\frac{\partial F}{\partial \theta} = \begin{bmatrix} \frac{\partial F_1}{\partial \theta_1} & \frac{\partial F_1}{\partial \theta_2} & \frac{\partial F_1}{\partial \theta_3} & \cdots & \frac{\partial F_1}{\partial \theta_k} \\ \frac{\partial F_2}{\partial \theta_1} & \frac{\partial F_2}{\partial \theta_2} & \frac{\partial F_2}{\partial \theta_3} & \cdots & \frac{\partial F_2}{\partial \theta_k} \\ \frac{\partial F_3}{\partial \theta_1} & \frac{\partial F_3}{\partial \theta_2} & \frac{\partial F_3}{\partial \theta_3} & \cdots & \frac{\partial F_3}{\partial \theta_k} \\ \cdots & \cdots & \cdots & \cdots & \cdots \\ \frac{\partial F_k}{\partial \theta_1} & \frac{\partial F_k}{\partial \theta_2} & \frac{\partial F_k}{\partial \theta_3} & \cdots & \frac{\partial F_k}{\partial \theta_k} \end{bmatrix}. \tag{14}$$

Provided that the initial guesses of the switching angles supplied to the Newton-Raphson iterative algorithm are satisfactory, it should converge upon a solution set consisting of switching angles which will enable elimination of the targeted PWM current harmonics. In practice, this entire process would be completed off-line, where the pre-computed switching angles would then be imported onto a digital controller for real-world implementation [5, 6]. The following two sections will apply the concepts discussed above to practical examples of SHE.

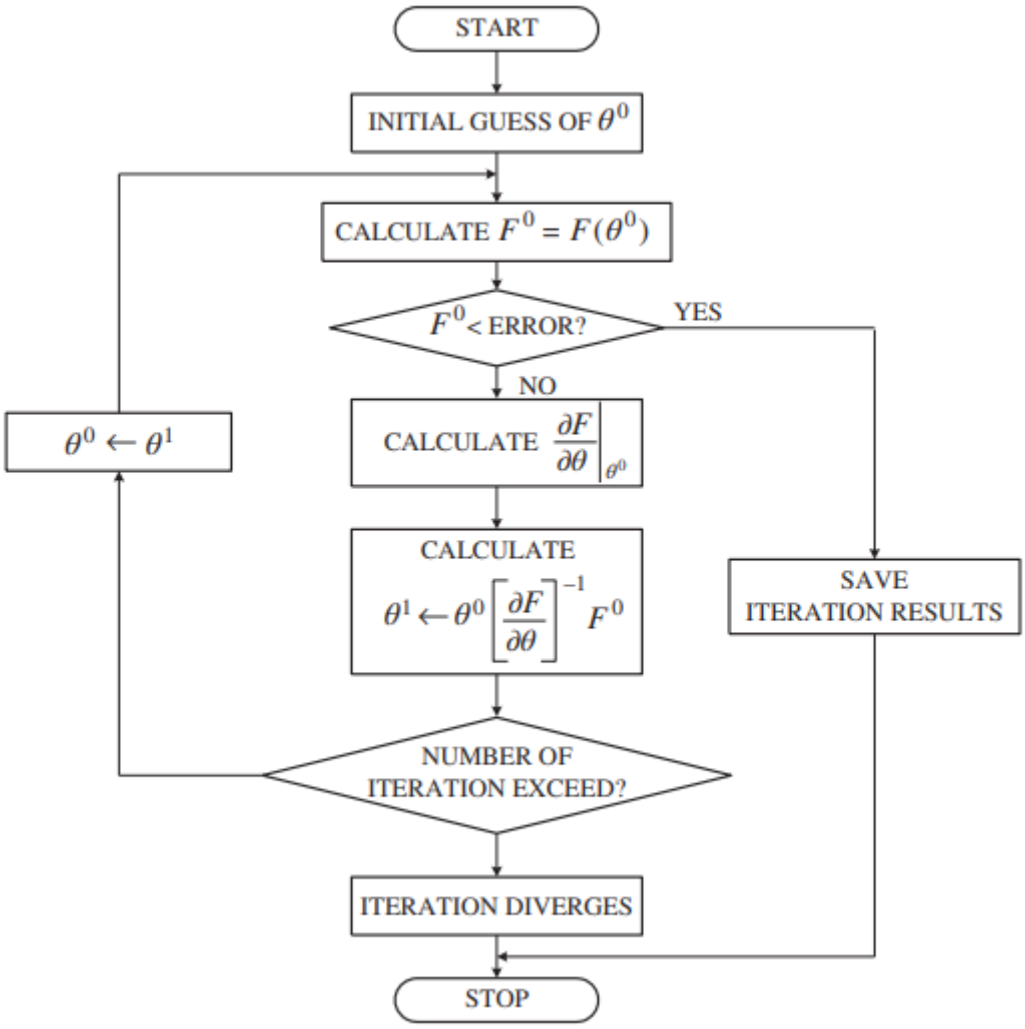

Figure 11: Flowchart showing the steps and decision-making processes followed by the Newton-Raphson iterative algorithm when used to solve for SHE switching angles [5].

1.2.3.1 SHE Without Amplitude Modulation Index Control

Fig. 12 provides an illustration of two typical PWM current waveforms achievable through $N_p = 7$ and $N_p = 9$ SHE configured without amplitude modulation index control. Based on (10) and (11), the $N_p = 7$ SHE scheme is capable of eliminating three PWM current harmonics, and given a fundamental frequency of 60 Hz, it features a device switching frequency of 420 Hz. Conversely, the $N_p = 9$ SHE scheme can eliminate four PWM current harmonics, and supports a device switching frequency of 540 Hz.

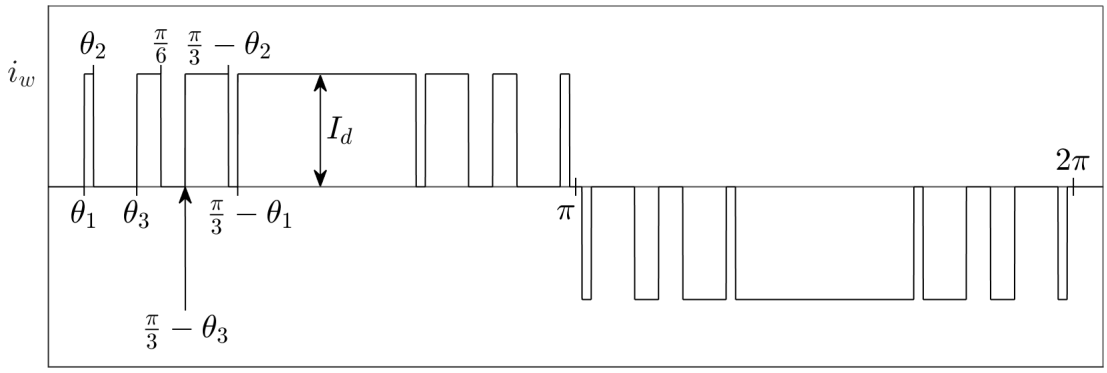

(a) $N_p = 7$ SHE

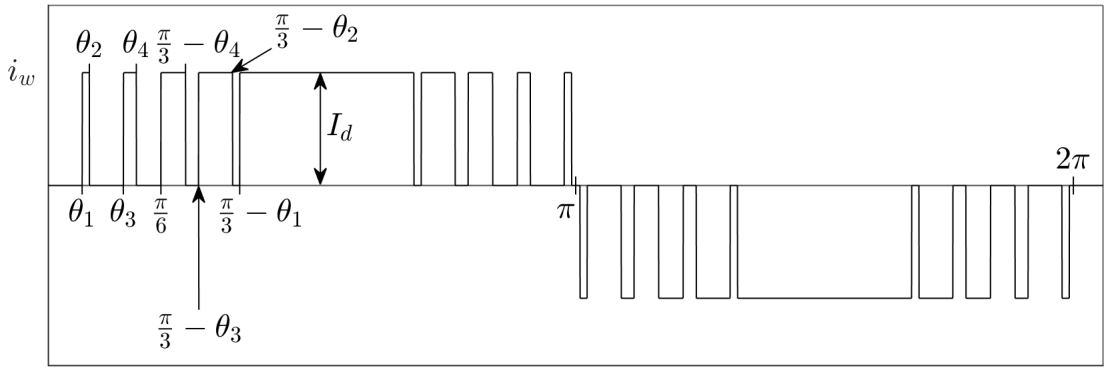

(b) $N_p = 9$ SHE

Figure 12: PWM current waveforms (i_w) generated through (a) $N_p = 7$ SHE and (b) $N_p = 9$ SHE, both configured without amplitude modulation index (m_a) control.

Supposing that the $N_p = 7$ SHE scheme shown in Fig. 12 (a) is targeting the 5th, 7th, and 11th order PWM current harmonics for elimination, the necessary independent switching angles (θ_{1-3}) can be determined by solving the following system of nonlinear equations derived from (13),

$$\begin{cases} F_1 = \cos(5\theta_1) + \cos(5(\pi/3-\theta_1)) - \cos(5\theta_2) - \cos(5(\pi/3-\theta_2)) + \cos(5\theta_3) \\ \qquad + \cos(5(\pi/3-\theta_3)) - \cos(5\pi/6) = 0 \\ F_2 = \cos(7\theta_1) + \cos(7(\pi/3-\theta_1)) - \cos(7\theta_2) - \cos(7(\pi/3-\theta_2)) + \cos(7\theta_3) \\ \qquad + \cos(7(\pi/3-\theta_3)) - \cos(7\pi/6) = 0 \\ F_3 = \cos(11\theta_1) + \cos(11(\pi/3-\theta_1)) - \cos(11\theta_2) - \cos(11(\pi/3-\theta_2)) \\ \qquad + \cos(11\theta_3) + \cos(11(\pi/3-\theta_3)) - \cos(11\pi/6) = 0. \end{cases} \tag{15}$$

In order to solve this system of transcendental equations, various different numerical methods can be used. One such method is the Newton-Raphson iterative algorithm, which converges upon the following solution set

$$\begin{cases} \theta_1 = 2.238^\circ \\ \theta_2 = 5.603^\circ \\ \theta_3 = 21.257^\circ. \end{cases} \tag{16}$$

Incorporating these switching angles into the aforementioned $N_p = 7$ SHE scheme, results in a PWM current harmonic spectrum in which the 5th, 7th, and 11th order harmonics are eliminated, as shown in Fig. 13.

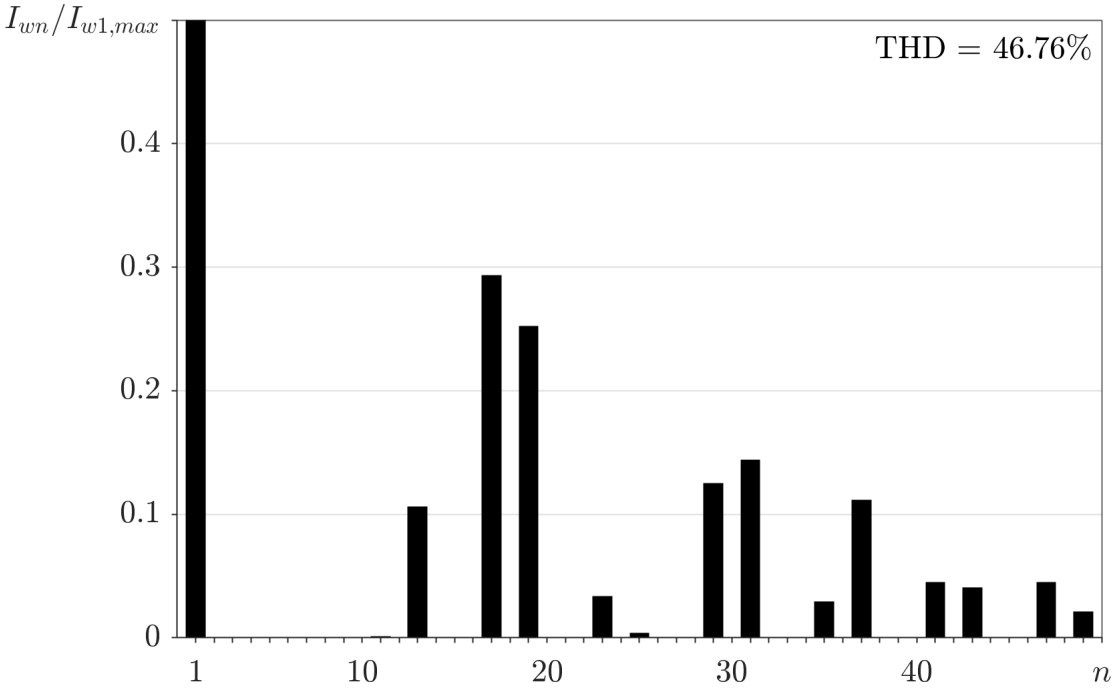

Figure 13: The PWM current (i_w) harmonic spectrum produced by $N_p = 7$ SHE configured without amplitude modulation index (m_a) control, where the 5th, 7th, and 11th order harmonics are eliminated.

A similar process can be followed in order to determine the switching angles necessary to implement the $N_p = 9$ SHE scheme shown in Fig. 12 (b) (θ_{1-4}). For this case, supposing that the 5th, 7th, 13th, and 17th PWM current harmonics are targeted for elimination, (13) can be used to derive the following system of nonlinear equations,

$$
\begin{cases}
F_1 = \cos(5\theta_1) + \cos(5(\pi/3-\theta_1)) - \cos(5\theta_2) - \cos(5(\pi/3-\theta_2)) + \cos(5\theta_3) \\
\qquad + \cos(5(\pi/3-\theta_3)) - \cos(5\theta_4) - \cos(5(\pi/3-\theta_4)) + \cos(5\pi/6) = 0 \\
F_2 = \cos(7\theta_1) + \cos(7(\pi/3-\theta_1)) - \cos(7\theta_2) - \cos(7(\pi/3-\theta_2)) + \cos(7\theta_3) \\
\qquad + \cos(7(\pi/3-\theta_3)) - \cos(7\theta_4) - \cos(7(\pi/3-\theta_4)) + \cos(7\pi/6) = 0 \\
F_3 = \cos(13\theta_1) + \cos(13(\pi/3-\theta_1)) - \cos(13\theta_2) - \cos(13(\pi/3-\theta_2)) \\
\qquad + \cos(13\theta_3) + \cos(13(\pi/3-\theta_3)) - \cos(13\theta_4) - \cos(13(\pi/3-\theta_4)) \\
\qquad + \cos(13\pi/6) = 0 \\
F_4 = \cos(17\theta_1) + \cos(17(\pi/3-\theta_1)) - \cos(17\theta_2) - \cos(17(\pi/3-\theta_2)) \\
\qquad + \cos(17\theta_3) + \cos(17(\pi/3-\theta_3)) - \cos(17\theta_4) - \cos(17(\pi/3-\theta_4)) \\
\qquad + \cos(17\pi/6) = 0.
\end{cases}
\tag{17}
$$

By applying the Newton-Raphson iterative algorithm to (17), the following switching angles are obtained

$$
\begin{cases}
\theta_1 = 1.496^\circ \\
\theta_2 = 4.141^\circ \\
\theta_3 = 16.400^\circ \\
\theta_4 = 21.118^\circ.
\end{cases}
\tag{18}
$$

As shown in Fig. 14, by utilizing these switching angles in the model $N_p = 9$ SHE switching scheme, the 5th, 7th, 13th, and 17th order PWM current harmonics are completely eliminated.

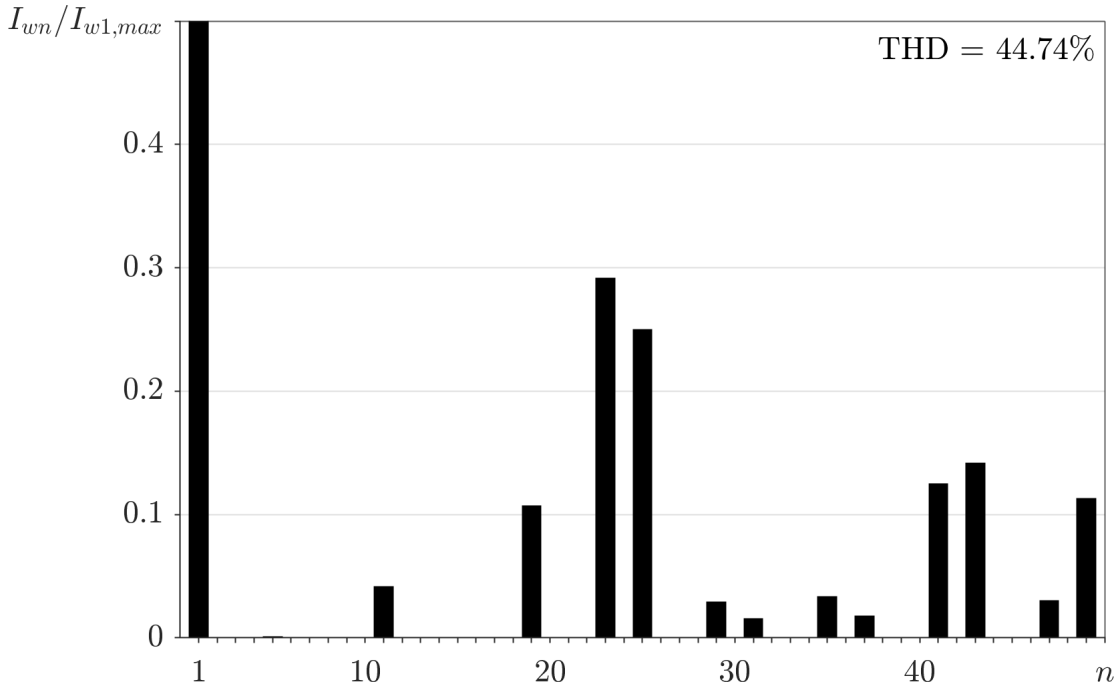

Figure 14: The PWM current (i_w) harmonic spectrum produced by $N_p = 9$ SHE configured without amplitude modulation index (m_a) control, where the 5th, 7th, 13th, and 17th order harmonics are eliminated.

1.2.3.2 SHE With Amplitude Modulation Index Control

When considering SHE configured with amplitude modulation index control, one of the switching angles which would otherwise be used to eliminate an additional harmonic, is instead reserved to control the magnitude of the PWM currents fundamental harmonic. Thus, $k - 1$ PWM current harmonics can be eliminated using k switching angles for these cases [5]. Additionally, in order to fully control the magnitude of the PWM currents fundamental harmonic, this variant of SHE introduces a bypass pulse of variable width, within the center $\pi/3$ interval of each half-cycle of the PWM current [5]. This is illustrated in Fig. 15, which shows the half-cycle waveforms generated by $N_p = 8$ SHE configured with amplitude modulation index control. This $N_p = 8$ SHE scheme is capable of eliminating three PWM current harmonics, while simultaneously supporting amplitude modulation index control. Furthermore, given a fundamental frequency of 60 Hz, this SHE scheme features a device switching frequency of 480 Hz.

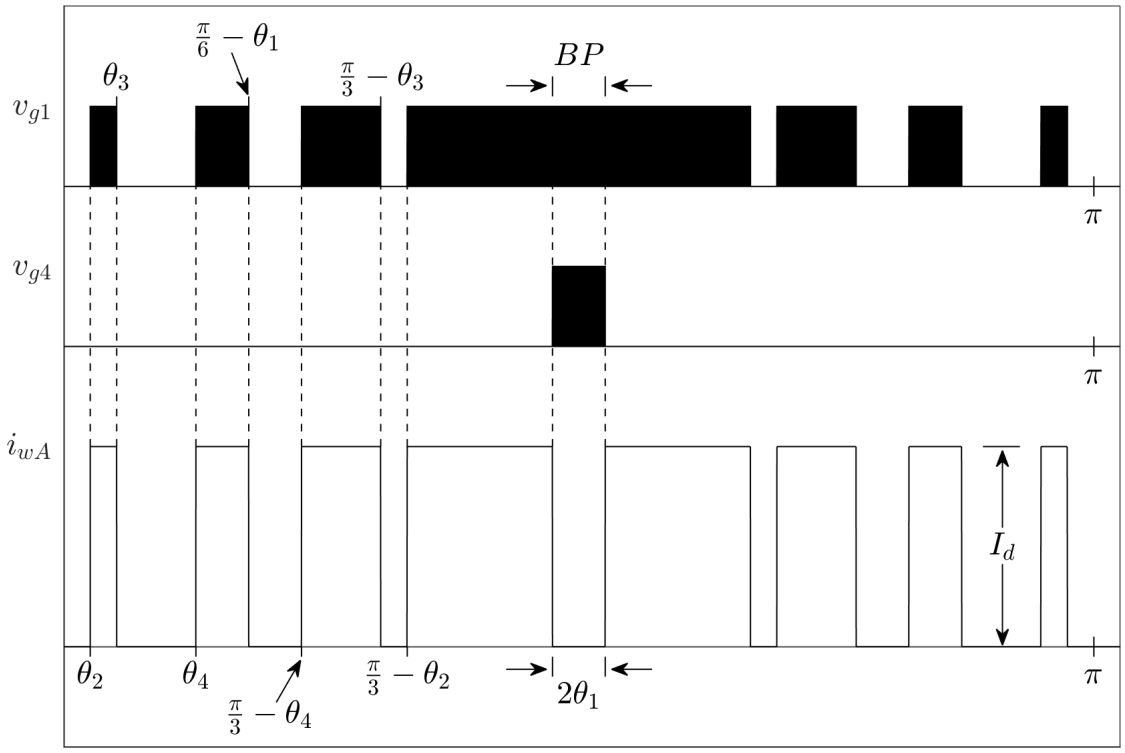

Figure 15: Half-cycle waveforms of the phase-A PWM current (i_{wA}) and its respective gating signals ($v_{g1,4}$), generated through $N_p = 8$ SHE configured with amplitude modulation index (m_a) control.

As an example, assuming that the $N_p = 8$ SHE scheme presented in Fig. 15 is meant to eliminate the 5th, 7th, and 11th order PWM current harmonics, while also providing amplitude modulation index control, (13) can be used to derive a set of nonlinear equations representing the magnitudes of the fundamental, and each of the harmonics targeted for elimination.

$$
\begin{cases}
F_1 = \cos(\theta_2) - \cos(\theta_3) + \cos(\theta_4) - \cos(\pi/6 - \theta_1) + \cos(\pi/3 - \theta_4) \\
\qquad - \cos(\pi/3 - \theta_3) + \cos(\pi/3 - \theta_2) - \cos(\pi/2 - \theta_1) = m_a\pi/4 \\
F_2 = \cos(5\theta_2) - \cos(5\theta_3) + \cos(5\theta_4) - \cos(5(\pi/6 - \theta_1)) + \cos(5(\pi/3 - \theta_4)) \\
\qquad - \cos(5(\pi/3 - \theta_3)) + \cos(5(\pi/3 - \theta_2)) - \cos(5(\pi/2 - \theta_1)) = 0 \\
F_3 = \cos(7\theta_2) - \cos(7\theta_3) + \cos(7\theta_4) - \cos(7(\pi/6 - \theta_1)) + \cos(7(\pi/3 - \theta_4)) \\
\qquad - \cos(7(\pi/3 - \theta_3)) + \cos(7(\pi/3 - \theta_2)) - \cos(7(\pi/2 - \theta_1)) = 0 \\
F_4 = \cos(11\theta_2) - \cos(11\theta_3) + \cos(11\theta_4) - \cos(11(\pi/6 - \theta_1)) \\
\qquad + \cos(11(\pi/3 - \theta_4)) - \cos(11(\pi/3 - \theta_3)) + \cos(11(\pi/3 - \theta_2)) \\
\qquad - \cos(11(\pi/2 - \theta_1)) = 0
\end{cases}
\tag{19}
$$

As shown in (19), given that the magnitude of the PWM currents fundamental harmonic is adjusted by varying the amplitude modulation index, its magnitude expression (i.e., F_1) is initialized to m_a, while the others are set to zero. For SHE, the amplitude modulation index is defined by (9) as well [5, 22]. Furthermore, changes to the amplitude modulation index term in (19) will result in different solution sets when applying a numerical method like the Newton-Raphson iterative algorithm. Therefore, in order to determine the switching angles needed to establish different operating points, the switching angles must be solved for at different values of the amplitude modulation index, that span the entire operating range [5]. By applying this concept to the model $N_p = 8$ SHE scheme, the switching angle trajectories illustrated in Fig. 16 are obtained.

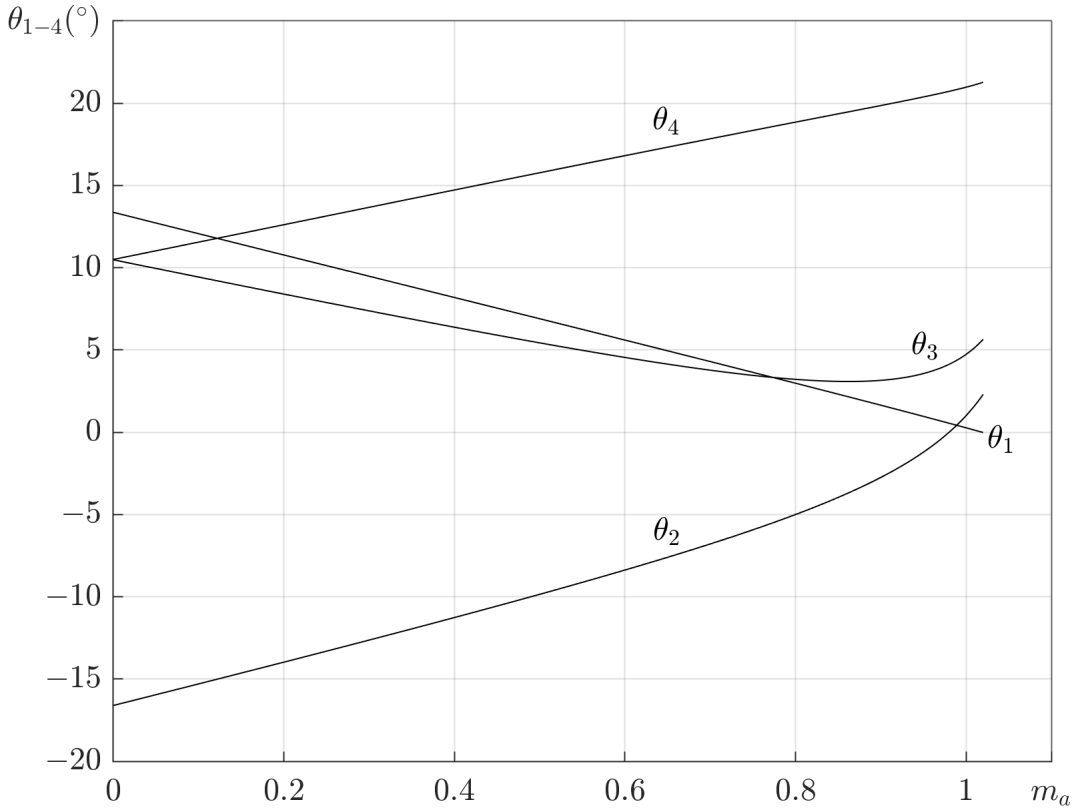

Figure 16: Trajectories of the SHE switching angles used to eliminate the output PWM currents (i_w) 5th, 7th, and 11th order harmonics, and control the magnitude of its fundamental ($N_p = 8$).

The following independent switching angles were determined by applying the Newton-Raphson iterative algorithm to (19), while the amplitude modulation index was set to 0.8,

$$\begin{cases} \theta_1 = 2.996^\circ \\ \theta_2 = -5.016^\circ \\ \theta_3 = 3.222^\circ \\ \theta_4 = 18.842^\circ. \end{cases} \tag{20}$$

Implementation of these switching angles results in a PWM current harmonic spectrum where the 5th, 7th, and 11th order harmonics are eliminated, and the normalized fundamental harmonic is reduced to approximately 0.8, as shown in Fig. 17.

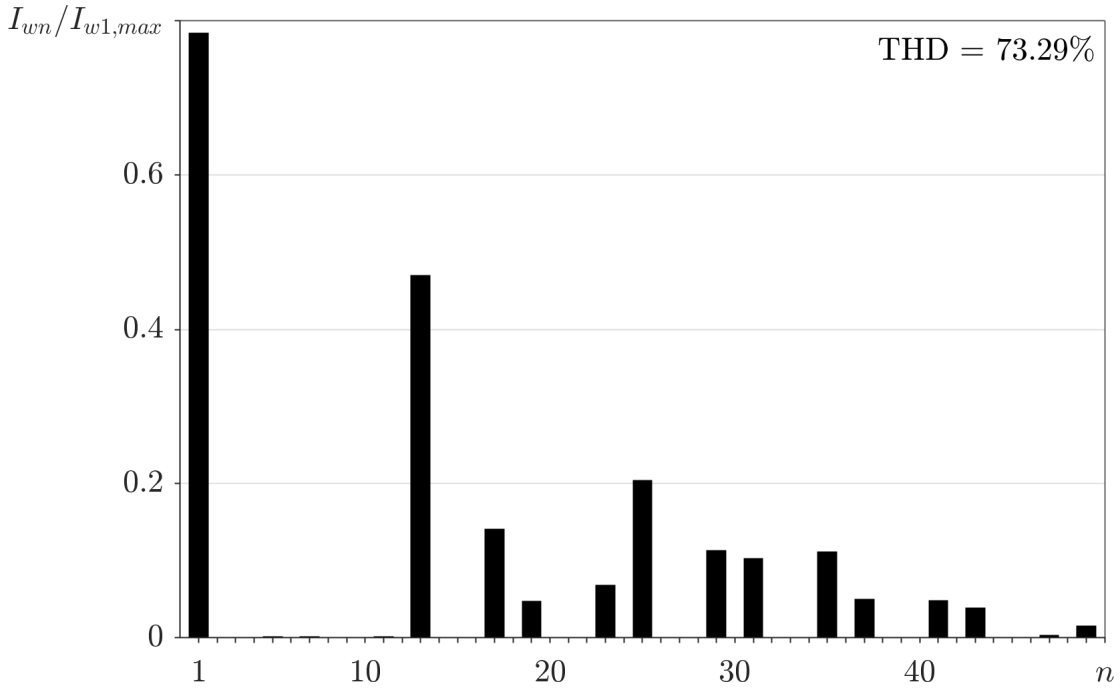

Figure 17: The PWM current (i_w) harmonic spectrum produced by $N_p = 8$ SHE configured with amplitude modulation index (m_a) control, where the 5th, 7th, and 11th order harmonics are eliminated ($m_a = 0.8$).

1.2.4 Overview

Each of the three main modulation schemes used in high-power, MV PWM CSC-based drives (i.e., SHE, SVM, and TPWM), can be evaluated based on their DC current utilization, dynamic performance, and harmonic performance [5, 13]. In the context of PWM CSIs, DC current utilization is defined as the ratio of the maximum magnitude of the PWM currents fundamental harmonic versus the available DC-link current, or $I_{w1,max}/I_d$ [5]. Furthermore, dynamic performance refers to the speed and accuracy with which the modulation scheme can respond to changes in the load and maintain stable operating conditions, while harmonic performance is a measure of the modulation schemes ability to suppress or eliminate unwanted harmonics [5].

Table 2 summarizes and compares the DC current utilization, dynamic performance, and harmonic performance, of SHE, SVM, and TPWM at similar device switching frequencies, along with providing information regarding how they can each be implemented digitally, and whether or not they feature bypass operation. Note that it is difficult to numerically quantify dynamic and harmonic performance, seeing as they both greatly de-

pend on the specifications and ratings of the overall system. Hence, in order to compare the harmonic performance of the modulation schemes included in Table 2, broad terms like "best" and "good" are used to demonstrate how each of the modulation schemes generally perform with respect to one another. Similarly, the dynamic performance of the three modulation schemes is simply ranked from high to low.

Table 2: Summary and comparison of conventional PWM CSI modulation schemes [5, 13].

Characteristics	SHE	TPWM	SVM
DC Current Utilization ($I_{w1,max}/I_d$)	0.721	0.743	0.707
Device Switching Frequency (f_{sw})	420 Hz	420 Hz	480 Hz
Dynamic Performance	Low	Medium	High
Digital Implementation	Look-up table	Real-time	Real-time
Harmonic Performance	Best	Good	Adequate
DC Current Bypass Operation	No	No	Yes

1.2.5 Practical Implementation

In commercial high-power, MV PWM CSC-based drives, the three main modulation schemes discussed in Sections 1.2.1 to 1.2.4 are uniquely applied to both the front-end PWM CSR, and the motor-side PWM CSI. SHE configured with amplitude modulation index control is commonly used to modulate the front-end PWM CSR, due to its ability to eliminate problematic low-order harmonics, located close to the resonance frequency of the input LC filter, and because it offers full control over the DC-link current [5, 13]. At the other end of the drive, modulation of the motor-side PWM CSI typically involves a unified approach where different modulation schemes are applied based on the desired

output frequency of the inverter [5, 13]. At low inverter output frequencies (e.g., $f_1 < 38$ Hz), TPWM or SVM are typically used, while at high inverter output frequencies, SHE configured without amplitude modulation index control is employed [5, 13]. An example of such a modulation strategy is shown in Fig. 18.

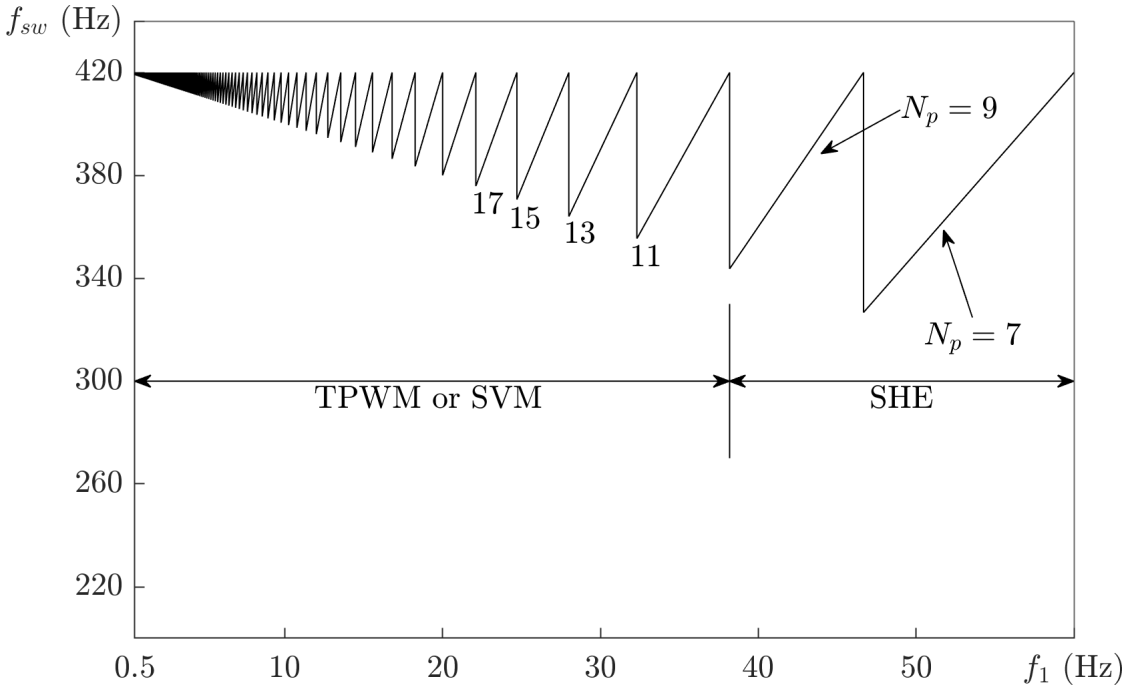

Figure 18: Typical motor-side PWM CSI modulation strategy.

1.3 Literature Review

The main emphasis of recent research on SHE with regards to implementation in PWM CSC-based drives, has been on addressing its inability to suppress both grid and DC-link background harmonics. These background harmonics compromise the performance of PWM CSC-based drives as they can resonate with the front-end PWM CSRs input LC filter, causing significant line current distortion [24]. To address the problems posed by grid-side background harmonics, in low-switching frequency CSC applications, a selective harmonic compensation (SHC) scheme was proposed in [24]. This proposed modulation scheme relaxes the PWM current quarter-wave symmetry constraints imposed by conventional SHE, and by doing so provides control over both the magnitude and phase of selected harmonics (e.g., 5th and 7th). This added phase angle control makes it possible for the grid-interfacing converter to effectively suppress problematic background harmon-

ics generated by the grid. While this scheme can, in theory, be extended to compensate multiple harmonics at once, this requires an increasingly complex look-up table that exceeds practical limits. For instance, to simultaneously compensate two harmonics using this technique, a four-dimensional look-up table is required [25–27]. Additional SHC schemes, like those covered in [25] and [26], have been proposed that improve upon the work presented in [24]. [25] introduces a harmonic suppression method that uses a phase angle compensation signal to generate an altered SHE PWM waveform that is capable of actively compensating a chosen harmonic. This approach eliminates the need for a large look-up table as required by [25], and features real-time harmonic compensation. However, this method cannot compensate two harmonics simultaneously, which is the basis of the SHC scheme outlined in [26]. [26] proposes a combination approach that uses both of the SHC schemes presented in [24] and [25] together, to each target a respective harmonic, thus enabling compensation of two harmonics in total. While this SHC scheme is effective at compensating two harmonics at once, its reliance on accurate detection of the grid frequency in real-time can be seen as a flaw when considering weak grid applications [27]. As a result, [27] proposes a more robust dual-harmonic compensation scheme that incorporates the work of [24], and introduces a bypass pulse that is actively injected to compensate for an additional harmonic. In addition to the SHC schemes outlined previously, [28] and [29] have also proposed promising virtual impedance-based selective harmonic compensation (VI-SHC) control schemes. Recently too, a model predictive switching pattern control (MPSPC) scheme was introduced for PWM CSC-based drives in [30], which utilizes an SVM-based SHE modulation scheme. This proposed scheme features excellent low-order harmonic performance during steady-state, as a result of the implemented SHE, along with improved dynamic performance, courtesy of the model predictive control (MPC) [30]. In comparison to alternative, pre-existing MPC schemes, this method eliminates steady-state quantization error and does not incorporate a weighting factor, both of which were seen as major drawbacks [30]. Nonetheless, effective on-line implementation of SHE for use in commercial high-power, MV PWM CSC-based drives continues to be a major challenge that has yet to be solved.

1.4 Research Objective

Of the three major modulation schemes used in MW-level, MV PWM CSC-based drives, SHE offers the best harmonic performance due to its ability to eliminate a number of low-order PWM current harmonics, all while preserving a low device switching frequency [5, 6, 13]. Unfortunately, however, due to its inherent off-line implementation, SHE suffers from poor dynamic performance and in certain cases (e.g., when configured with amplitude modulation index control) requires a large, memory-exhaustive look-up table [5, 6, 13, 31–33]. This research aims to address both of these issues by investigating ways of improving the dynamic performance of conventional SHE through on-line (i.e., real-time) implementation. Two new modulation schemes are proposed in this thesis: on-line SHE for modulation of the grid-side PWM CSR and SHE-TPWM for modulation of the motor-side PWM CSI. The proposed on-line SHE scheme models the independent switching angles used in conventional SHE as polynomial functions by applying curve-fitting techniques. This method of implementation improves the dynamic performance of conventional SHE, as it enables real-time computation of switching angles, and eliminates the need for look-up tables. Conversely, the proposed SHE-TPWM scheme combines the principles, while retaining the respective advantages, of both conventional SHE and TPWM. This integrative approach enables SHE-TPWM to possess SHE-level harmonic performance, along with improved dynamic performance rivaling that of TPWM.

1.5 Thesis Organization

This thesis is divided into four chapters, Chapter 1 introduces high-power, MV PWM CSC-based drives and their modulation schemes (e.g., SHE, SVM, and TPWM). Chapter 1 also provides an overview of modern research focused on improving CSC-based SHE and highlights the objectives of the research presented in this thesis. Chapters 2 and 3 introduce and examine both the theoretical and practical performance of the proposed on-line SHE and SHE-TPWM schemes. Lastly, Chapter 4 summarizes the findings of the research presented in this thesis and provides some conclusions.

2 Chapter 2 - On-line SHE

2.1 Motivation

In high-power, MV PWM CSC-based drives, SHE configured with amplitude modulation index control is commonly used to modulate the front-end PWM CSR as it possesses the ability to eliminate problematic low-order harmonics, while also offering full control over the DC-link current [5,13]. To practically implement this variant of SHE, the switching angles solved for at discrete values of the amplitude modulation index, across its full operating range (e.g., $m_a = 0$, 0.01, 0.02, 0.03, ..., 0.99, 1), must be pre-computed off-line, and then stored within a look-up table on the digital controller [6,31–33]. This method of implementation possesses a number of drawbacks, including poor dynamic performance due to its off-line nature, limited accuracy as its impossible to sample and store an infinite number of switching angles to correspond to every possible value of the amplitude modulation index, and considerable memory usage resulting from the inherently large look-up table [5, 13, 31]. In order to address these issues, an on-line SHE scheme is proposed here, which retains the same superior harmonic performance of conventional SHE, while offering improved (i.e., more accurate) dynamic performance.

2.2 Principle

As previously shown in Section 1.2.3.2, the switching angles solved for at different values of the amplitude modulation index can be plotted with respect to the amplitude modulation index, forming unique curves such as those illustrated in Fig. 16. By applying curve fitting software, such as MATLABs "polyfit" function, to these curves, each of the independent switching angles can then be realized as polynomial functions of the amplitude modulation index. For cases such as this, where the number of data points supplied to the "polyfit" function is greater than the pre-determined order of the resultant polynomial, MATLABs "polyfit" function uses polynomial regression to fit a least-squares nth order polynomial to the input data vectors [34]. When applied to the switching angle curves constituent to the $N_p = 8$ SHE scheme shown in Fig. 16, the "polyfit" function

returns the following polynomial functions,

$$\begin{cases} \theta_1(m_a) = -0.6619m_a^3 + 0.6975m_a^2 - 13.1311m_a + 13.3899 \\ \theta_2(m_a) = 132.6456m_a^6 - 342.0784m_a^5 + 338.8464m_a^4 - 156.5410m_a^3 \\ \qquad\qquad +34.5514m_a^2 + 10.0973m_a - 16.5555 \\ \theta_3(m_a) = 147.3898m_a^6 - 380.7062m_a^5 + 377.5167m_a^4 - 174.6484m_a^3 \\ \qquad\qquad +38.4041m_a^2 - 13.8078m_a + 10.5617 \\ \theta_4(m_a) = 0.3516m_a^3 - 0.7772m_a^2 + 10.8704m_a + 10.4712. \end{cases} \tag{21}$$

Each of the polynomial expressions shown in (21) are able to accurately model their respective switching angle curves to within an accuracy of ± 0.25 degrees. This is illustrated in Fig. 19, where the absolute error between the actual switching angles and their approximated values ($|\Delta\theta|$), as determined using (22), is plotted with respect to the amplitude modulation index.

$$|\Delta\theta| = |\theta_{\text{approximate}} - \theta_{\text{actual}}| \tag{22}$$

The absolute error between the actual switching angles and their polynomial-generated counterparts shown in Fig. 19, can be even further reduced by increasing the order of the polynomial expressions presented in (21). However, by increasing the order of these polynomial expressions, this adds further computational burden to the digital controller, slowing its ability to re-compute switching angles in real-time. Thus, when taking this trade-off into consideration, the polynomial expressions shown in (21) offer a good balance between accuracy and simplicity. This statement is substantiated by the results shown in Fig. 20, which compares the low-order PWM current harmonics produced through conventional $N_p = 8$ SHE, to those generated by an equivalent on-line SHE scheme using the polynomial expressions introduced in (21).

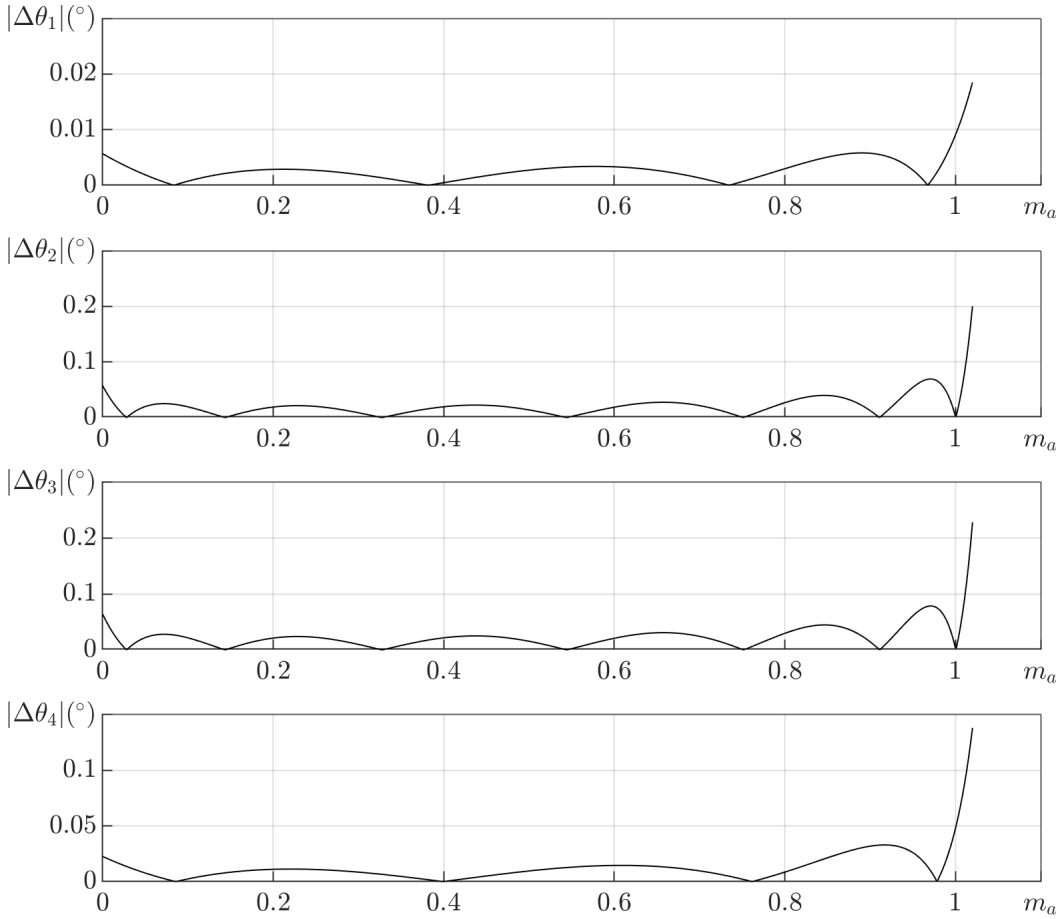

Figure 19: The absolute error ($|\Delta\theta|$) between the actual switching angles (θ_{actual}) and their polynomial approximations ($\theta_{\text{approximate}}$).

As shown in Fig. 20, through implementation of the "polyfit" generated expressions shown in (21), the proposed on-line SHE scheme is able to effectively replicate the low-order harmonic performance of conventional SHE. Where the 5th, 7th, and 11th order PWM current harmonics are all eliminated, and the PWM currents fundamental harmonic varies linearly in proportion to the amplitude modulation index. In addition, the proposed on-line SHE scheme features the ability to re-compute switching angles in real-time (i.e., on-line), which eliminates the need to store discrete values of the switching angles in large look-up tables, thus providing improved dynamic performance.

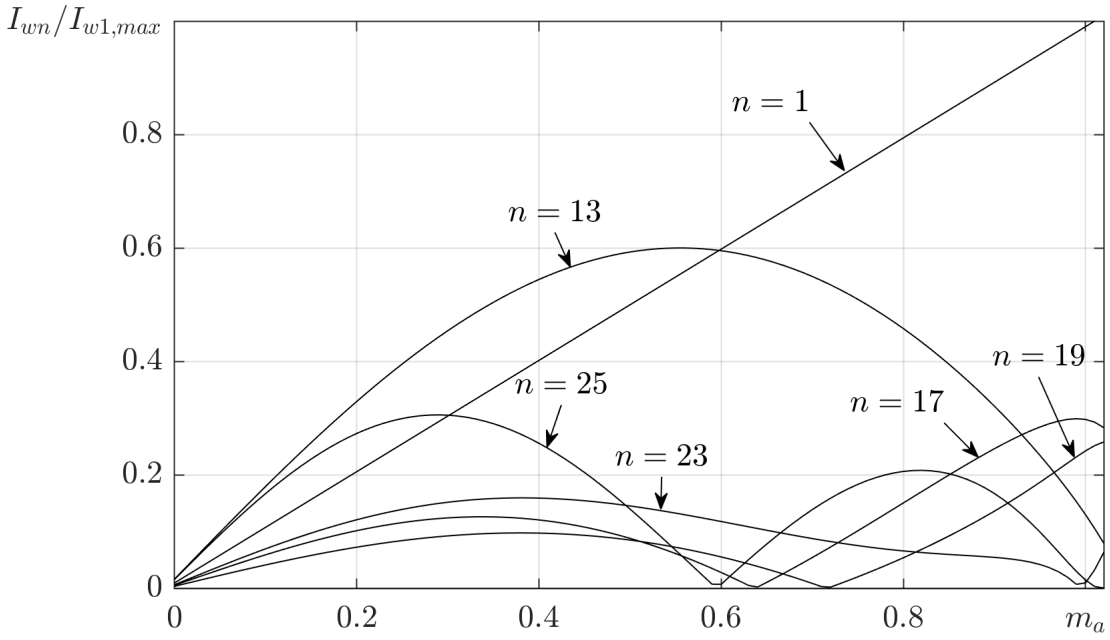

(a) Conventional SHE

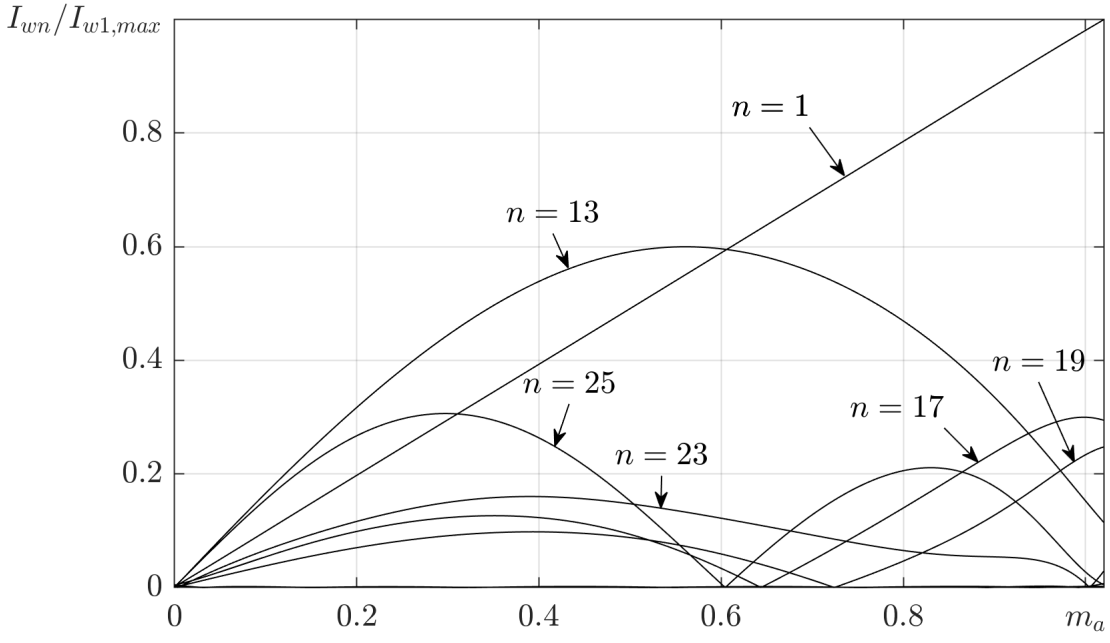

(b) On-Line SHE

Figure 20: Comparison of the low-order PWM current (i_w) harmonic content produced through (a) conventional $N_p = 8$ SHE, and (b) the proposed on-line SHE scheme.

When considering high switching frequency applications, the proposed on-line SHE scheme possesses the same limits as conventional SHE, as they both rely on the same initial off-line setup. This setup, which is outlined in Section 1.2.3.1, encounters difficulties at higher switching frequencies, as the size of the system of nonlinear equations to be solved,

increases proportionally. As a result, successful convergence of the chosen numerical method (e.g., Newton-Raphson iterative algorithm) will rely heavily on the supplied initial conditions [35]. This increased sensitivity makes it difficult to effectively determine the switching angles necessary to implement either SHE scheme at high switching frequencies.

2.3 Experimental Results

2.3.1 Test Setup

In order to confirm that the theoretical performance and features of the proposed on-line SHE scheme were retained during practical implementation, multiple laboratory experiments were performed, testing the proposed on-line SHE scheme on a down-scaled PWM CSI. The PWM CSI used in these experiments was constructed using three Semikron SKM300GBD12T4 insulated gate bipolar transistor (IGBT) modules with series-connected diodes, and a front-end Semikron SKD 160 full-bridge rectifier unit. The proposed on-line SHE scheme was also implemented through a dSPACE CLP1103 controller board. Additional test setup parameters can be found in Table 3. It should be noted that while the proposed on-line SHE scheme is recommended for use in PWM CSRs, a PWM CSI was used for these experiments to limit the complexity of the test setup.

Table 3: On-Line SHE experimental test setup parameters.

Parameters	Experimental Values
Maximum DC-Link Current (I_d)	10 A
DC-Link Inductance (L_d)	100 mH
Filter Capacitor (C_f)	100 μF
Load Inductance (L_s)	10 mH
Load Resistance (R_s)	5 Ω
Fundamental Frequency (f_1)	60 Hz
Device Switching Frequency (f_{sw})	480 Hz
Number of PWM Current Pulses per Half-Cycle (N_p)	8
Overlap Time (t_{ov})	25 μs

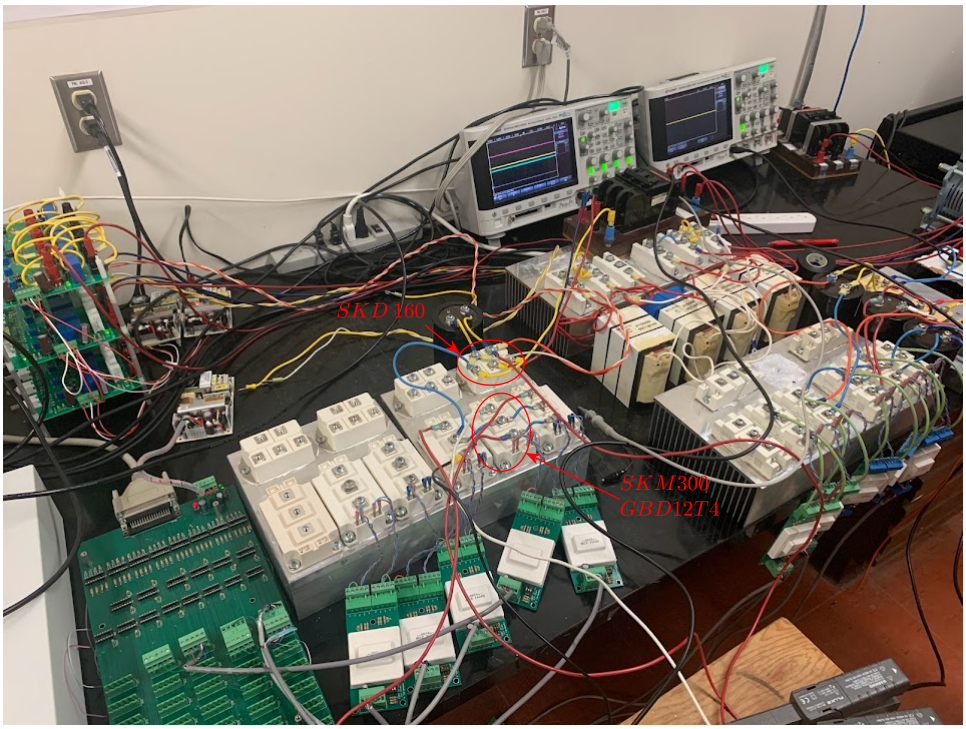

Figure 21: Active components part of the experimental test setup.

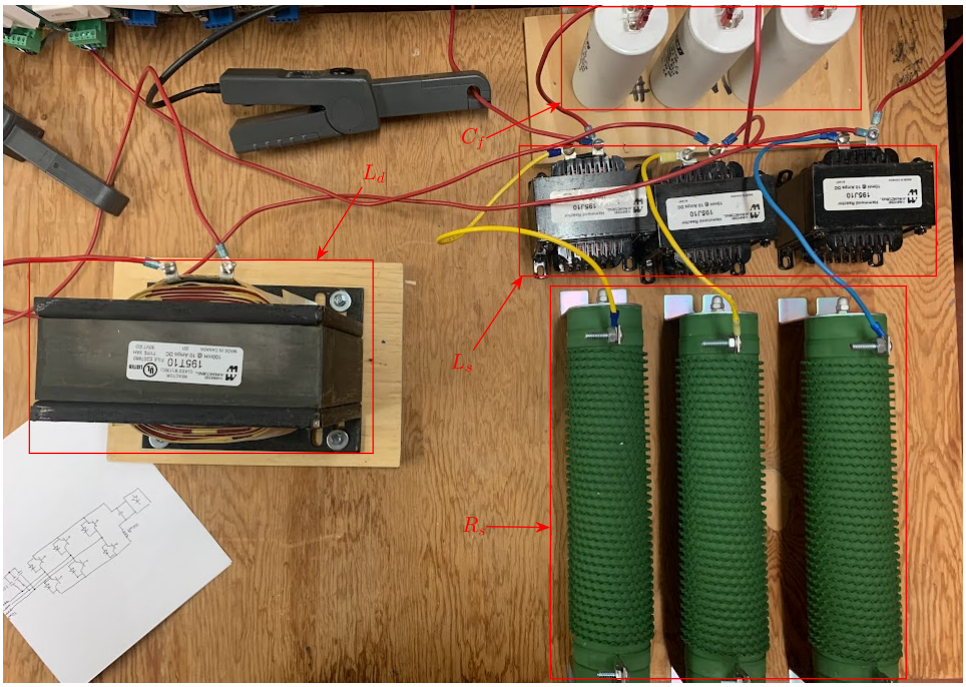

Figure 22: Passive components part of the experimental test setup.

2.3.2 Harmonic Performance

Fig. 23 shows the steady-state experimental results recorded while the proposed on-line SHE scheme was applied to the test setup with a fixed amplitude modulation index

of 0.8. From the phase-A output PWM current (i_{wA}) fast Fourier transform (FFT), it is clear that 5th, 7th, and 11th order PWM current harmonics are each approximately zero. The reason for these low-order harmonics not being completely eliminated, results from the overlap time added to the generated gating signals in order to ensure continuity of the DC-link current. Nevertheless, these results match those achieved through conventional $N_p = 8$ SHE, thus confirming that the proposed on-line SHE scheme retains the same superior low-order harmonic performance during steady-state operation.

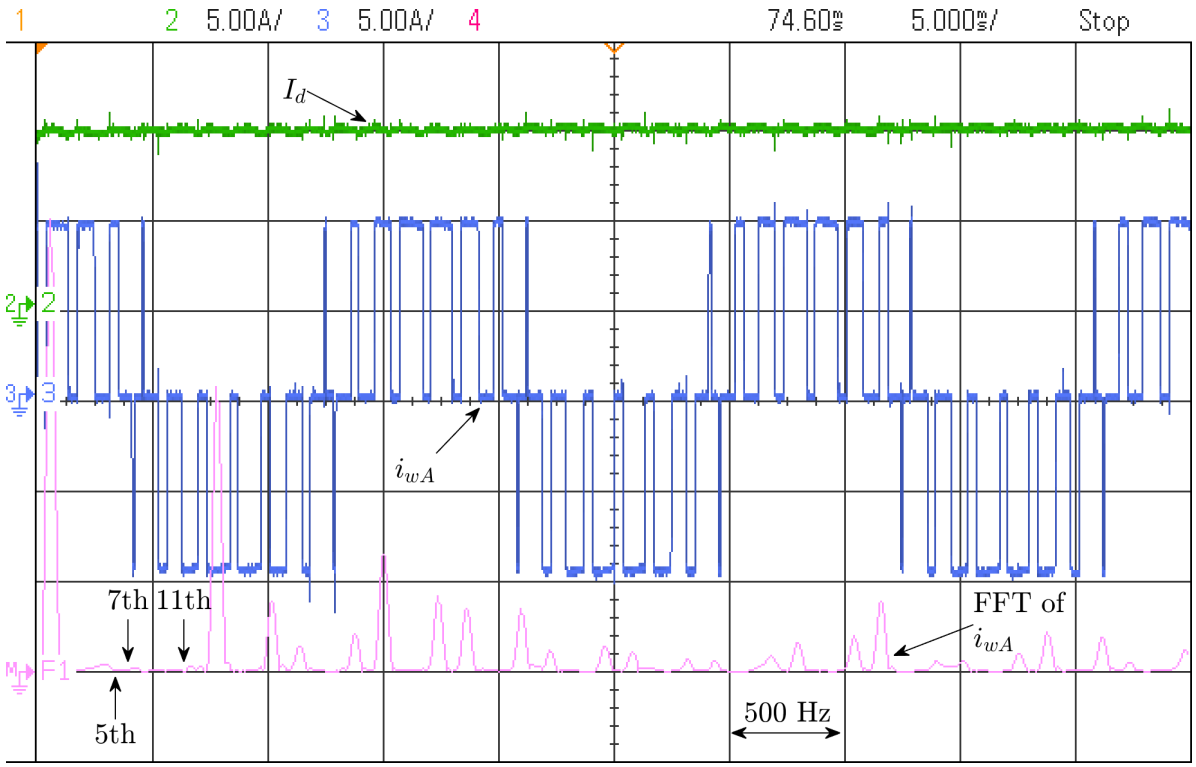

Figure 23: Experimental results showing the DC-link current (I_d) and phase-A PWM current (i_{wA}) waveforms during steady-state operation of the proposed on-line SHE scheme ($m_a = 0.8$). The FFT of the phase-A PWM current is also included.

2.3.3 Dynamic Performance

Fig. 24 presents experimental results captured while the amplitude modulation index of the proposed on-line SHE scheme was varied from 1 to 0.8. These results showcase the ability of the proposed scheme to re-compute the necessary switching angles in real-time, following changes to the amplitude modulation index, while preserving the harmonic performance of conventional SHE. This is evidenced by the included phase-A PWM current FFT, which shows that the 5th, 7th, and 11th order harmonics continue to be eliminated

while operating at both an amplitude modulation index of 1 and 0.8. Fig. 24 also includes waveforms of the S_1 gating signal (v_{g1}) and the DC-link current, as a result of the amplitude modulation index decreasing from 1 to 0.8, the S_1 gating signals bypass pulse widens, and the DC-link current increases.

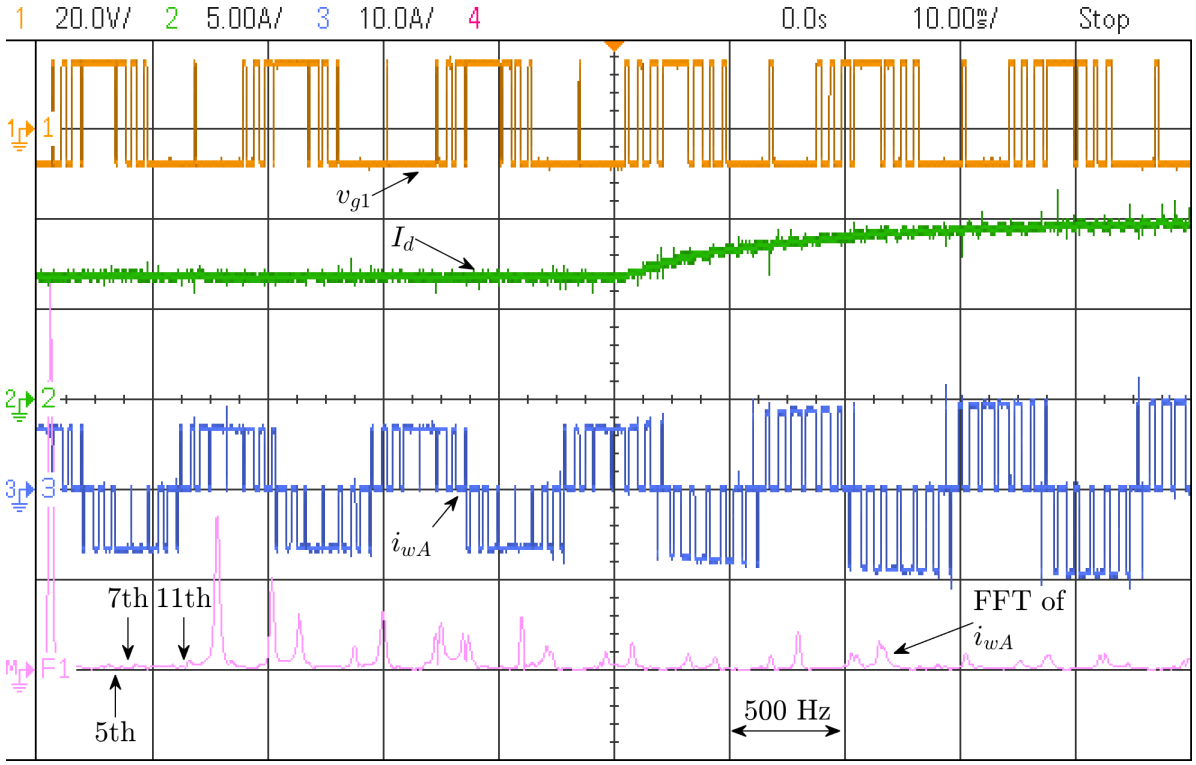

Figure 24: Experimental results showing the S_1 gating signal (v_{g1}), DC-link current (I_d), and phase-A PWM current (i_{wA}) waveforms during transient operation, where the amplitude modulation index (m_a) of the proposed on-line SHE scheme is varied from 1 to 0.8. The FFT of the phase-A PWM current is also included.

2.4 Summary

As proven by the theoretical and experimental results presented in Sections 2.2 and 2.3 above, the proposed on-line SHE scheme is able to effectively match the low-order harmonic performance of conventional SHE configured with amplitude modulation index control, while simultaneously providing on-line implementation, improved dynamic performance, and continuous amplitude modulation index control. For these reasons, the proposed on-line SHE scheme is well suited to replace conventional SHE used to modulate the front-end PWM CSRs, part of high-power, MV PWM CSC-based drives, without any penalty.

3 Chapter 3 - SHE-TPWM

3.1 Motivation

Modulation of the motor-side PWM CSI in high-power, MV PWM CSC-based drives, involves different modulation schemes that are strategically applied depending on the output frequency of the inverter [5, 13]. At low inverter output frequencies, TPWM or SVM are typically used, while at high inverter output frequencies, SHE configured without amplitude modulation index is commonly implemented [5, 13]. Either TPWM or SVM are applied at low inverter output frequencies, as under these conditions, they both exhibit passable harmonic performance, along with dynamic performance higher than that of SHE [5, 13]. However, when considering operation at high inverter output frequencies, both TPWM and SVM cannot compete with the superior low-order harmonic performance of SHE [5,13]. Nevertheless, being an inherently off-line modulation scheme, the SHE applied at high inverter output frequencies suffers from poor dynamic performance [5, 13]. To address the poor dynamic performance of SHE configured without amplitude modulation index control, a new modulation scheme referred to as SHE-TPWM is proposed here. This proposed SHE-TPWM scheme combines the principles and retains the inherent benefits of both SHE and TPWM, meaning that it features the same superior harmonic performance of conventional SHE, along with improved dynamic performance and DC current utilization inherited from TPWM.

3.2 Principle

In order to retain the superior low-order harmonic performance of conventional SHE, along with improved dynamic performance and DC current utilization rivaling that of TPWM, the proposed SHE-TPWM scheme incorporates a carrier-based modulation strategy that can be implemented within real-time. The proposed SHE-TPWM scheme replaces the trapezoidal modulating signal used in conventional TPWM, with a polynomial-based modulating signal synthesized using Lagrange interpolation. Lagrange interpolation is a method of curve-fitting used to formulate polynomial functions capable of interpo-

lating (i.e., pass through) given sets of data [36]. For instance, given a set of data points (a_0,b_0), (a_1,b_1), ..., (a_n,b_n), where the a_i terms are distinct, Lagrange interpolation can be used to generate a polynomial of the following form

$$P(x) = \alpha_n x^n + \alpha_{n-1} x^{n-1} + ... + \alpha_0 \tag{23}$$

where the polynomial coefficients (α_i) can be obtained using

$$\alpha_i = (-1)^{n-1} \frac{\det \begin{pmatrix} b_0 & b_1 & ... & b_n \\ a_0^n & a_1^n & ... & a_n^n \\ ... & ... & ... & ... \\ a_0^{i+1} & a_1^{i+1} & ... & a_n^{i+1} \\ a_0^{i-1} & a_1^{i-1} & ... & a_n^{i-1} \\ ... & ... & ... & ... \\ 1 & 1 & ... & 1 \end{pmatrix}}{\det \begin{pmatrix} a_0^n & a_1^n & ... & a_n^n \\ a_0^{n-1} & a_1^{n-1} & ... & a_n^{n-1} \\ ... & ... & ... & ... \\ 1 & 1 & ... & 1 \end{pmatrix}} . \tag{24}$$

Lagrange interpolation is a useful tool for the purposes of SHE-TPWM, as it can be used to generate a polynomial-based modulating signal capable of intersecting a particular triangular carrier signal at instances that correspond to SHE switching angles.

$$v_m(\omega t) = \alpha_n (\omega t)^n + \alpha_{n-1} (\omega t)^{n-1} + ... + \alpha_0 \tag{25}$$

To accomplish this, a set of two-dimensional data points, such as those listed in Table 4, must be formulated and used in conjunction with (24), to determine the polynomial coefficients needed to construct a modulating signal possessing the same form as (25). Referring to the data points provided in Table 4, the horizontal axis components (a_i) consist of SHE switching angles, while the vertical axis components (b_i) are determined using

$$v_{cr}(\omega t) = \frac{-2\hat{V}_{cr}}{\pi}(\sin^{-1}(\sin(3(N_p-1)\omega t))) \tag{26}$$

which is a general expression modeling the triangular carrier signal used within the first $\pi/3$ interval of the proposed SHE-TPWM scheme, where $\hat{V}_{cr}$ refers to its peak value. Note that because the proposed SHE-TPWM scheme is intended to replace conventional SHE applied to PWM CSIs at high inverter output frequencies, Table 4 only considers the cases where $N_p = 7$ and $N_p = 9$ [5, 13]. Furthermore, it can also be observed in Table 4, that additional data points are appended at the start and end of each data set, such as $(0,-\hat{V}_{cr}/2)$ and $(\pi/3,+\hat{V}_{cr}/2)$. This is done in order to prevent the manifestation of extra PWM pulses (e.g., $N_p > 7$ or $N_p > 9$) caused by inadvertent interaction between the synthesized modulating signal and its corresponding triangular carrier signal.

Table 4: Generalized data points used in the synthesis of modulating signals for the proposed SHE-TPWM scheme.

i	$N_p = 7$ (a_i,b_i)	$N_p = 9$ (a_i,b_i)
0	$(0,-\hat{V}_{cr}/2)$	$(0,-\hat{V}_{cr}/2)$
1	$(\theta_1,v_{cr}(\theta_1))$	$(\theta_1,v_{cr}(\theta_1))$
2	$(\theta_2,v_{cr}(\theta_2))$	$(\theta_2,v_{cr}(\theta_2))$
3	$(\theta_3,v_{cr}(\theta_3))$	$(\theta_3,v_{cr}(\theta_3))$
4	$(\pi/6,v_{cr}(\pi/6))$	$(\theta_4,v_{cr}(\theta_4))$
5	$(\pi/3-\theta_3,v_{cr}(\pi/3-\theta_3))$	$(\pi/6,v_{cr}(\pi/6))$
6	$(\pi/3-\theta_2,v_{cr}(\pi/3-\theta_2))$	$(\pi/3-\theta_4,v_{cr}(\pi/3-\theta_4))$
7	$(\pi/3-\theta_1,v_{cr}(\pi/3-\theta_1))$	$(\pi/3-\theta_3,v_{cr}(\pi/3-\theta_3))$
8	$(\pi/3,+\hat{V}_{cr}/2)$	$(\pi/3-\theta_2,v_{cr}(\pi/3-\theta_2))$
9	-	$(\pi/3-\theta_1,v_{cr}(\pi/3-\theta_1))$
10	-	$(\pi/3,+\hat{V}_{cr}/2)$

As suggested by the dependence of the tabulated data points on switching angles unique to certain SHE switching schemes, these data points will vary depending on the harmonics that are to be eliminated. However, there are certain SHE switching schemes that cannot be effectively implemented using the proposed SHE-TPWM scheme. These incompatible SHE switching schemes possess independent switching angles which fall outside of the bounds presented in Table 5. For the case where $N_p = 7$, these constraints limit the compatible SHE switching schemes to the following: (1) elimination of $n =$

$5, 7, 11$, or (2) elimination of $n = 5, 7, 13$. Similarly, for the $N_p = 9$ case, there are three compatible SHE switching schemes: (1) elimination of $n = 5, 7, 11, 19$, (2) elimination of $n = 5, 7, 13, 17$, or (3) elimination of $n = 5, 7, 13, 19$ [5]. The following two sections will provide examples highlighting how the proposed SHE-TPWM scheme can be implemented for the cases where $N_p = 7$ and $N_p = 9$, as well as experimental results used for practical verification.

Table 5: Independent SHE switching angle limits for compatibility with the proposed SHE-TPWM scheme.

$N_p = 7$	$N_p = 9$
$0 \leq \theta_1 < \pi/36$	$0 \leq \theta_1 < \pi/48$
$\pi/36 \leq \theta_2 < \pi/12$	$\pi/48 \leq \theta_2 < \pi/16$
$\pi/12 \leq \theta_3 < 5\pi/36$	$\pi/16 \leq \theta_3 < 5\pi/48$
-	$5\pi/48 \leq \theta_4 < 7\pi/48$

3.3 $N_p = 7$ SHE-TPWM

3.3.1 Theoretical Implementation & Results

It was determined through testing that the $N_p = 7$ SHE scheme in which the 5th, 7th, and 11th order PWM current harmonics are eliminated, provided the most promising results when incorporated into the proposed SHE-TPWM scheme. As such, it will be the focus of this section of the thesis. Fig. 25 showcases the principle of the proposed SHE-TPWM scheme, where the polynomial-based modulating signal has been synthesized following the methodology outlined above in Section 3.2, to eliminate the 5th, 7th, and 11th order PWM current harmonics. Refer to (18) to view the independent switching angles used in the synthesis of this polynomial-based modulating signal.

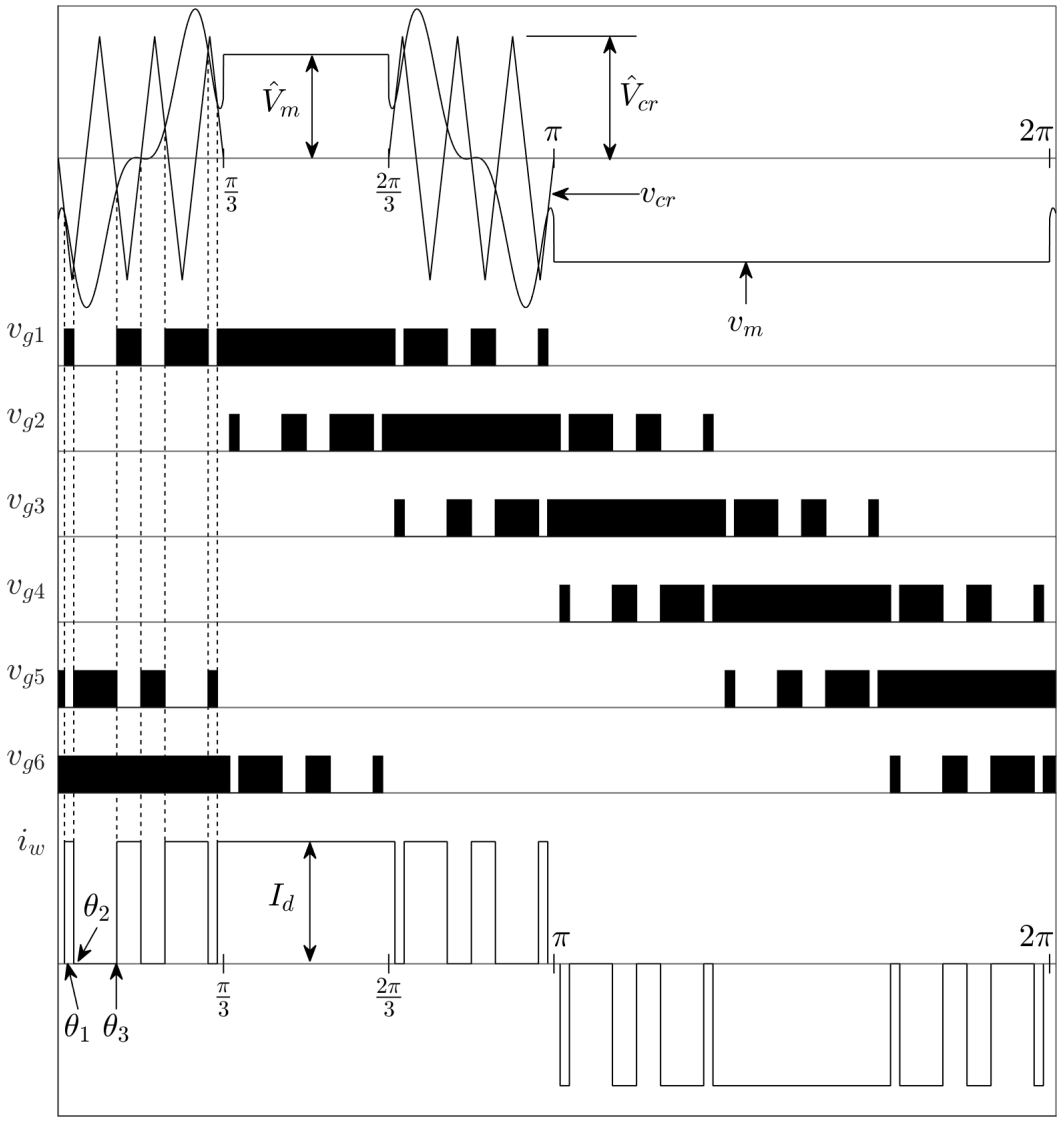

Figure 25: Principle of the proposed SHE-TPWM scheme, where the modulating signal (v_m) has been synthesized to eliminate the 5th, 7th, and 11th order PWM current (i_w) harmonics ($N_p = 7$, $m_a = 0.85$).

The SHE-TPWM scheme described in Fig. 25 features amplitude modulation index control, which is accomplished by scaling the synthesized modulating signal in proportion to the set value of the amplitude modulation index. This method of control is comparable to that which is utilized in conventional TPWM, and as such, it possesses the same limitation. This being that the magnitude of the PWM currents fundamental harmonic can only be adjusted within a limited range [5]. For this case, that range is the following:

$$0.867 I_{w1,max} \leq I_{w1} \leq I_{w1,max}. \tag{27}$$

This limitation results from the fact that neither TPWM nor SHE-TPWM implements

bypass operation. The amplitude modulation index for the proposed SHE-TPWM scheme is defined by (1) as well.

Fig. 26 compares the PWM current harmonic profiles produced by conventional SHE configured to eliminate the 5th, 7th, and 11th order PWM current harmonics (without amplitude modulation index control), conventional $N_p = 7$ TPWM, and the SHE-TPWM scheme presented in Fig. 25. In order for Fig. 26 to provide an objective comparison of the included harmonic profiles, each of the associated modulation schemes were configured to feature a DC current utilization of 0.7215, which refers to the theoretical maximum DC current utilization of the $N_p = 7$ SHE scheme under evaluation. In order to accomplish this, the amplitude modulation indices of the three modulation schemes had to be individually adjusted to the following: $m_a = 1$ for SHE, $m_a = 0.79$ for TPWM, and $m_a = 0.85$ for SHE-TPWM. Referring to Fig. 26, it is clear that while operating at a fixed amplitude modulation index of 0.85, that the proposed $N_p = 7$ SHE-TPWM scheme possesses a harmonic profile identical to that which is achieved through conventional SHE, where the 5th, 7th, and 11th order PWM current harmonics are completely eliminated. In contrast, these low-order harmonics, while low in magnitude, are still present in the harmonic profile of conventional TPWM. These results confirm that for the case where $N_p = 7$, the proposed SHE-TPWM scheme retains the ability of conventional SHE to eliminate low-order PWM current harmonics, while operating at an amplitude modulation index of 0.85.

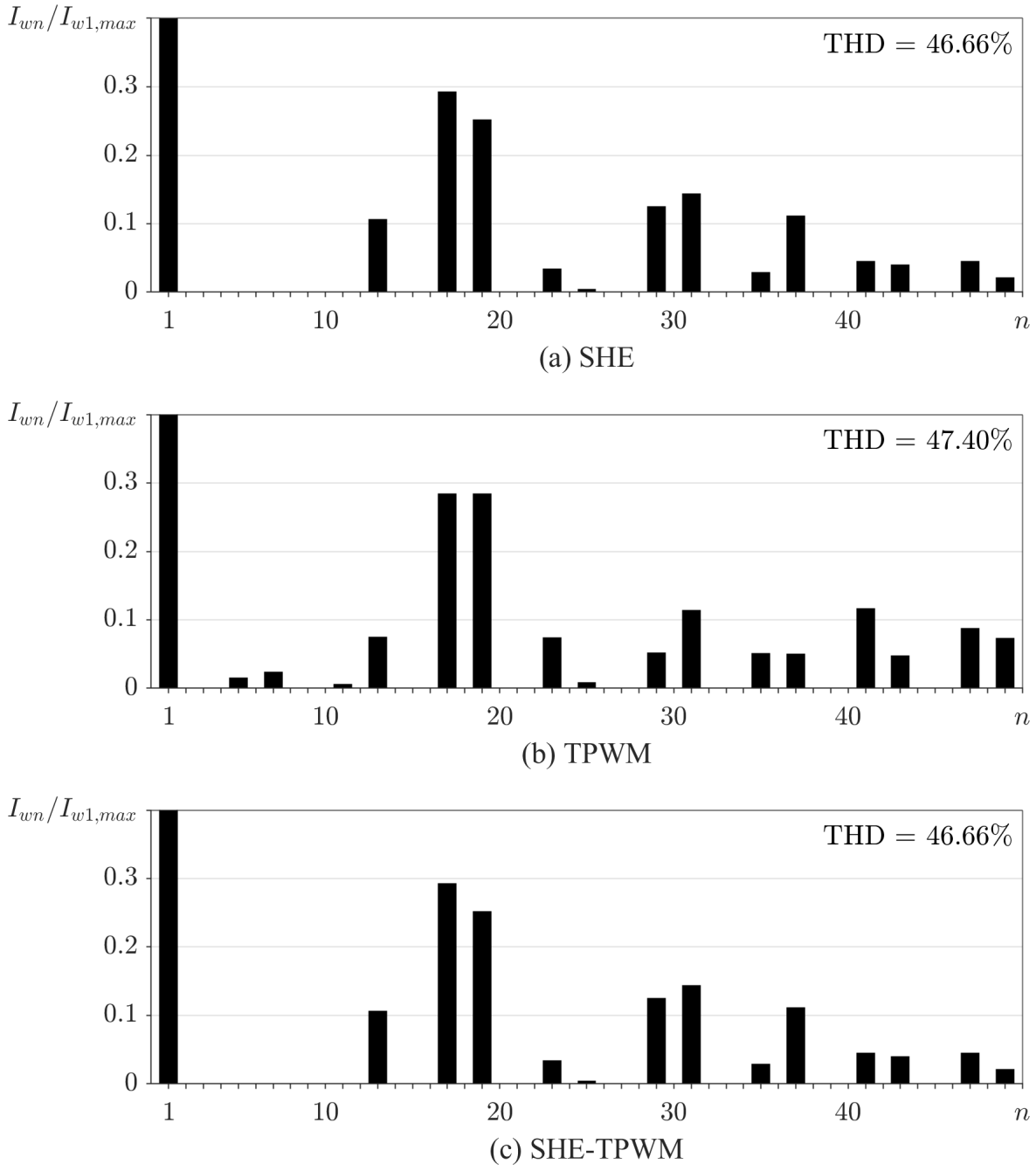

Figure 26: Harmonic profiles of (a) SHE ($m_a = 1$), (b) TPWM ($m_a = 0.79$), and (c) SHE-TPWM ($m_a = 0.85$). The DC current utilization (I_{w1}/I_d) for each modulation scheme is set to 0.7215.

Fig. 27 compares the DC current utilization and the magnitudes of the low-order PWM current harmonics (e.g., 5th, 7th, and 11th), of both the proposed SHE-TPWM scheme and conventional $N_p = 7$ TPWM, across their full ranges of operation. As can be seen, when plotted with respect to the amplitude modulation index, the DC current utilization of the proposed SHE-TPWM scheme trends similar to that of conventional TPWM, with some minor non-linear variation. In effect, the maximum DC current uti-

lization of the proposed SHE-TPWM scheme is very close to that of TPWM, thus proving that it offers better DC current utilization than conventional SHE. Referring now to the subplots comparing the magnitudes of the low-order PWM current harmonics produced by both schemes, it is evident that the 5th, 7th, and 11th order PWM current harmonics generated by the proposed SHE-TPWM scheme are virtually always lower than those produced through TPWM. As intended, these three low-order harmonics are even completely eliminated when the amplitude modulation index is set to 0.85, as under these operating conditions, the proposed SHE-TPWM scheme is able to effectively emulate conventional SHE. In order to illustrate this, Fig. 27 also includes red markers denoting the DC current utilization and low-order PWM current harmonic performance achieved through conventional SHE.

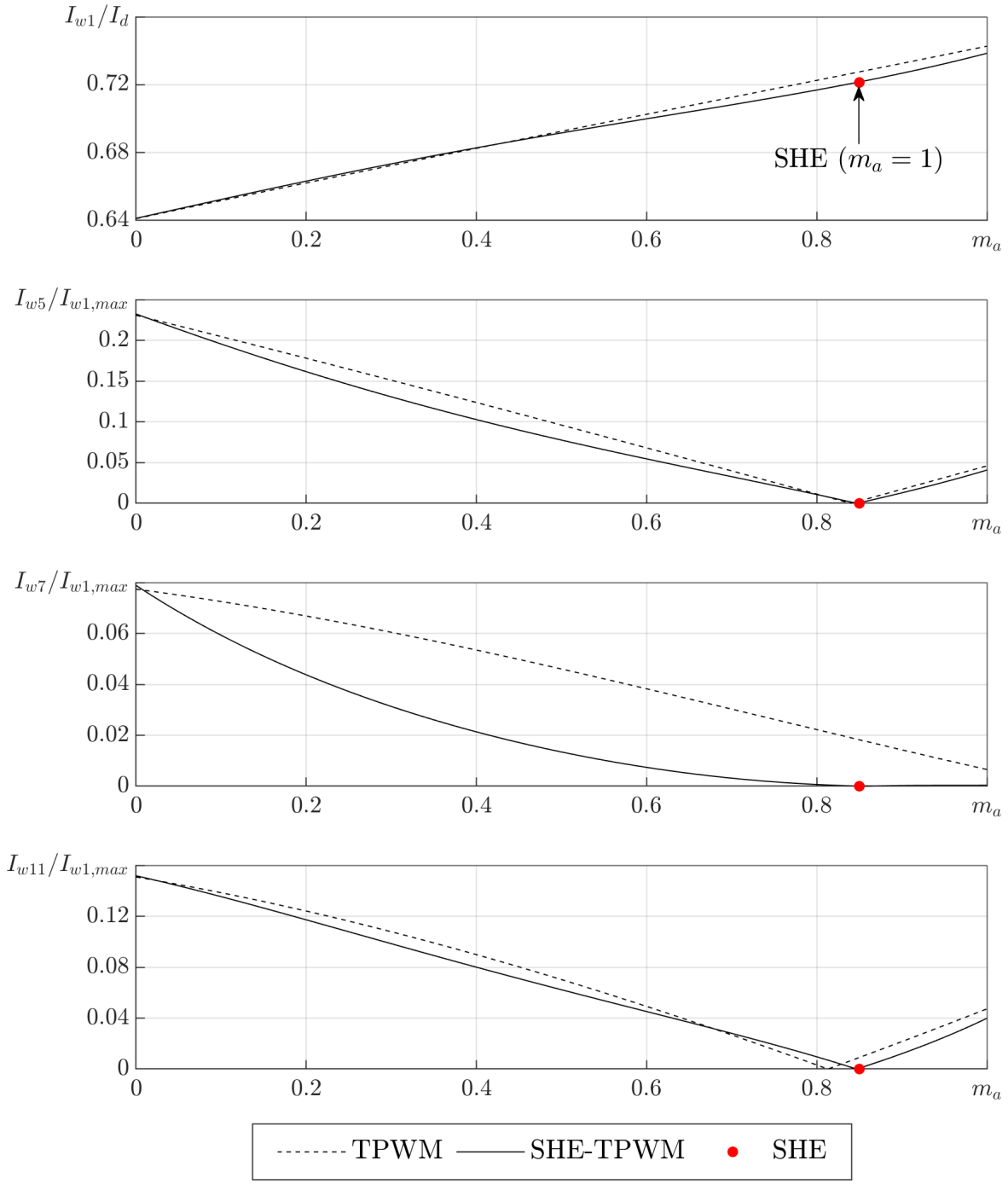

Figure 27: Comparison of the DC current utilization, as well as the low-order harmonic content of TPWM, SHE-TPWM, and SHE, across their full ranges of operation ($N_p = 7$).

3.3.2 Experimental Results

3.3.2.1 Test Setup

Experiments used to verify the performance of the proposed SHE-TPWM scheme were performed using the same test setup as described in Section 2.3, but with mild changes to certain component values, as illustrated in Table 6. For these experiments, the harmonic performance and maximum DC current utilization of the proposed SHE-TPWM scheme were tested and compared to those of conventional SHE and conventional TPWM, for the cases where $N_p = 7$ and $N_p = 9$. The dynamic performance of the proposed SHE-TPWM scheme was also assessed for both cases.

Table 6: SHE-TPWM experimental test setup parameters.

Parameters	Experimental Values
Maximum DC-Link Current (I_d)	10 A
DC-Link Inductance (L_d)	100 mH
Filter Capacitor (C_f)	100 μF
Load Inductance (L_s)	10 mH
Load Resistance (R_s)	10 Ω
Fundamental Frequency (f_1)	60 Hz
Device Switching Frequency (f_{sw})	420 Hz / 540 Hz
Number of PWM Current Pulses per Half-Cycle (N_p)	7 / 9
Overlap Time (t_{ov})	25 μs

3.3.2.2 Harmonic Performance

Figs. 28, 29, and 30 depict experimental results consisting of DC-link current and phase-A PWM current waveforms, along with FFTs of the phase-A PWM current, obtained by applying the following modulation schemes to the test setup: SHE configured to eliminate the 5th, 7th, and 11th order PWM current harmonics (without amplitude modulation index control) (Fig. 28), $N_p = 7$ TPWM (Fig. 29), and the proposed $N_p = 7$ SHE-TPWM scheme (Fig. 30). Seeing as these experimental results are meant to verify the findings presented in Fig. 26, the amplitude modulation indices of each of the aforementioned modulation schemes were configured as follows: $m_a = 1$ for SHE, $m_a = 0.79$ for TPWM, and $m_a = 0.85$ for SHE-TPWM. Previously, this was done to ensure that

each modulation scheme featured a DC current utilization of 0.7215, however; due to the overlap time added during practical implementation, the measured DC current utilization for each modulation scheme showed some minor variation, as illustrated in Table 7.

Table 7: DC current utilization measured while testing the harmonic performance of the three $N_p = 7$ modulation schemes.

Modulation Scheme	Amplitude Modulation Index (m_a)	DC Current Utilization (I_{w1}/I_d)
SHE	1	0.726
TPWM	0.79	0.727
SHE-TPWM	0.85	0.726

By observing the phase-A PWM current FFTs included in Figs. 28, 29, and 30, it is clear that the proposed SHE-TPWM scheme continues to retain the superior low-order harmonic performance of conventional SHE, even when applied in practice. This is proven by the fact that their respective phase-A PWM current FFTs are identical, each featuring nearly complete elimination of the 5th, 7th, and 11th order PWM current harmonics. The reason for these harmonics not being completely eliminated is again due to the overlap added to their gating signals.

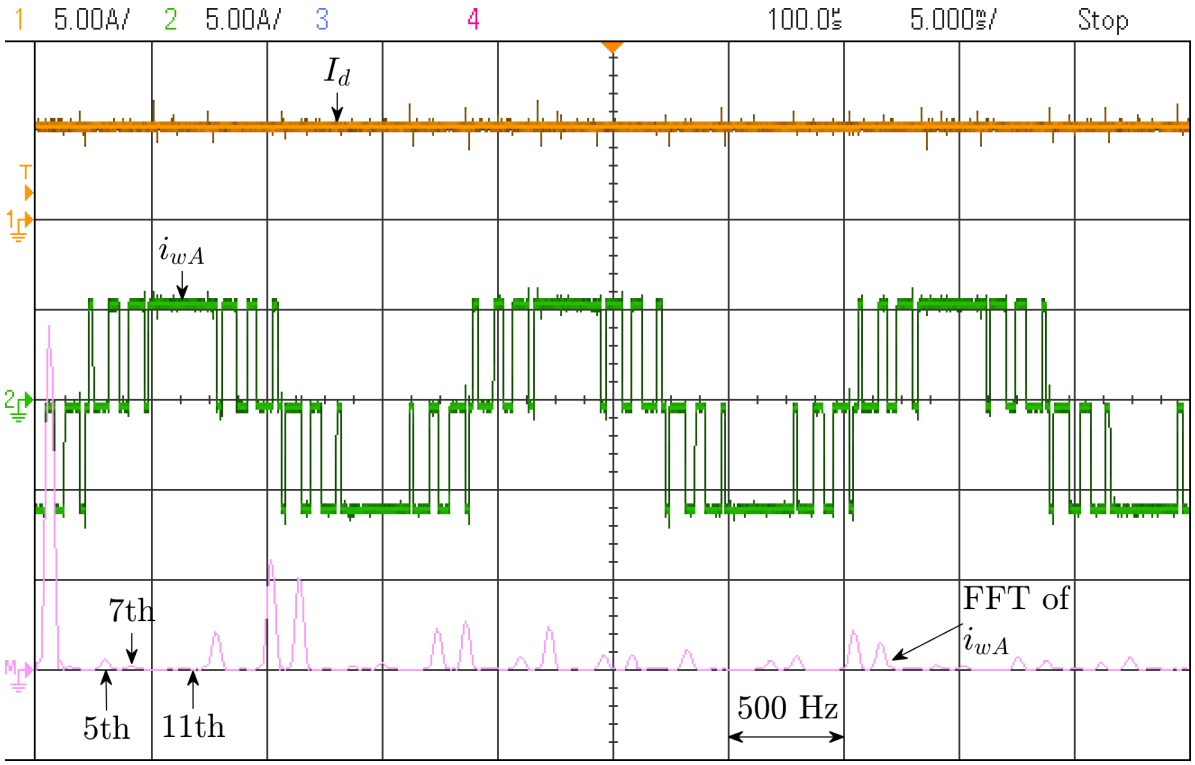

Figure 28: Experimental results showing the DC-link current (I_d) and phase-A PWM current (i_{wA}) waveforms during steady-state operation of conventional SHE ($m_a = 1$, $N_p = 7$). The FFT of the phase-A PWM current is also included.

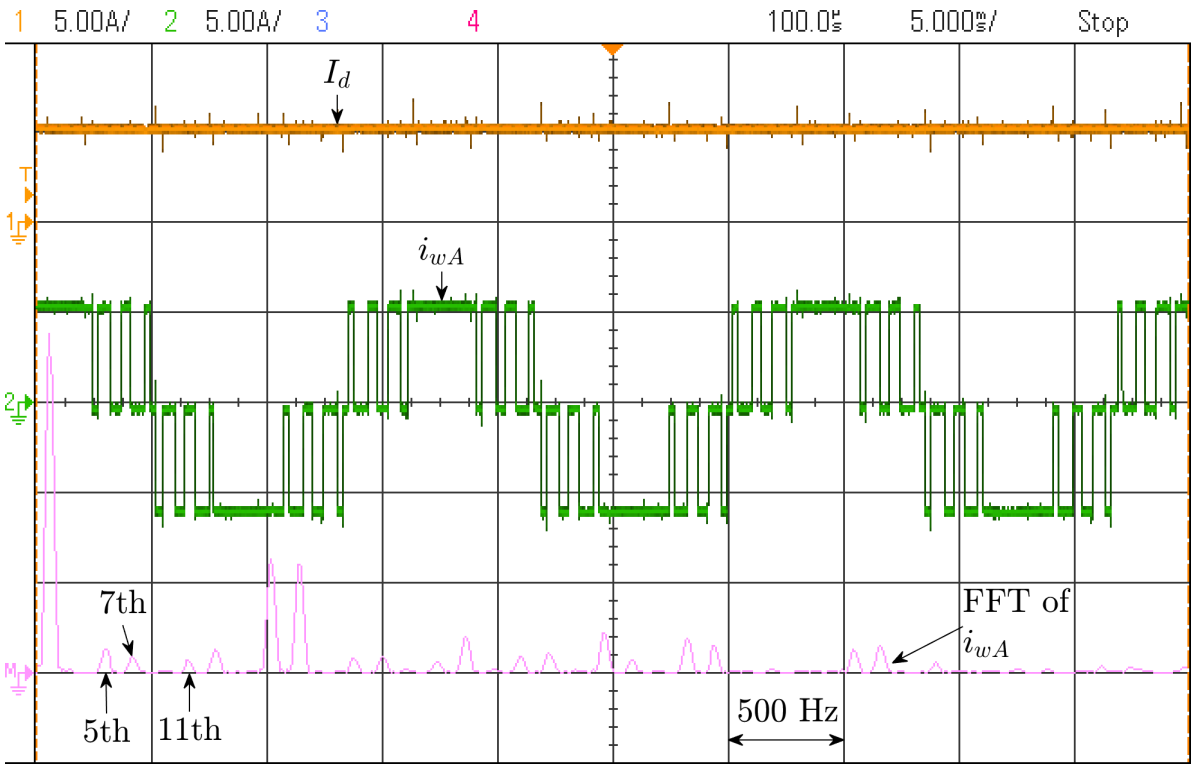

Figure 29: Experimental results showing the DC-link current (I_d) and phase-A PWM current (i_{wA}) waveforms during steady-state operation of conventional TPWM ($m_a = 0.79$, $N_p = 7$). The FFT of the phase-A PWM current is also included.

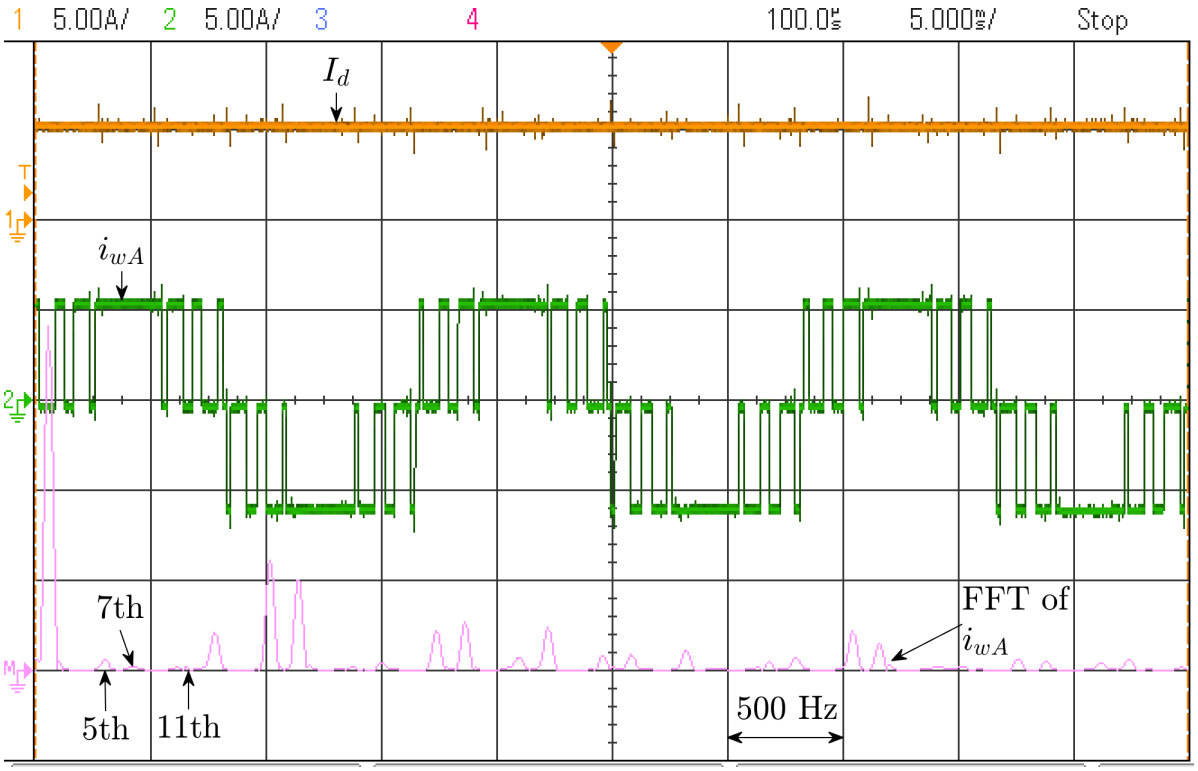

Figure 30: Experimental results showing the DC-link current (I_d) and phase-A PWM current (i_{wA}) waveforms during steady-state operation of the proposed SHE-TPWM scheme ($m_a = 0.85$, $N_p = 7$). The FFT of the phase-A PWM current is also included.

3.3.2.3 Maximum DC Current Utilization

Figs. 31, 32, and 33 show experimental results consisting of DC-link current and phase-A PWM current waveforms, along with FFTs of the phase-A PWM current, obtained using the same modulation schemes as in Section 3.3.2.2. However, because these experiments were used to determine the practical maximum DC current utilization of each modulation scheme, they were each configured with an amplitude modulation index of 1. The maximum DC current utilization values associated with each of the three modulation schemes are included in Table 8. By analyzing these numerical results, it is clearly visible that the proposed SHE-TPWM scheme features a maximum DC current utilization nearly equivalent to that of TPWM, and significantly higher than that of SHE.

Table 8: Maximum DC current utilization measured while testing the three $N_p = 7$ modulation schemes.

Modulation Scheme	Amplitude Modulation Index (m_a)	Maximum DC Current Utilization ($I_{w1,max}/I_d$)
SHE	1	0.726
TPWM	1	0.745
SHE-TPWM	1	0.743

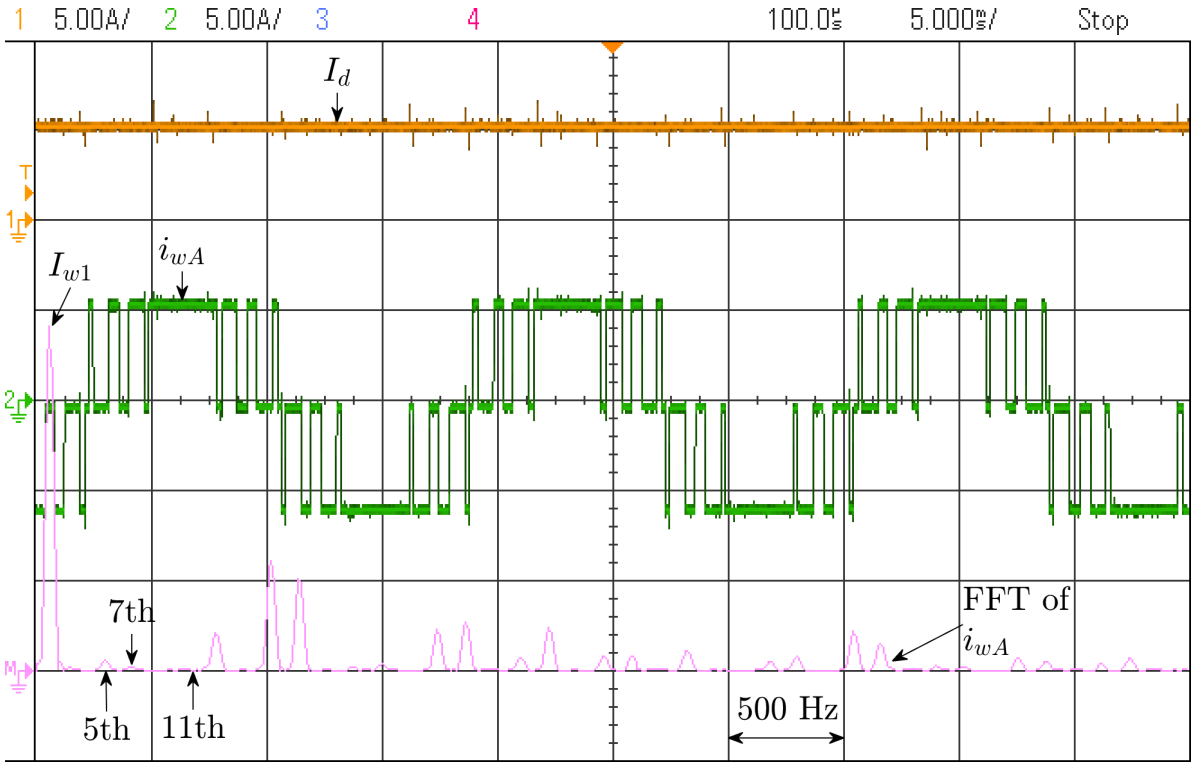

Figure 31: Experimental results showing the DC-link current (I_d) and phase-A PWM current (i_{wA}) waveforms during steady-state operation of conventional SHE ($m_a = 1$, $N_p = 7$). The FFT of the phase-A PWM current is also included.

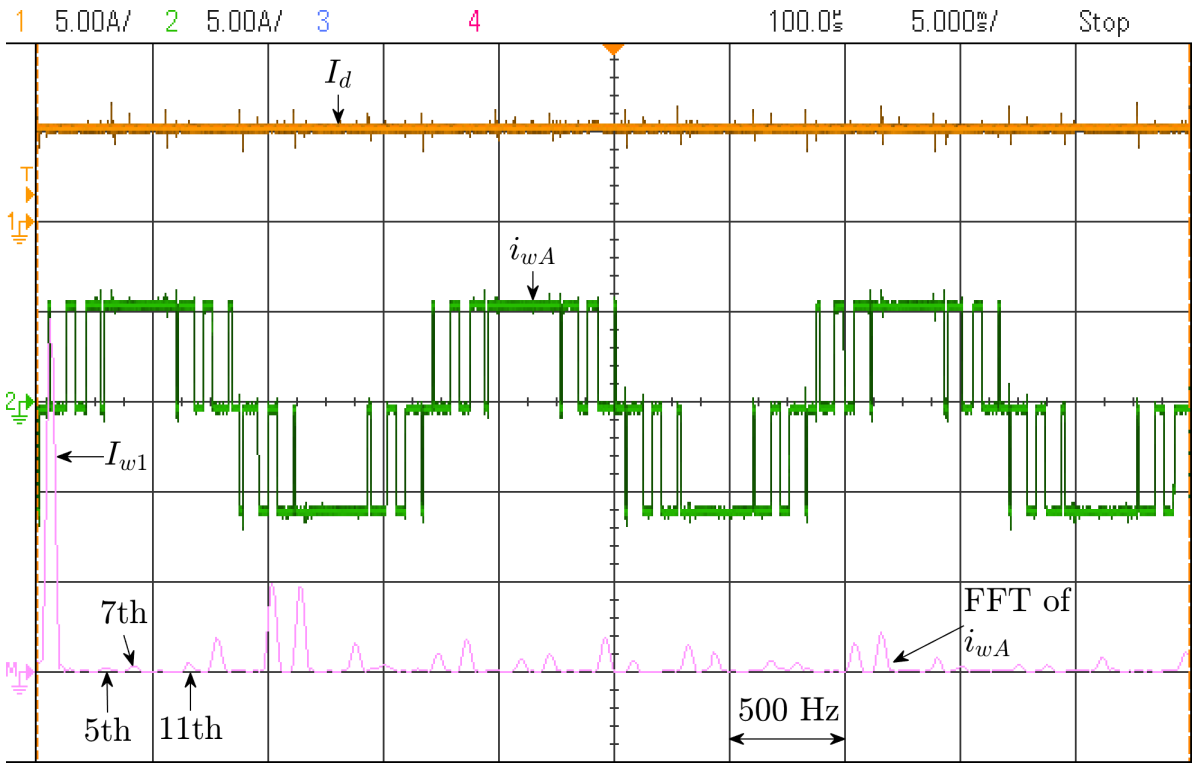

Figure 32: Experimental results showing the DC-link current (I_d) and phase-A PWM current (i_{wA}) waveforms during steady-state operation of conventional TPWM ($m_a = 1$, $N_p = 7$). The FFT of the phase-A PWM current is also included.

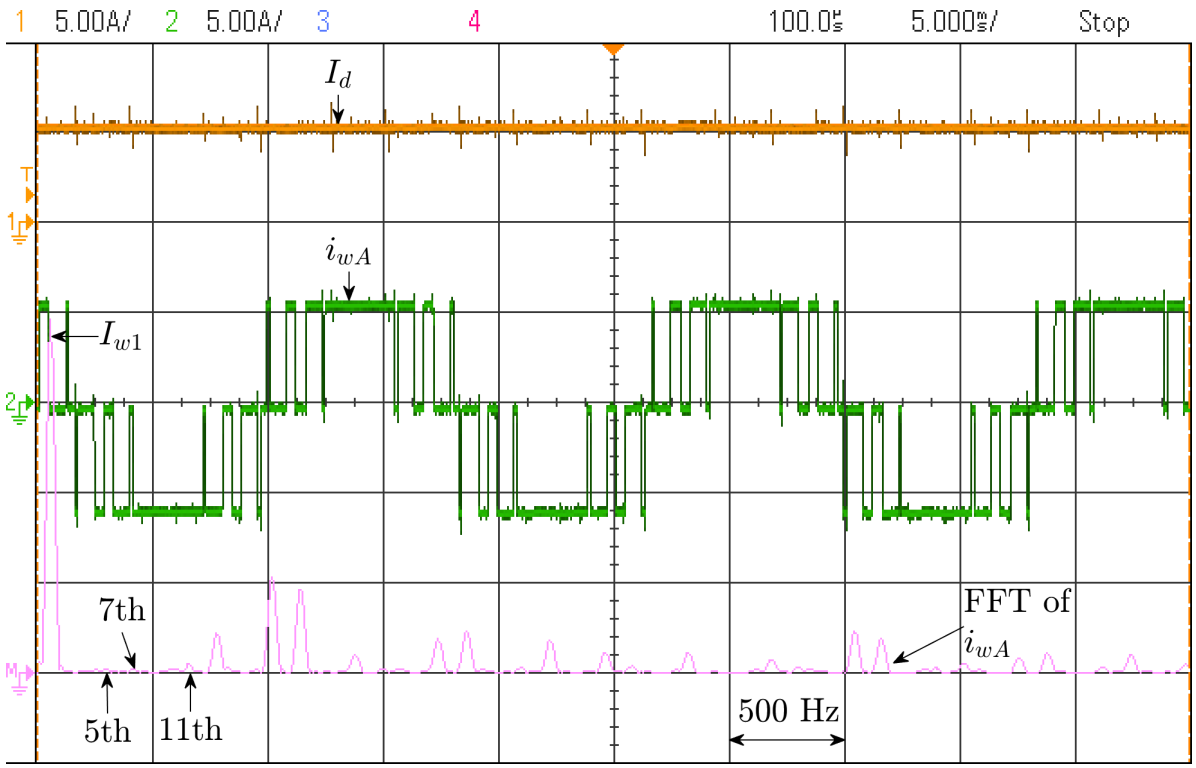

Figure 33: Experimental results showing the DC-link current (I_d) and phase-A PWM current (i_{wA}) waveforms during steady-state operation of the proposed SHE-TPWM scheme ($m_a = 1$, $N_p = 7$). The FFT of the phase-A PWM current is also included.

3.3.2.4 Dynamic Performance

Fig. 34 shows the DC-link current, phase-A PWM current, and phase-A filtered output current waveforms produced by the proposed $N_p = 7$ SHE-TPWM scheme, as its amplitude modulation index is varied from 0.4 to 1. These results highlight the ability of the proposed SHE-TPWM scheme to respond to changes in the amplitude modulation index in real-time. As observed in Fig. 34, by increasing the amplitude modulation index from 0.4 to 1, the DC-link current reduces by approximately 1A, and in response, the peak values reached by the phase-A PWM and filtered output current waveforms are reduced. The positioning of the phase-A PWM current pulses is also modified due to variation of the switching angles, however; it is difficult to view such a change at this scale.

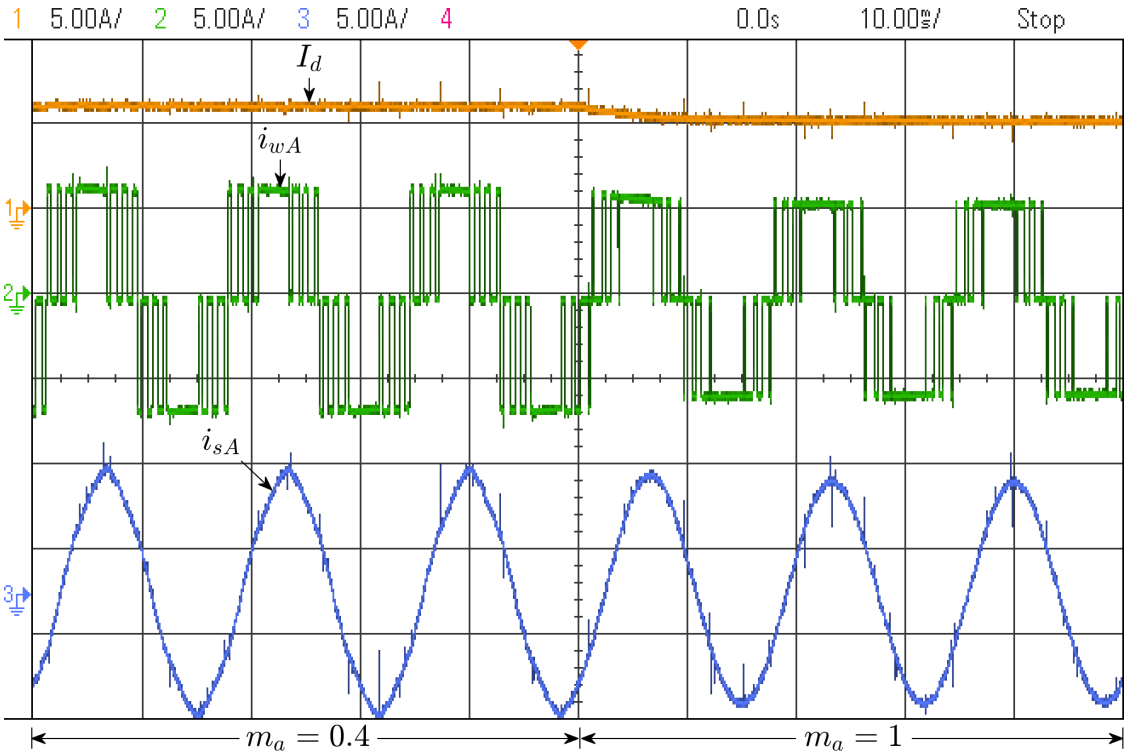

Figure 34: Experimental results showing the DC-link current (I_d), phase-A PWM current (i_{wA}), and phase-A filtered output current (i_{sA}) waveforms during transient operation, where the amplitude modulation index (m_a) of the proposed $N_p = 7$ SHE-TPWM scheme is varied from 0.4 to 1.

3.4 $N_p = 9$ SHE-TPWM

3.4.1 Theoretical Implementation & Results

Just as with the $N_p = 7$ case outlined in Section 3.3, it was determined through testing that the $N_p = 9$ SHE scheme configured to eliminate the 5th, 7th, 13th, and 17th order PWM current harmonics, was best suited for implementation into the proposed SHE-TPWM scheme. An illustration of this $N_p = 9$ SHE-TPWM scheme is included in Fig. 35. This SHE scheme uses the switching angles previously provided in (20).

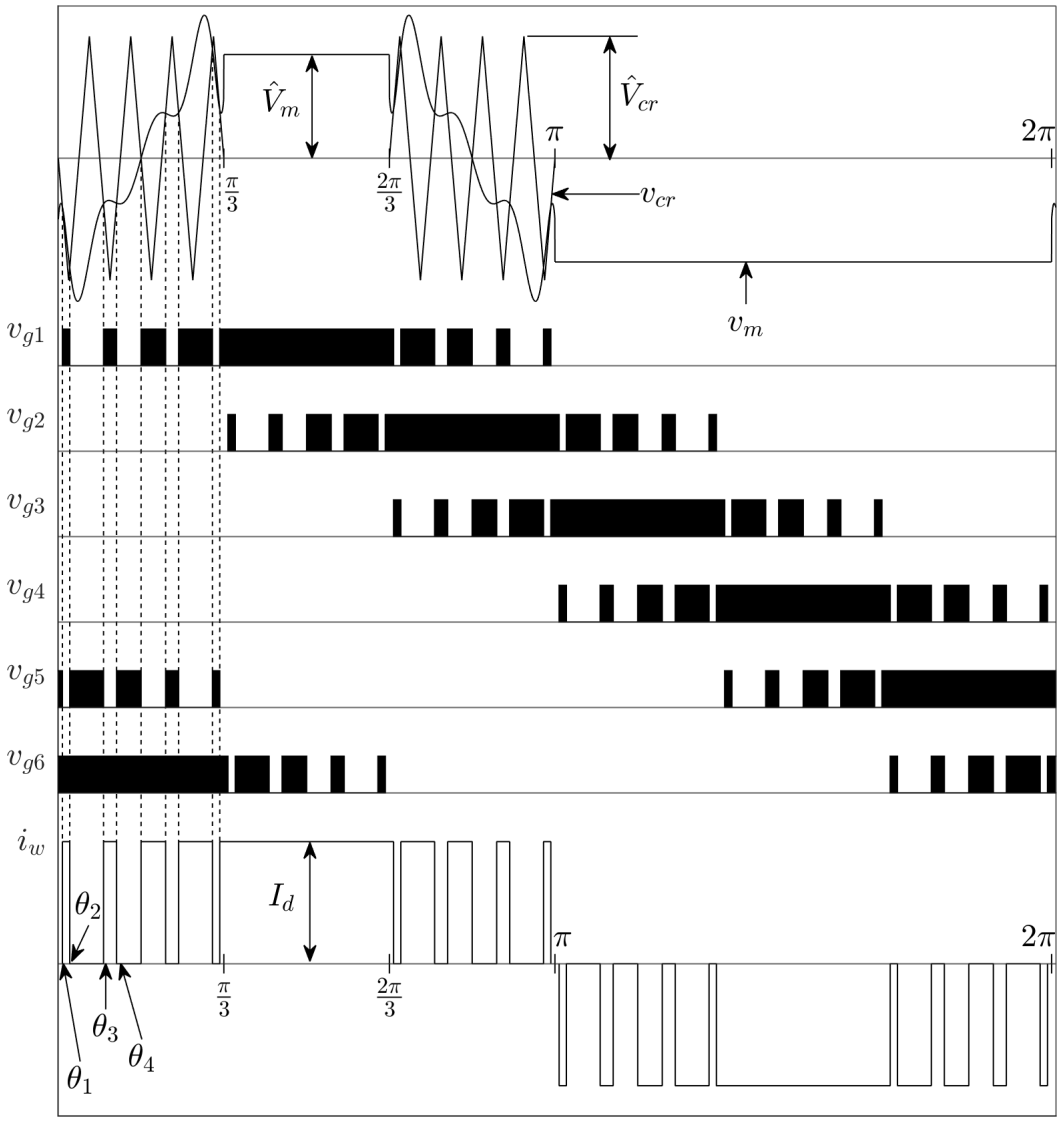

Figure 35: Principle of the proposed SHE-TPWM scheme, where the modulating signal (v_m) has been synthesized to eliminate the 5th, 7th, 13th, and 17th order CSC PWM current harmonics ($N_p = 9$, $m_a = 0.85$).

Fig. 36 displays the harmonic profiles of conventional SHE configured to eliminate the 5th, 7th, 13th, and 17th order PWM current harmonics (without amplitude modulation index control), conventional $N_p = 9$ TPWM, and the proposed SHE-TPWM scheme illustrated in Fig. 35. By comparing the harmonic profiles of the SHE and SHE-TPWM schemes included in Fig. 36, it is evident that the proposed SHE-TPWM scheme retains the superior low-order harmonic performance of conventional SHE, as they both possess identical harmonic profiles. Both schemes are shown to completely eliminate the 5th, 7th, 13th and 17th order PWM current harmonics, which are still present in the harmonic profile of $N_p = 9$ TPWM.

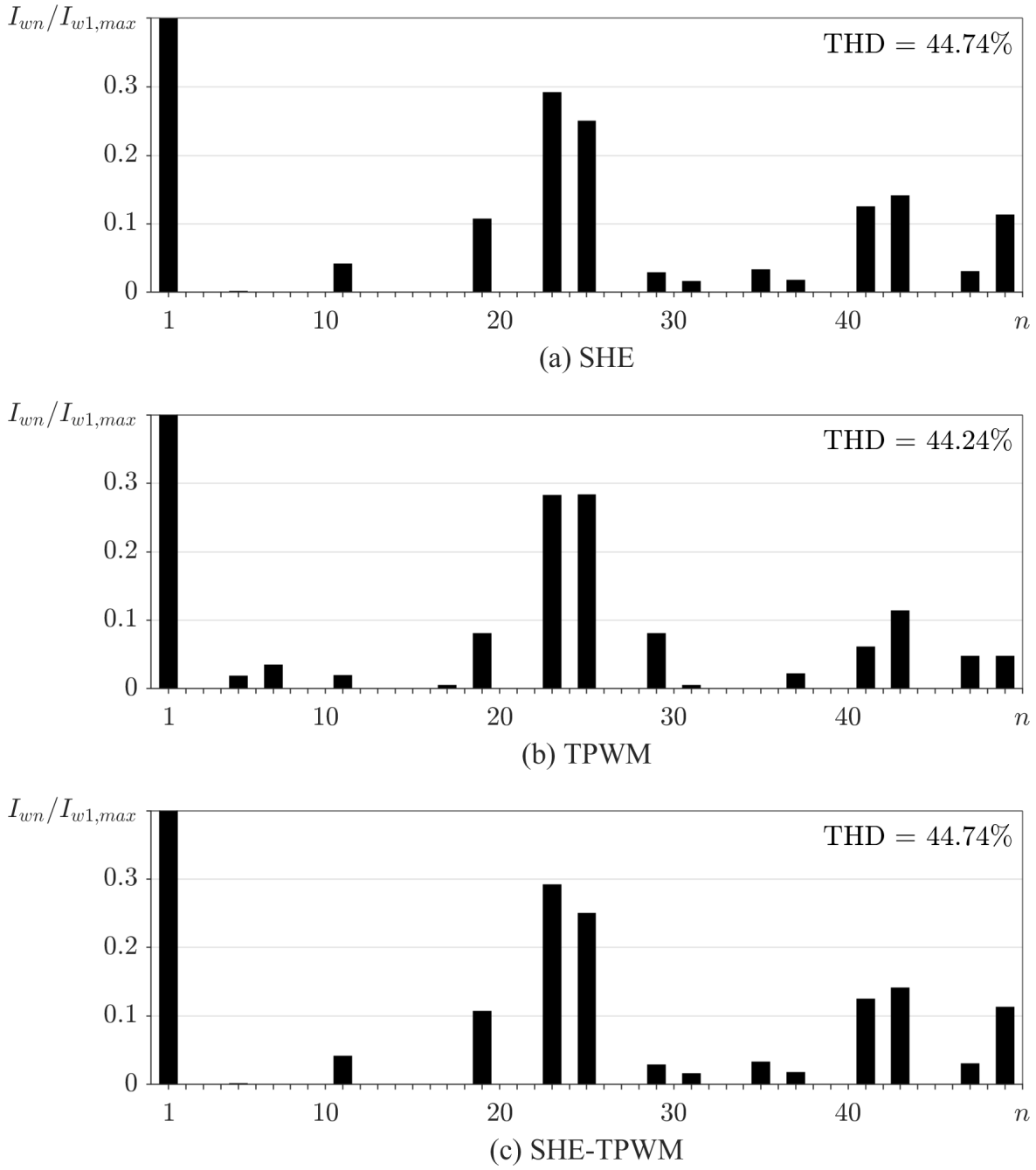

Figure 36: Harmonic profiles of (a) SHE ($m_a = 1$), (b) TPWM ($m_a = 0.774$), and (c) SHE-TPWM ($m_a = 0.85$). The DC current utilization (I_{w1}/I_d) for each modulation scheme is set to 0.7225.

As shown in Fig. 37, the DC current utilization of the proposed SHE-TPWM and conventional $N_p = 9$ TPWM schemes are very similar across their full ranges of operation, however; the latter possesses a slightly higher maximum DC current utilization. Regardless, the maximum DC current utilization of the proposed SHE-TPWM scheme is again shown to be significantly higher than that of conventional SHE. Furthermore, in comparison to conventional TPWM, the proposed SHE-TPWM scheme exhibits superior

low-order harmonic performance when considering the harmonics targeted for elimination (e.g., 5th, 7th, 13th, and 17th). The magnitudes of the 5th, 7th, 13th, and 17th order PWM current harmonics produced by the proposed SHE-TPWM scheme are generally lower than their TPWM counterparts for all values of the amplitude modulation index.

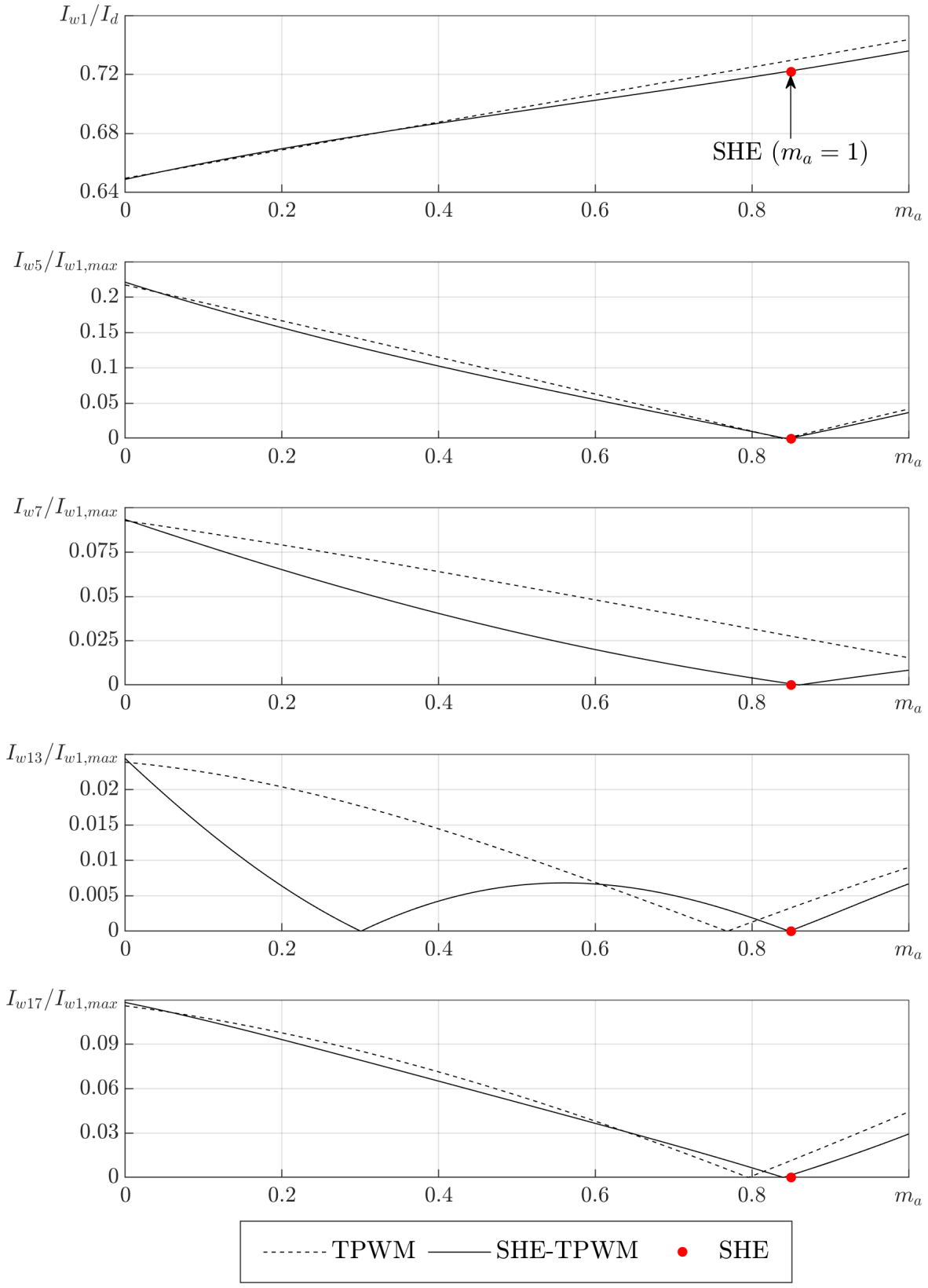

Figure 37: Comparison of the DC current utilization, as well as the low-order harmonic content of TPWM, SHE-TPWM, and SHE, across their full ranges of operation ($N_p = 9$).

3.4.2 Experimental Results

3.4.2.1 Test Setup

Refer to Section 3.3.2 for details regarding the laboratory test setup used to obtain the following experimental results. Both sets of experiments were performed using the same down-scaled PWM CSI.

3.4.2.2 Harmonic Performance

Figs. 38, 39, and 40 show experimental results consisting of DC-link current and phase-A PWM current waveforms, along with FFTs of the phase-A PWM current, obtained by applying the following modulation schemes to the test setup: SHE configured to eliminate the 5th, 7th, 13th, and 17th order PWM current harmonics (without amplitude modulation index control) (Fig. 38), $N_p = 9$ TPWM (Fig. 39), and the proposed $N_p = 9$ SHE-TPWM scheme (Fig. 40). As with the previous $N_p = 7$ case, in order to provide an objective comparison, each of the three modulation schemes showcased in these figures were configured following the amplitude modulation indices included in Table 9. Furthermore, based on the results presented in Figs. 38 - 40, specifically the phase-A PWM current FFTs included in each figure, it is clear that the proposed SHE-TPWM scheme features the same superior low-order harmonic performance as conventional SHE, for the case where $N_p = 9$.

Table 9: DC current utilization measured while testing the harmonic performance of the three $N_p = 9$ modulation schemes.

Modulation Scheme	Amplitude Modulation Index (m_a)	DC Current Utilization (I_{w1}/I_d)
SHE	1	0.712
TPWM	0.774	0.709
SHE-TPWM	0.85	0.714

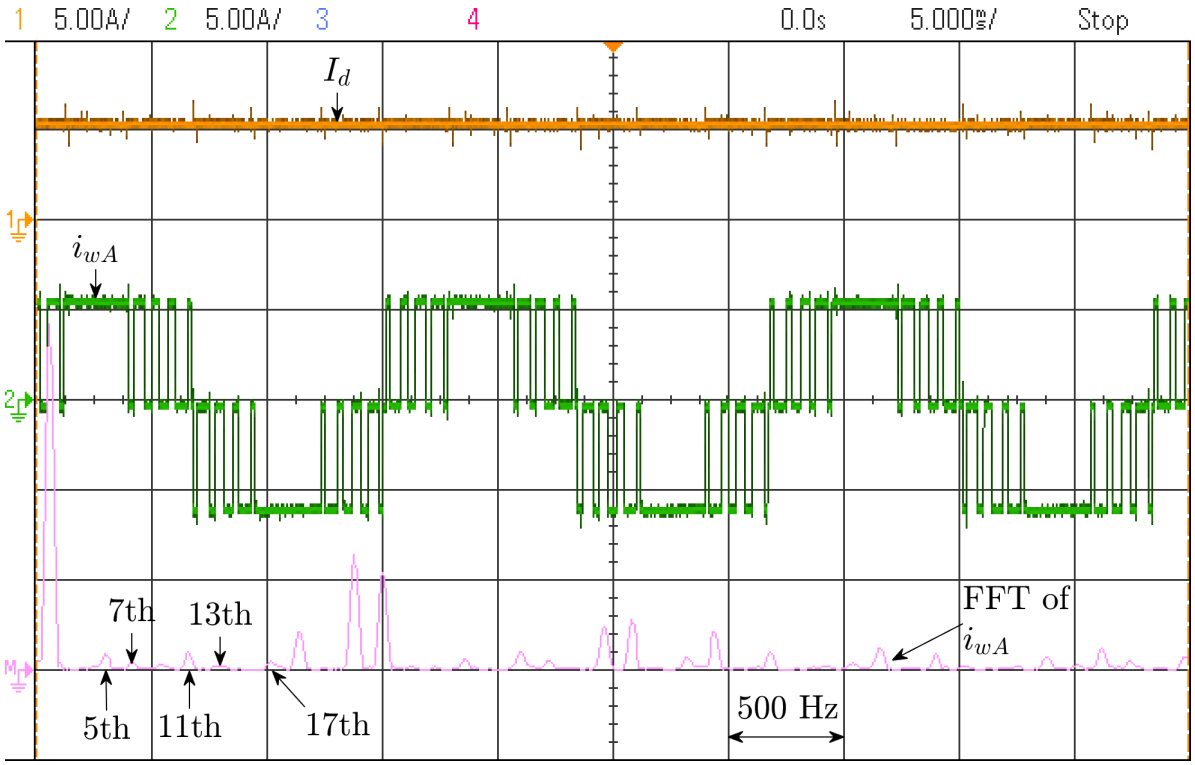

Figure 38: Experimental results showing the DC-link current (I_d) and phase-A PWM current (i_{wA}) waveforms during steady-state operation of conventional SHE ($m_a = 1$, $N_p = 9$). The FFT of the phase-A PWM current is also included.

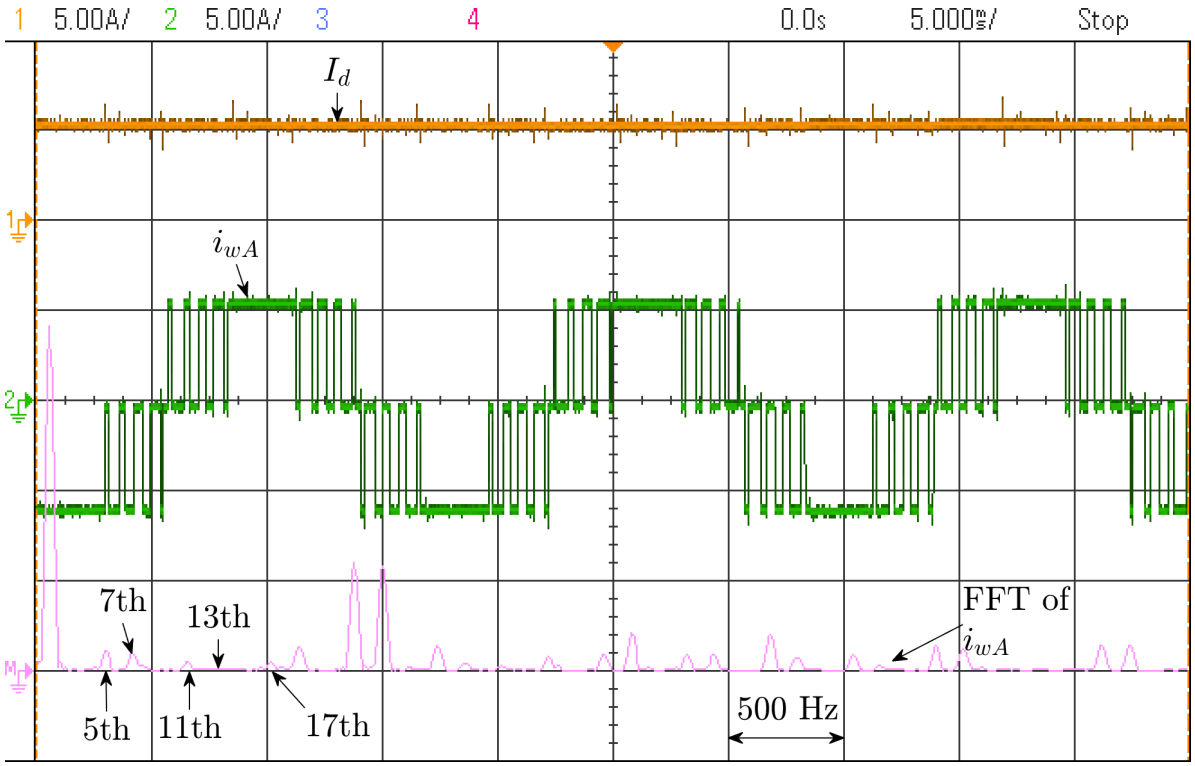

Figure 39: Experimental results showing the DC-link current (I_d) and phase-A PWM current (i_{wA}) waveforms during steady-state operation of conventional TPWM ($m_a = 0.79$, $N_p = 9$). The FFT of the phase-A PWM current is also included.

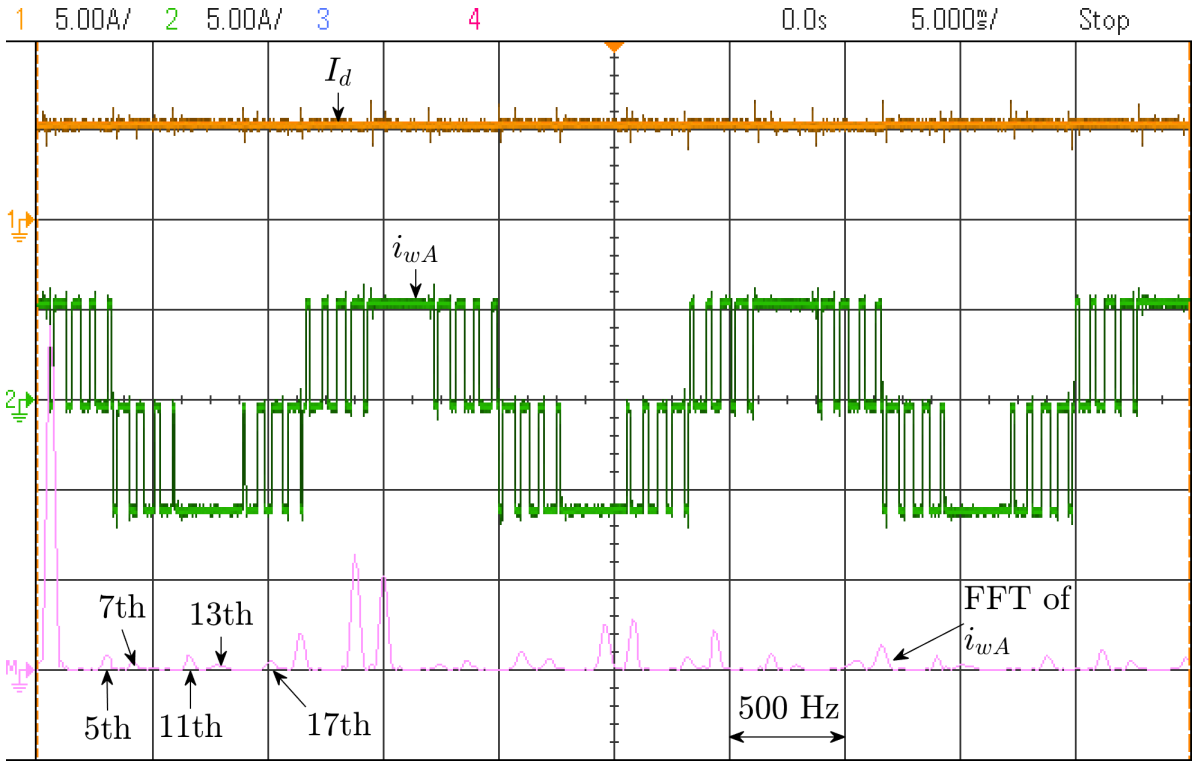

Figure 40: Experimental results showing the DC-link current (I_d) and phase-A PWM current (i_{wA}) waveforms during steady-state operation of the proposed SHE-TPWM scheme ($m_a = 0.85$, $N_p = 9$). The FFT of the phase-A PWM current is also included.

3.4.2.3 Maximum DC Current Utilization

Experimental results, including DC-link current and phase-A PWM current waveforms, as well as FFTs of the phase-A PWM current, are presented in Figs. 41, 42, and 43. The same modulation schemes used in Section 3.4.2.2 are employed to achieve these results. However, in these experiments, each of the three $N_p = 9$ modulation schemes use an amplitude modulation index of 1 in order to determine their practical maximum DC current utilization. Table 10 highlights the maximum DC current utilization associated with each of the three $N_p = 9$ modulation schemes. Examination of these results reveals that the proposed SHE-TPWM scheme demonstrates a maximum DC current utilization almost equivalent to that of TPWM, and higher than that of SHE.

Table 10: Maximum DC current utilization measured while testing the three $N_p = 9$ modulation schemes.

Modulation Scheme	Amplitude Modulation Index (m_a)	Maximum DC Current Utilization ($I_{w1,max}/I_d$)
SHE	1	0.712
TPWM	1	0.738
SHE-TPWM	1	0.725

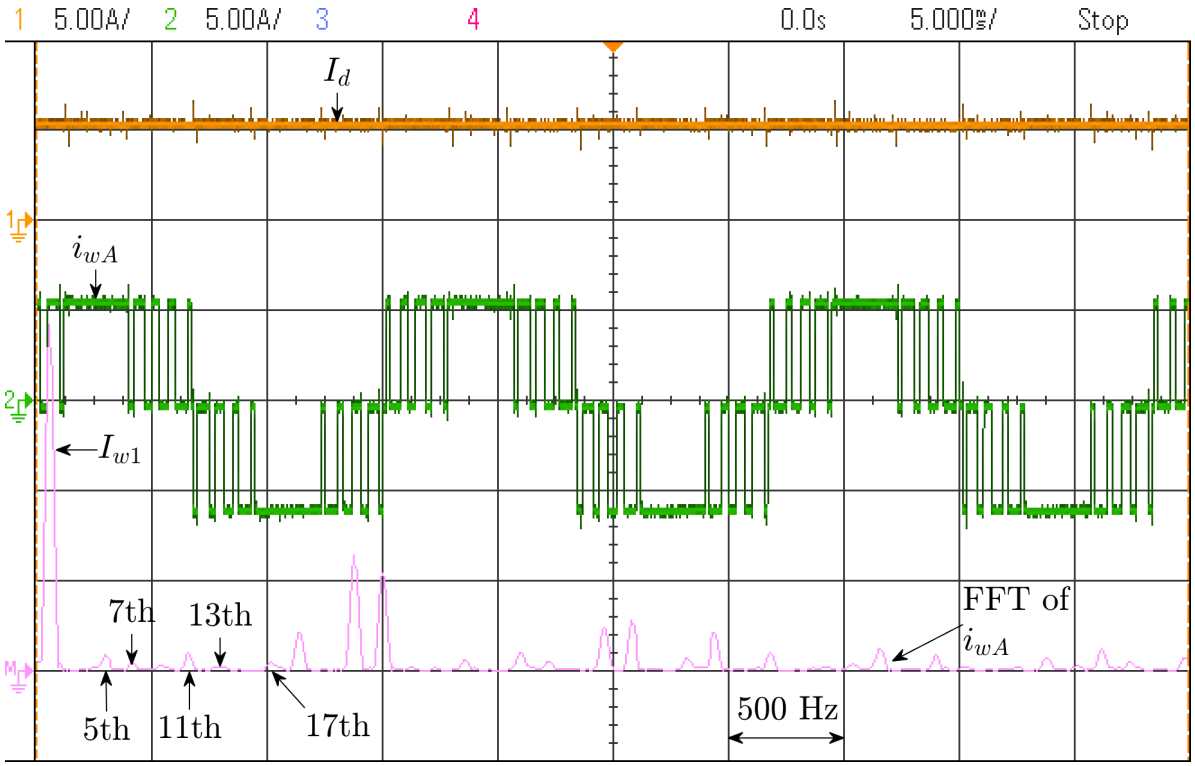

Figure 41: Experimental results showing the DC-link current (I_d) and phase-A PWM current (i_{wA}) waveforms during steady-state operation of conventional SHE ($m_a = 1$, $N_p = 9$). The FFT of the phase-A PWM current is also included.

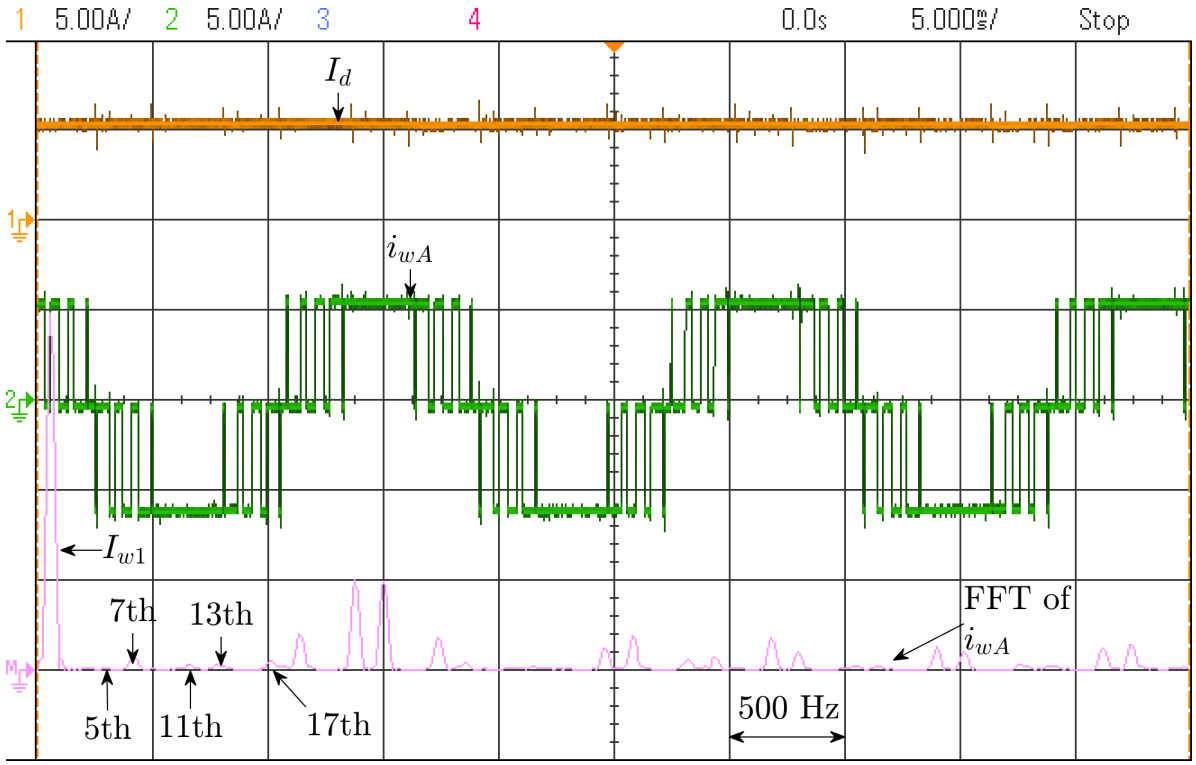

Figure 42: Experimental results showing the DC-link current (I_d) and phase-A PWM current (i_{wA}) waveforms during steady-state operation of conventional TPWM ($m_a = 1$, $N_p = 9$). The FFT of the phase-A PWM current is also included.

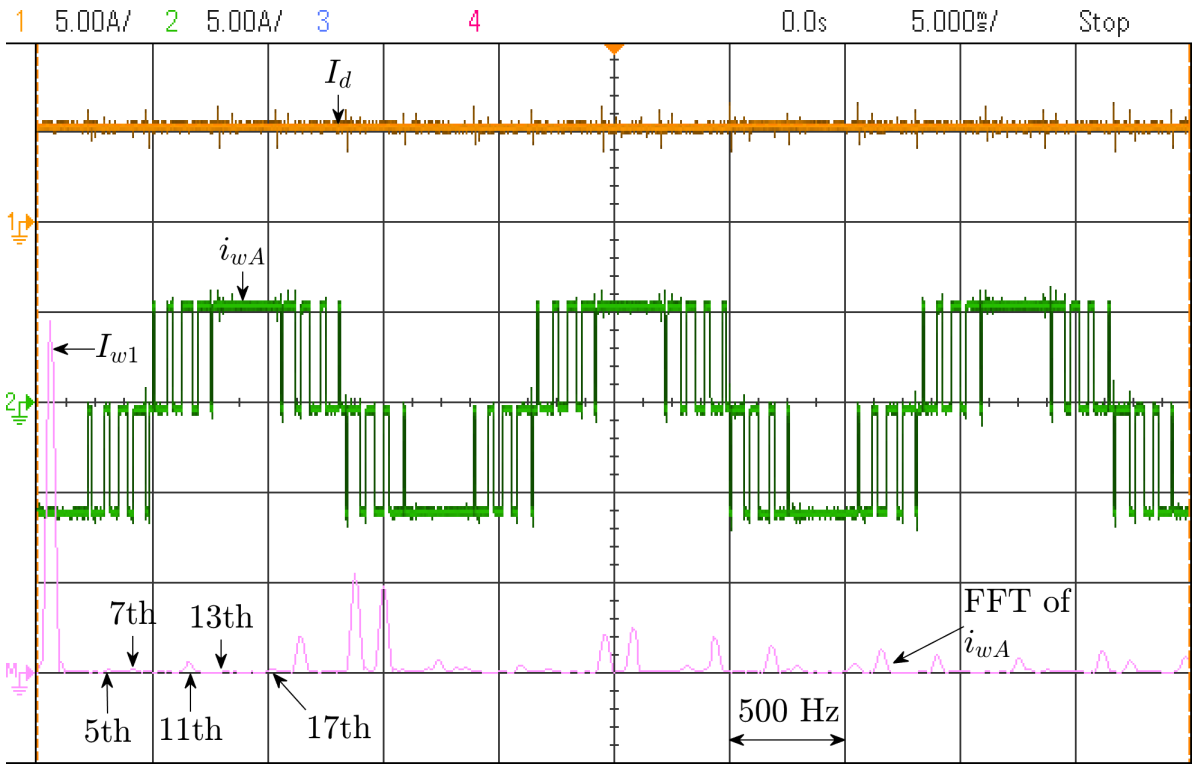

Figure 43: Experimental results showing the DC-link current (I_d) and phase-A PWM current (i_{wA}) waveforms during steady-state operation of the proposed SHE-TPWM scheme ($m_a = 1$, $N_p = 9$). The FFT of the phase-A PWM current is also included.

3.4.2.4 Dynamic Performance

Fig. 44 shows the DC-link current, phase-A PWM current, and phase-A filtered output current waveforms produced by the proposed $N_p = 9$ SHE-TPWM scheme, as its amplitude modulation index is varied from 0.4 to 1. These results confirm that the proposed SHE-TPWM scheme can be implemented within real-time, for the case where $N_p = 9$.

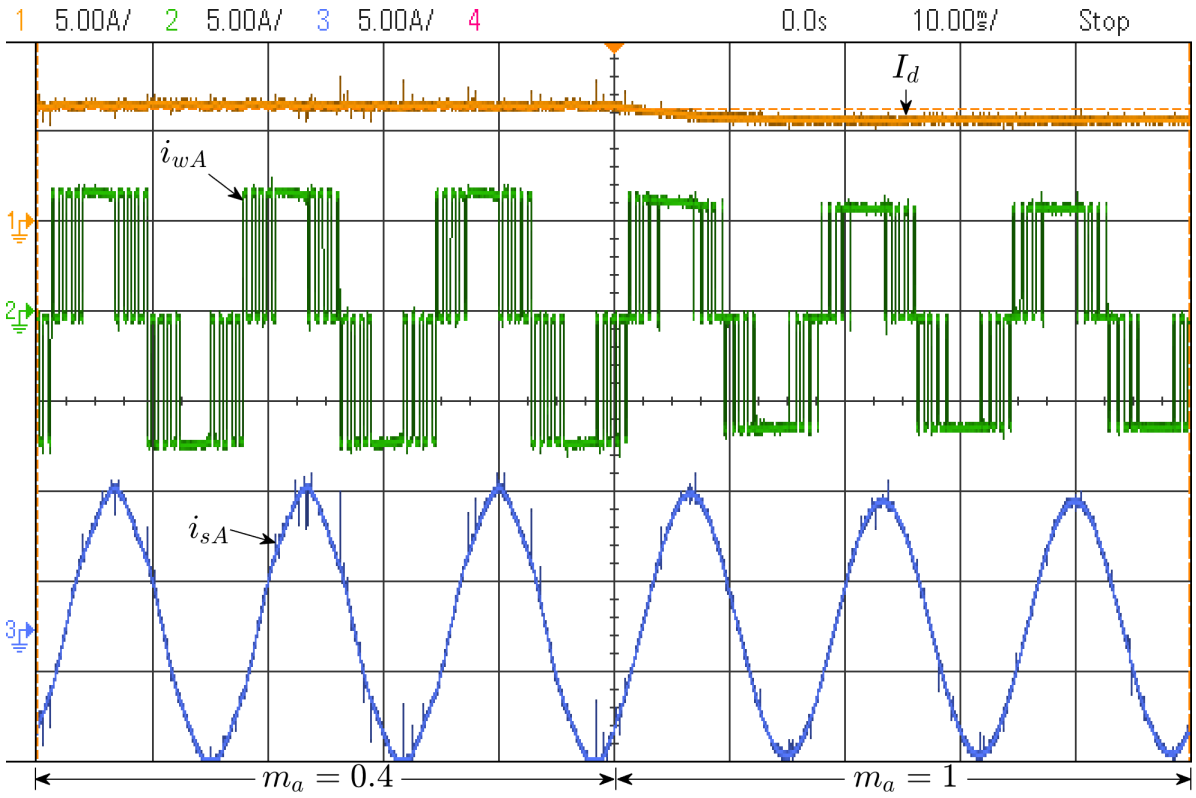

Figure 44: Experimental results showing the DC-link current (I_d), phase-A PWM current (i_{wA}), and phase-A filtered output current (i_{sA}) waveforms during transient operation, where the amplitude modulation index (m_a) of the proposed $N_p = 9$ SHE-TPWM scheme is varied from 0.4 to 1.

3.5 Summary

Based on the theoretical and experimental results presented in Sections 3.3 and 3.4 above, the proposed SHE-TPWM scheme is shown to retain the low-order harmonic performance of conventional SHE, while also providing better DC current utilization, improved dynamic performance, and real-time digital implementation. As a result, the proposed SHE-TPWM scheme is well suited for modulating the motor-side PWM CSI

in high-power, MV PWM CSC-based drives, specifically at high inverter output frequencies, where it would be used in place of conventional SHE configured without amplitude modulation index control.

Table 11 summarizes and compares the respective characteristics of SHE-TPWM, SHE, and TPWM, for the cases where $N_p = 7$ and $N_p = 9$. When compared to conventional SHE, the proposed SHE-TPWM scheme is shown to possess improved dynamic performance as a result of its real-time implementation, along with better DC current utilization, and the same superior low-order harmonic performance while operating at a fixed amplitude modulation index of 0.85. In comparison to conventional TPWM, the proposed SHE-TPWM scheme matches its dynamic performance, while also providing comparable DC current utilization and superior low-order harmonic performance across its full range of operation.

Table 11: Summary and comparison of the proposed SHE-TPWM scheme to equivalent conventional modulation schemes [5].

Characteristics	SHE-TPWM	SHE	TPWM
Maximum DC Current Utilization ($I_{w1,max}/I_d$)	0.739 ($N_p = 7$) 0.736 ($N_p = 9$)	0.721 ($N_p = 7$) 0.722 ($N_p = 9$)	0.743 ($N_p = 7$) 0.744 ($N_p = 9$)
Dynamic Performance	Medium	Low	Medium
Digital Implementation	Real-time	Look-up table	Real-time
Harmonic Performance	Best ($m_a = 0.85$) Better ($m_a \neq 0.85$)	Best	Good

4 Chapter 4 - Conclusion

4.1 Conclusion

SHE is an off-line modulation scheme that is commonly used in high-power, MV PWM CSC-based drives, as it is capable of eliminating a number of unwanted low-order PWM current harmonics, all while retaining a low device switching frequency. However,

due to its inherent off-line implementation, SHE suffers from poor dynamic performance, and in certain cases requires the use of a large look-up table for effective implementation. In order to address these issues, two new modulation schemes were proposed in this thesis, both of which were capable of retaining the superior low-order harmonic performance of conventional SHE, while simultaneously offering improved dynamic performance, along with additional benefits.

Firstly, an on-line SHE scheme was proposed for modulation of the front-end PWM CSR, that utilized curve-fitting techniques, specifically polynomial regression, to model the trajectories of independent SHE switching angles. By modeling the independent SHE switching angles as polynomial functions of the amplitude modulation index, this enabled them to be re-computed in real-time (i.e., on-line), thus allowing for more accurate and continuous amplitude modulation index control when compared to the conventional look-up table method of implementation. Through further theoretical and experimental tests, where the proposed on-line SHE scheme was applied to a down-scaled PWM CSI, it was proven to possess improved dynamic performance, along with the same superior low-order harmonic performance, when compared to conventional SHE configured with amplitude modulation index control.

Additionally, a new modulation scheme referred to as SHE-TPWM was proposed for modulation of the motor-side PWM CSI, which combined the principles, while retaining the respective advantages, of both conventional SHE and conventional TPWM. Through this integrative approach, the proposed SHE-TPWM scheme was capable of retaining the excellent low-order harmonic performance of conventional SHE, along with the high DC current utilization, and improved dynamic performance of conventional TPWM. These performance claims were verified through both theoretical analysis and experimental testing of the proposed SHE-TPWM scheme. As a result, it was shown that the proposed SHE-TPWM could easily replace conventional SHE applied at high inverter output frequencies to PWM CSIs, without any penalty.

4.2 Future Work

Possible areas for future investigation with regard to the proposed on-line SHE and

SHE-TPWM schemes include the following:

1. Investigating the impact of the proposed on-line SHE scheme when incorporated into a power factor control scheme.

2. Investigating the impact of the proposed on-line SHE scheme when incorporated into an active damping control scheme.

3. Investigating possible applications of curve-fitting techniques in improving conventional SVM.

References

[1] *PowerFlex 7000 MV Drive*, Rockwell Automation, Milwaukee, WI, USA, 2002.

[2] *Medium Voltage Drives*, SIEMENS, Munich, Germany, 2018. [Online]. Available: https://w3.siemens.com/drives/global/en/converter/mv-drives/Pages/medium-voltage-converters

[3] *Medium Voltage AC Drives*, ABB Group, Zürich, Switzerland, 2018. [Online]. Available: http://new.abb.com/drives/medium-voltageac-drives

[4] *Medium Voltage Drives*, GE, Boston, MA, USA, 2018. [Online]. Available: http://new.abb.com/drives/medium-voltageac-drives

[5] B. Wu, *High-Power Converters and AC Drives*. New York, NY, USA: Wiley, 2006.

[6] B. Wu, J. Pontt, J. Rodriguez, S. Bernet, and S. Kouro, "Current-Source Converter and Cycloconverter Topologies for Industrial Medium-Voltage Drives," *IEEE Transactions on Industrial Electronics*, vol. 55, no. 7, pp. 2786–2797, 2008.

[7] J. C. Wiseman, B. Wu, and G. S. P. Castle, "A PWM Current-Source Rectifier with Active Damping for High Power Medium Voltage Applications," in *2002 IEEE 33rd Annual IEEE Power Electronics Specialists Conference*, 2002, pp. 1930–1934 vol. 4.

[8] E. P. Wiechmann, P. Aqueveque, R. Burgos, and J. Rodriguez, "On the Efficiency of Voltage Source and Current Source Inverters for High-Power Drives," *IEEE Transactions on Industrial Electronics*, vol. 55, no. 4, pp. 1771–1782, 2008.

[9] *Symmetric IGCT*, ABB Group, Zürich, Switzerland, 2018. [Online]. Available: http://new.abb.com/semiconductors/integrated-gate-commutatedthyristors-(igct)

[10] N. Zargari, S. Rizzo, Y. Xiao, H. Iwamoto, K. Satoh, and J. Donlon, "A new current-source converter using a symmetric gate-commutated thyristor (SGCT)," *IEEE Transactions on Industry Applications*, vol. 37, no. 3, pp. 896–903, 2001.

[11] P. Espelage, J. Nowak, and L. Walker, "Symmetrical GTO current source inverter for wide speed range control of 2300 to 4160 volt, 350 to 7000 hp, induction motors," in

Conference Record of the 1988 IEEE Industry Applications Society Annual Meeting, vol. 1, 1988, pp. 302–307.

[12] Y. W. Li, B. Wu, D. Xu, and N. R. Zargari, "Space Vector Sequence Investigation and Synchronization Methods for Active Front-End Rectifiers in High-Power Current-Source Drives," *IEEE Transactions on Industrial Electronics*, vol. 55, no. 3, pp. 1022–1034, 2008.

[13] Q. Wei, L. Xing, D. Xu, B. Wu, and N. R. Zargari, "Modulation Schemes for Medium-Voltage PWM Current Source Converter-Based Drives: An Overview," *IEEE Journal of Emerging and Selected Topics in Power Electronics*, vol. 7, no. 2, pp. 1152–1161, 2019.

[14] F. Liu, B. Wu, N. R. Zargari, and M. Pande, "An Active Damping Method Using Inductor-Current Feedback Control for High-Power PWM Current-Source Rectifier," *IEEE Transactions on Power Electronics*, vol. 26, no. 9, pp. 2580–2587, 2011.

[15] Q. Wei, B. Wu, D. Xu, and N. R. Zargari, "Minimization of Filter Capacitor for Medium-Voltage Current-Source Converters Based on Natural Sampling SVM," *IEEE Transactions on Power Electronics*, vol. 33, no. 1, pp. 473–481, 2018.

[16] B. Wu, S. Rizzo, N. R. Zargari, and Y. Xiao, "An Integrated DC Link Choke for Elimination of Motor Common-Mode Voltage in Medium Voltage Drives," in *Conference Record of the 2001 IEEE Industry Applications Conference*, 2001, pp. 2022–2027 vol. 3.

[17] N. Zhu, D. Xu, B. Wu, N. R. Zargari, M. Kazerani, and F. Liu, "Common-Mode Voltage Reduction Methods for Current-Source Converters in Medium-Voltage Drives," *IEEE Transactions on Power Electronics*, vol. 28, no. 2, pp. 995–1006, 2013.

[18] M. H. Rashid, *Power Electronics Handbook*. Oxford, UK: Elsevier Butterworth-Heinemann, 2011.

[19] Q. Wei, B. Wu, D. Xu, and N. R. Zargari, "A Natural-Sampling-Based SVM Scheme for Current Source Converter With Superior Low-Order Harmonics Performance," *IEEE Transactions on Power Electronics*, vol. 31, no. 9, pp. 6144–6154, 2016.

[20] J. Dai, Y. Lang, B. Wu, D. Xu, and N. R. Zargari, "A Multisampling SVM Scheme for Current Source Converters With Superior Harmonic Performance," *IEEE Transactions on Power Electronics*, vol. 24, no. 11, pp. 2436–2445, 2009.

[21] Q. Wei, B. Wu, D. D. Xu, and N. R. Zargari, "Optimal Space Vector Sequence Investigation Based on Natural Sampling SVM for Medium-Voltage Current-Source Converter," *IEEE Transactions on Power Electronics*, vol. 32, no. 1, pp. 176–185, 2017.

[22] H. Karshenas, H. Kojori, and S. Dewan, "Generalized techniques of selective harmonic elimination and current control in current source inverters/converters," *IEEE Transactions on Power Electronics*, vol. 10, no. 5, pp. 566–573, 1995.

[23] C. Namuduri and P. C. Sen, "Optimal Pulsewidth Modulation for Current Source Inverters," *IEEE Transactions on Industry Applications*, vol. IA-22, no. 6, pp. 1052–1072, 1986.

[24] H. Zhou, Y. W. Li, N. R. Zargari, Z. Cheng, R. Ni, and Y. Zhang, "Selective Harmonic Compensation (SHC) PWM for Grid-Interfacing High-Power Converters," *IEEE Transactions on Power Electronics*, vol. 29, no. 3, pp. 1118–1127, 2014.

[25] Y. Zhang, Y. W. Li, N. R. Zargari, and Z. Cheng, "Improved Selective Harmonics Elimination Scheme With Online Harmonic Compensation for High-Power PWM Converters," *IEEE Transactions on Power Electronics*, vol. 30, no. 7, pp. 3508–3517, 2015.

[26] Y. Zhang and Y. W. Li, "Grid Harmonics Compensation Using High-Power PWM Converters Based on Combination Approach," *IEEE Journal of Emerging and Selected Topics in Power Electronics*, vol. 4, no. 1, pp. 186–197, 2016.

[27] J. He, C. Zhang, M. Lei, J. Han, P. Guo, and Y. Li, "An Active Bypass Pulse Injection-Based Low Switching Frequency PWM Approach for Harmonic Compensation of Current-Source Converters," *IEEE Transactions on Power Electronics*, vol. 36, no. 2, pp. 1614–1625, 2021.

[28] R. Ni, Y. W. Li, Y. Zhang, N. R. Zargari, and Z. Cheng, "Virtual Impedance-Based Selective Harmonic Compensation (VI-SHC) PWM for Current Source Rectifiers," *IEEE Transactions on Power Electronics*, vol. 29, no. 7, pp. 3346–3356, 2014.

[29] Y. Zhang and Y. W. Li, "Investigation and Suppression of Harmonics Interaction in High-Power PWM Current-Source Motor Drives," *IEEE Transactions on Power Electronics*, vol. 30, no. 2, pp. 668–679, 2015.

[30] H. Gao, B. Wu, D. Xu, R. P. Aguilera, and P. Acuna, "Model Predictive Switching Pattern Control for Current-Source Converters With Space-Vector-Based Selective Harmonic Elimination," *IEEE Transactions on Power Electronics*, vol. 32, no. 8, pp. 6558–6569, 2017.

[31] K. Yang, M. Feng, Y. Wang, X. Lan, J. Wang, D. Zhu, and W. Yu, "Real-Time Switching Angle Computation for Selective Harmonic Control," *IEEE Transactions on Power Electronics*, vol. 34, no. 8, pp. 8201–8212, 2019.

[32] M. Wu, L. Ding, C. Xue, and Y. W. Li, "Model-Based Closed-Loop Control for High-Power Current Source Rectifiers Under Selective Harmonic Elimination/Compensation PWM With Fast Dynamics," *IEEE Journal of Emerging and Selected Topics in Power Electronics*, vol. 10, no. 5, pp. 5921–5932, 2022.

[33] M. Steczek, P. Chudzik, and A. Szelag, "Combination of SHE- and SHM-PWM Techniques for VSI DC-Link Current Harmonics Control in Railway Applications," *IEEE Transactions on Industrial Electronics*, vol. 64, no. 10, pp. 7666–7678, 2017.

[34] S. C. Chapra, *Applied Numerical Methods with MATLAB for Engineers and Scientists*, 4th ed. New York, NY, USA: McGraw-Hill Education, 2018.

[35] A. Janabi, B. Wang, and D. Czarkowski, "Generalized Chudnovsky Algorithm for Real-Time PWM Selective Harmonic Elimination/Modulation: Two-Level VSI Example," *IEEE Transactions on Power Electronics*, vol. 35, no. 5, pp. 5437–5446, 2020.

[36] V. B. Tymchyshyn and A. Khlevniuk, *Workbook on Mapping Simplexes Affinely*, Kyiv, Ukraine, 2019.

A On-Line SHE - Additional Experimental Results

Additional experimental results gathered while testing the practical performance of the proposed on-line SHE scheme are included below:

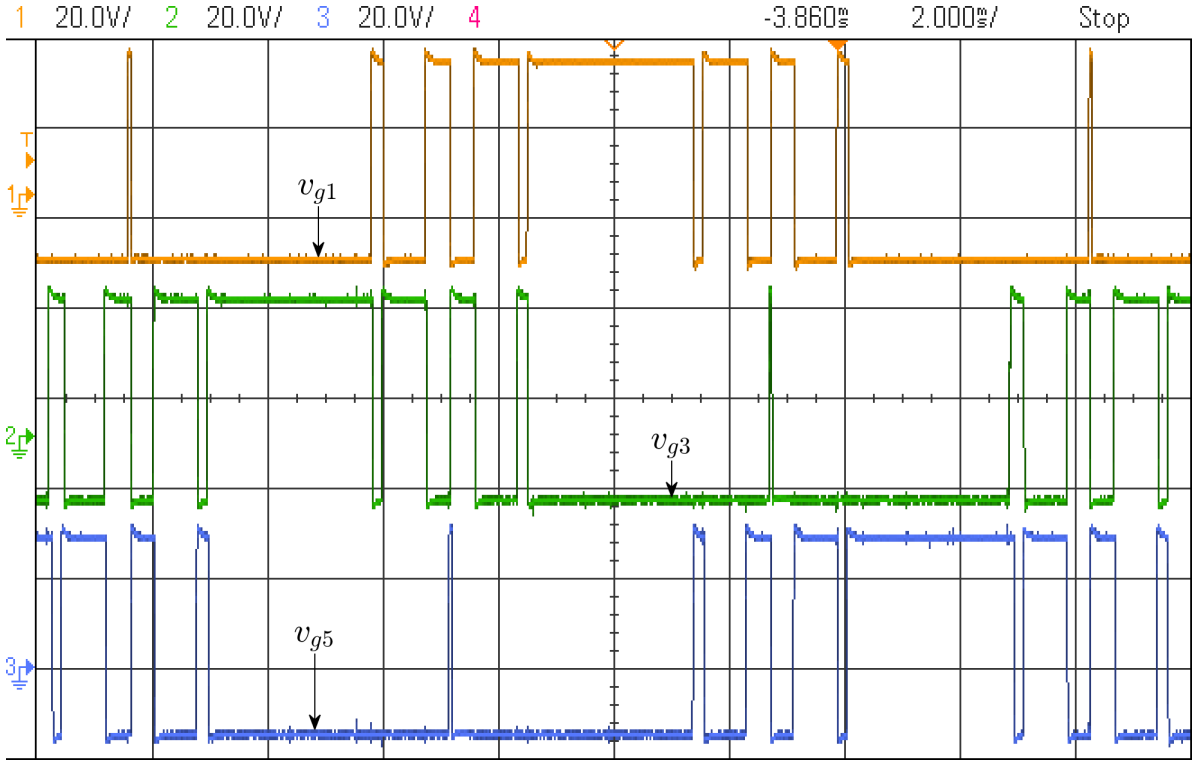

Figure A1: Experimental results showing the S_1, S_3, and S_5 gating signal ($v_{g1,\,g3,\,g5}$) waveforms during steady-state operation of the proposed on-line SHE scheme ($m_a = 1$, $N_p = 8$).

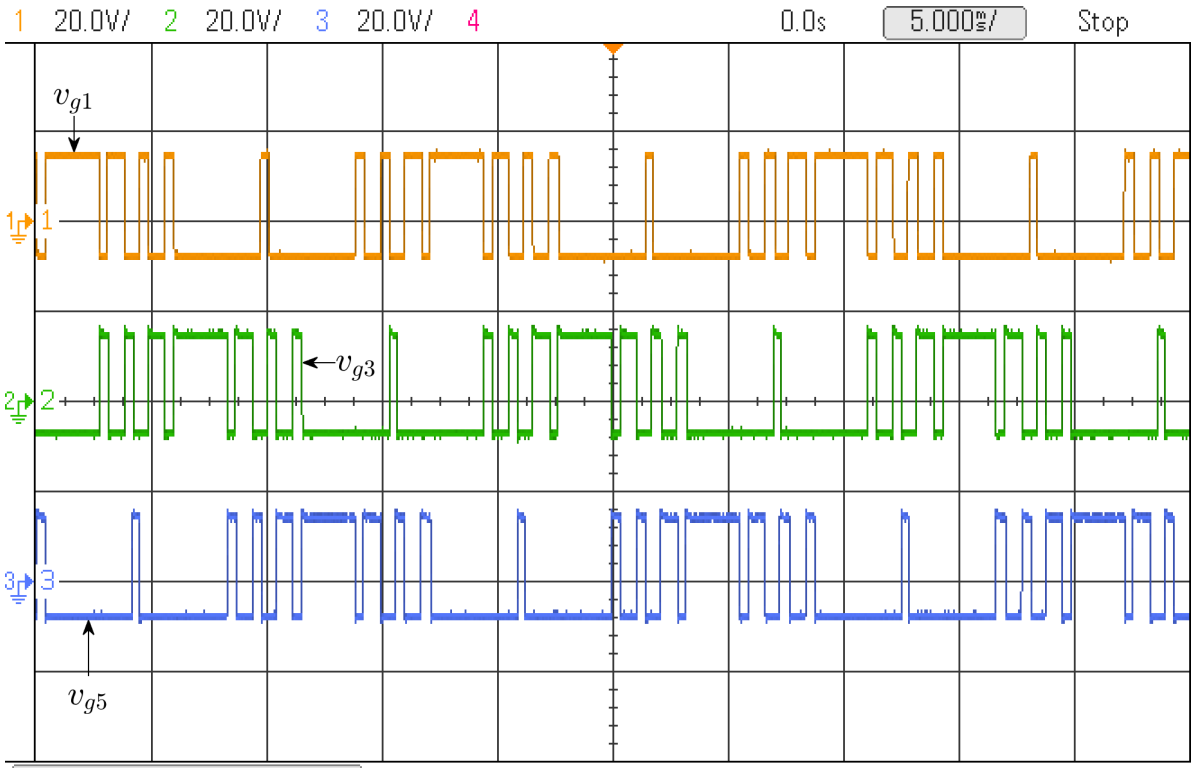

Figure A2: Experimental results showing the S_1, S_3, and S_5 gating signal ($v_{g1,\,g3,\,g5}$) waveforms during steady-state operation of the proposed on-line SHE scheme ($m_a = 0.8$, $N_p = 8$).

B SHE-TPWM - Additional Experimental Results

Additional experimental results gathered while testing the practical performance of the proposed SHE-TPWM scheme are included below:

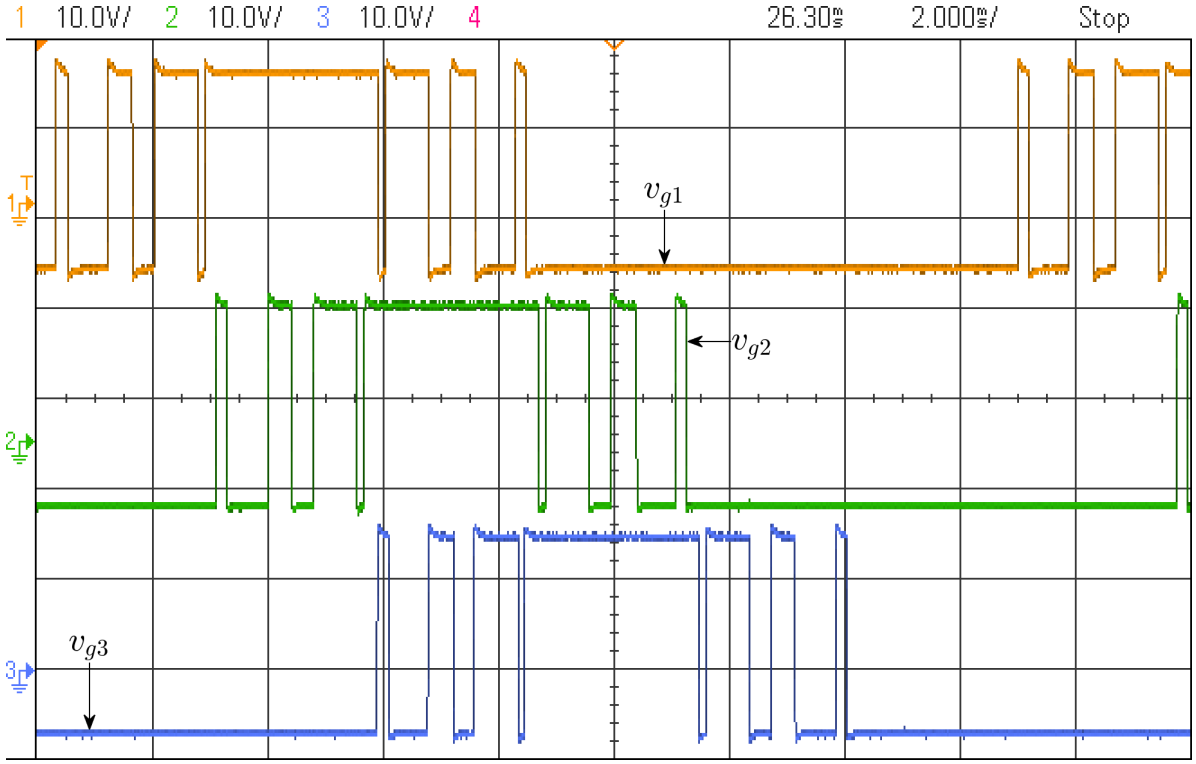

Figure B1: Experimental results showing the S_1, S_2, and S_3 gating signal (v_{g1-g3}) waveforms during steady-state operation of the proposed SHE-TPWM scheme ($m_a = 0.85$, $N_p = 7$).

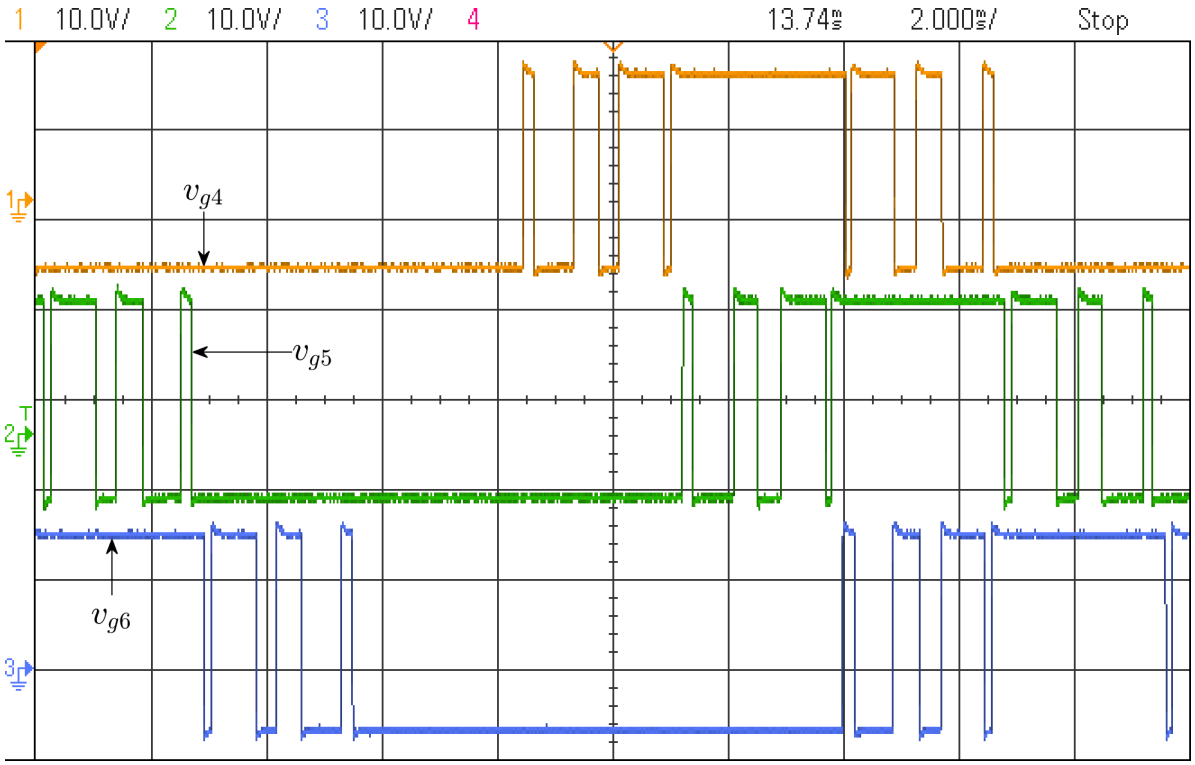

Figure B2: Experimental results showing the S_4, S_5, and S_6 gating signal (v_{g4-g6}) waveforms during steady-state operation of the proposed SHE-TPWM scheme ($m_a = 0.85$, $N_p = 7$).

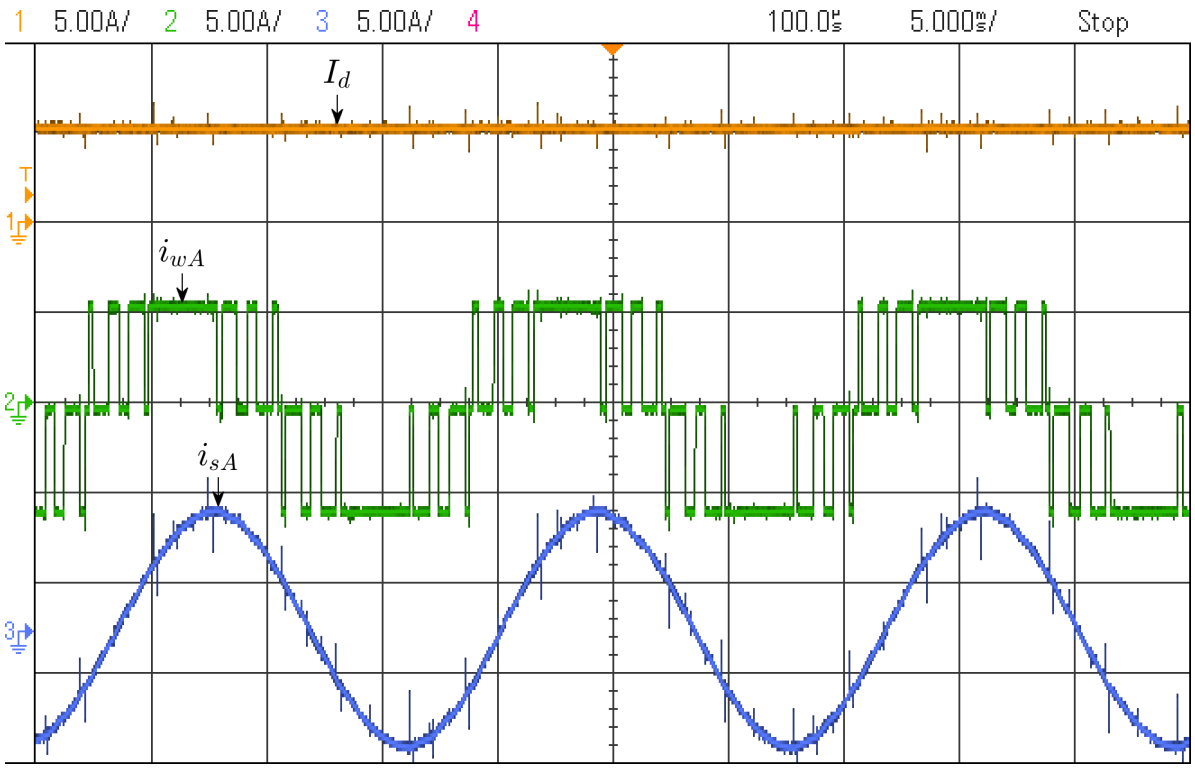

Figure B3: Experimental results showing the DC-link current (I_d), phase-A PWM current (i_{wA}), and phase-A filtered output current (i_{sA}) waveforms during steady-state operation of conventional SHE ($m_a = 1$, $N_p = 7$).

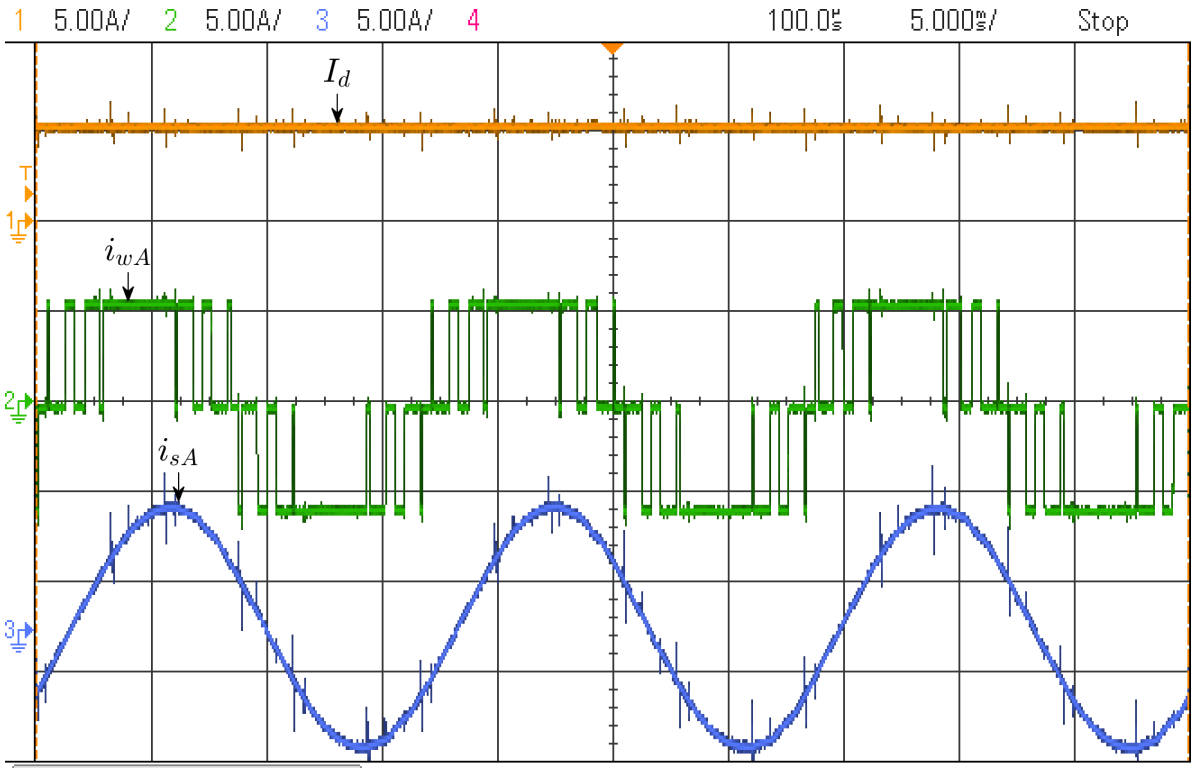

Figure B4: Experimental results showing the DC-link current (I_d), phase-A PWM current (i_{wA}), and phase-A filtered output current (i_{sA}) waveforms during steady-state operation of conventional TPWM ($m_a = 1$, $N_p = 7$).

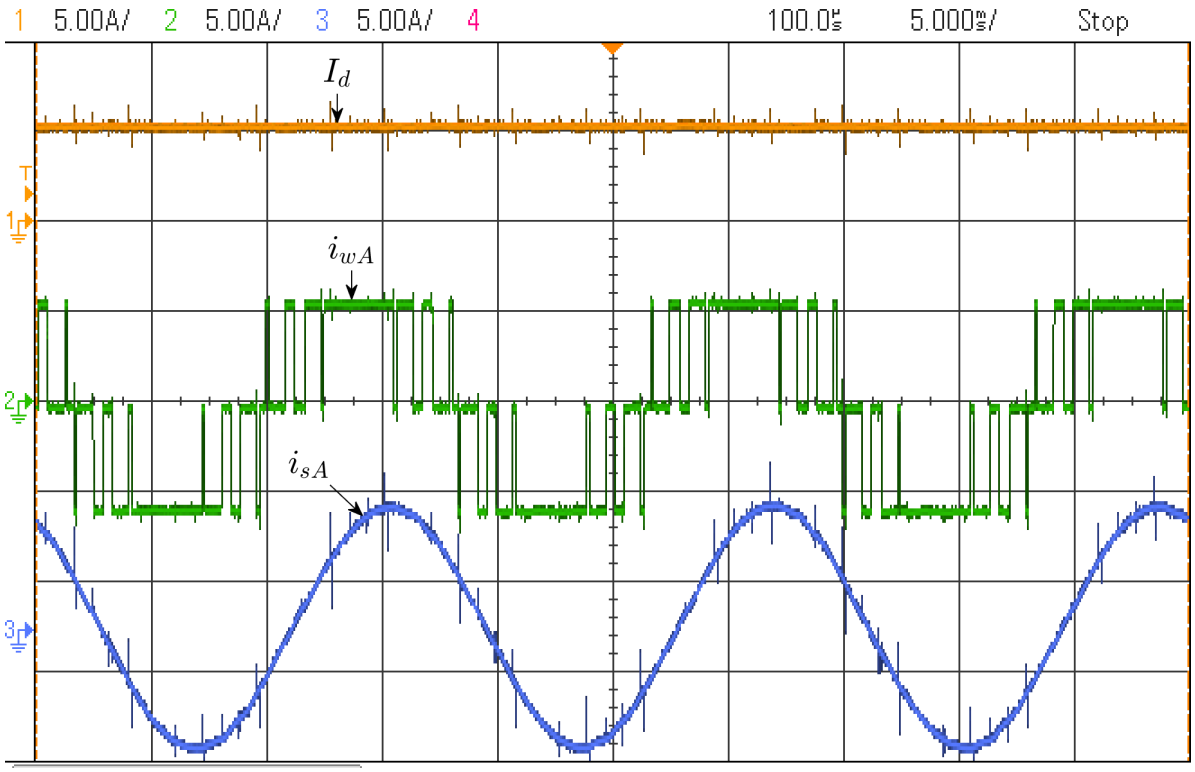

Figure B5: Experimental results showing the DC-link current (I_d), phase-A PWM current (i_{wA}), and phase-A filtered output current (i_{sA}) waveforms during steady-state operation of the proposed SHE-TPWM scheme ($m_a = 1$, $N_p = 7$).

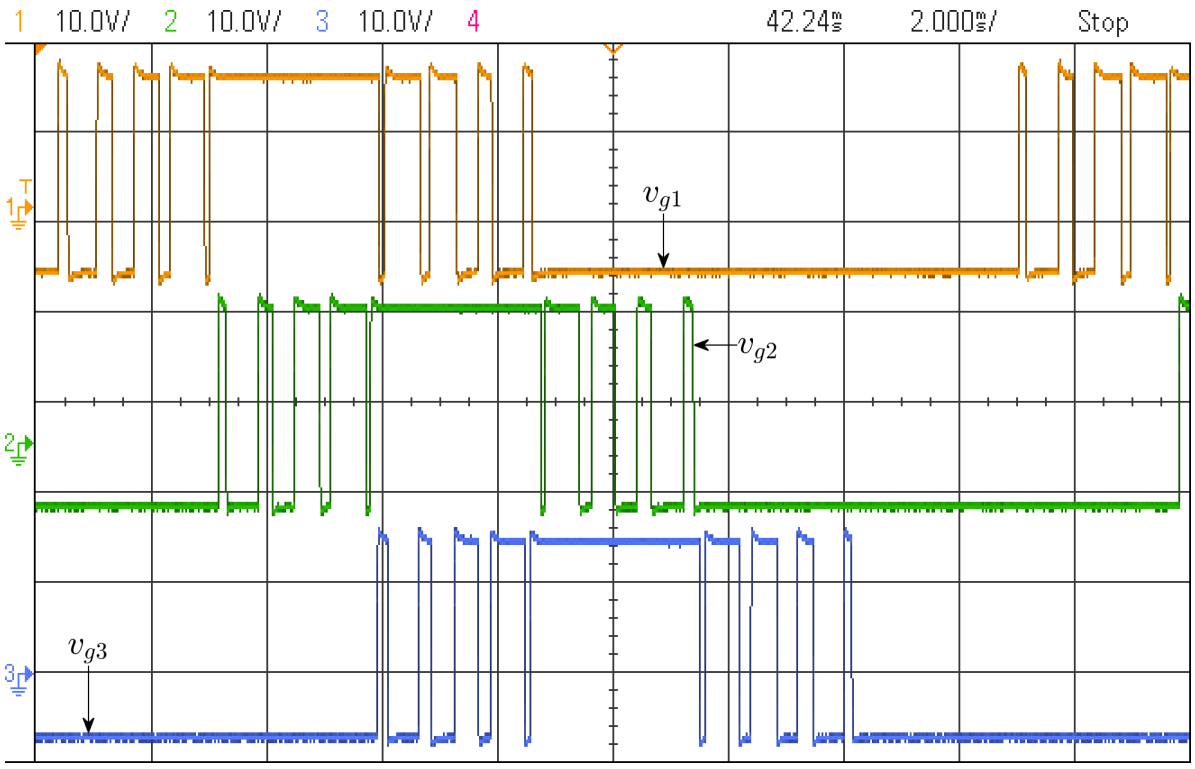

Figure B6: Experimental results showing the S_1, S_2, and S_3 gating signal (v_{g1-g3}) waveforms during steady-state operation of the proposed SHE-TPWM scheme ($m_a = 0.85$, $N_p = 9$).

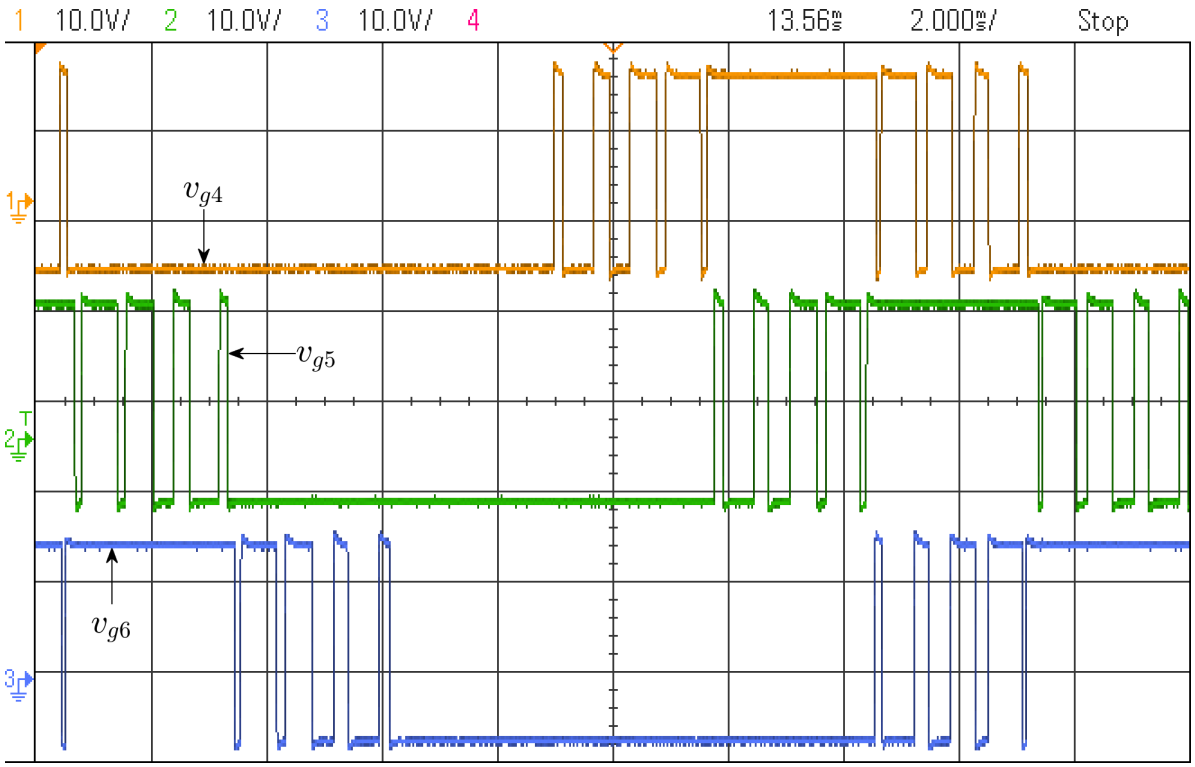

Figure B7: Experimental results showing the S_4, S_5, and S_6 gating signal (v_{g4-g6}) waveforms during steady-state operation of the proposed SHE-TPWM scheme ($m_a = 0.85$, $N_p = 9$).

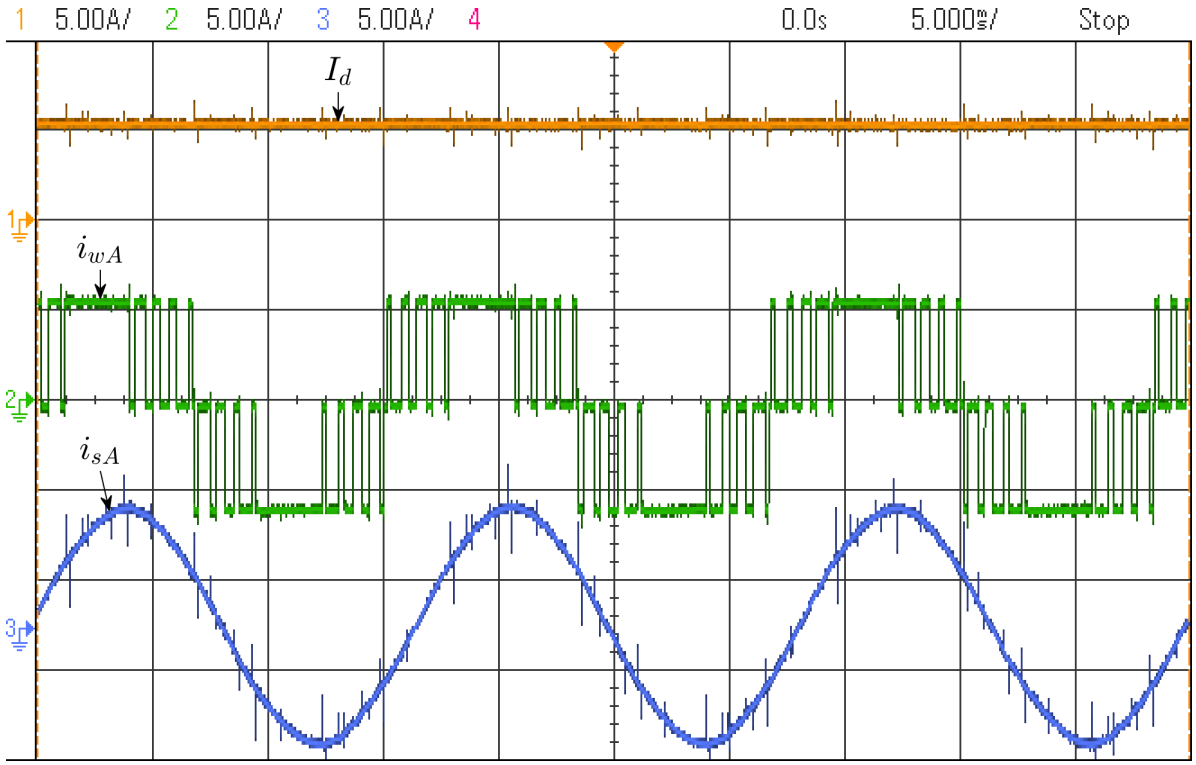

Figure B8: Experimental results showing the DC-link current (I_d), phase-A PWM current (i_{wA}), and phase-A filtered output current (i_{sA}) waveforms during steady-state operation of conventional SHE ($m_a = 1$, $N_p = 9$).

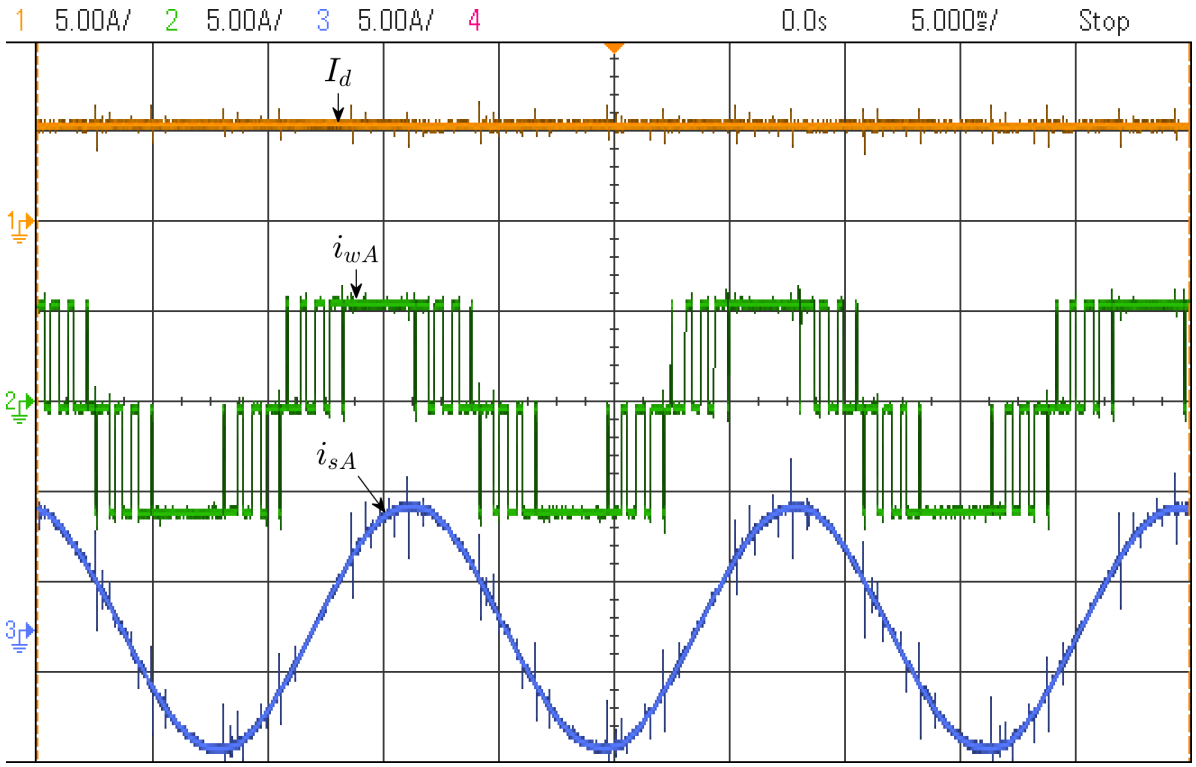

Figure B9: Experimental results showing the DC-link current (I_d), phase-A PWM current (i_{wA}), and phase-A filtered output current (i_{sA}) waveforms during steady-state operation of conventional TPWM ($m_a = 1$, $N_p = 9$).

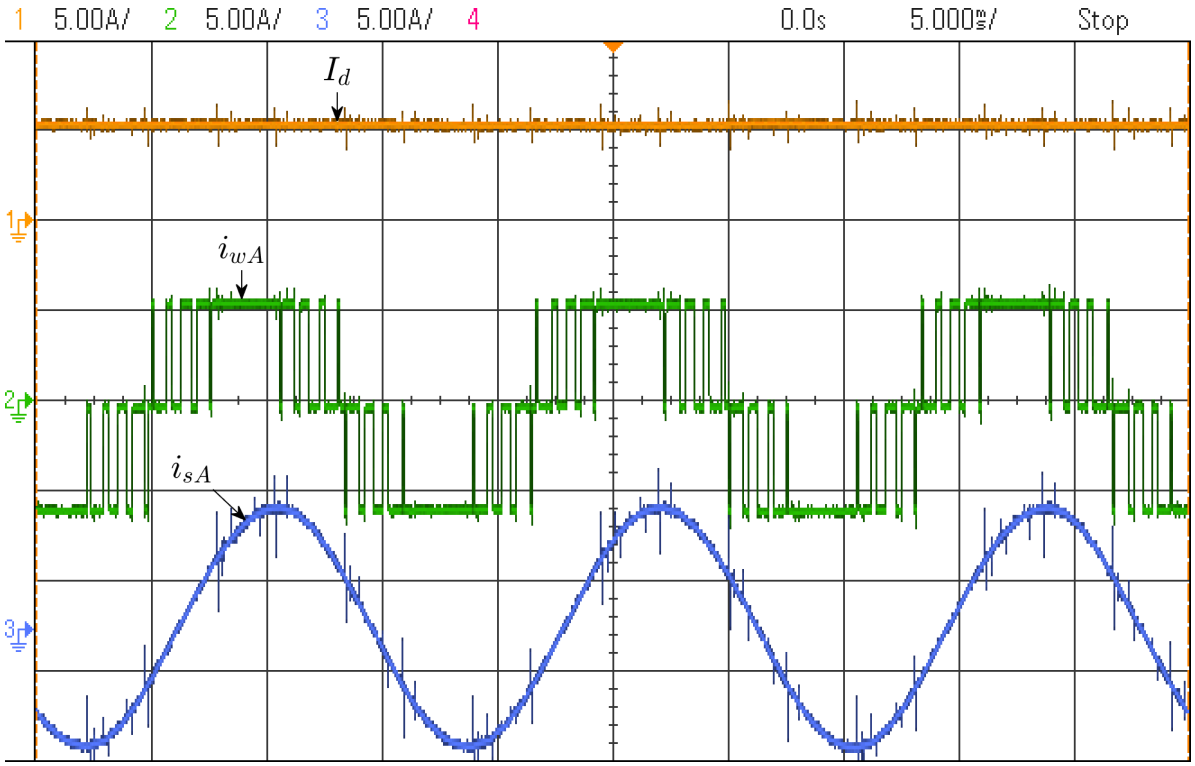

Figure B10: Experimental results showing the DC-link current (I_d), phase-A PWM current (i_{wA}), and phase-A filtered output current (i_{sA}) waveforms during steady-state operation of the proposed SHE-TPWM scheme ($m_a = 1$, $N_p = 9$).